Investigation of Anti-corrosive Coatings Degradation Mechanism

The Use of Non-destructive Evaluation Techniques

Li, Shu

Publication date:
2023

Document Version
Publisher's PDF, also known as Version of record

DTU Chemical Engineering
Department of Chemical Engineering

Investigation of Anti-corrosive Coatings Degradation Mechanism -The Use of Non-destructive Evaluation Techniques

PhD Thesis

PhD Thesis
May, 2023

By
Shu Li

Cover photo: Torben Rasmussen, 2021
Published by: DTU, Department of Chemical Engineering, Søltofts plads, Building 229, 2800 Kgs. Lyngby Denmark
www.kt.dtu.dk
ISSN: [0000-0000] (electronic version)
ISBN: [000-00-0000-000-0] (electronic version)

ISSN: [0000-0000] (printed version)
ISBN: [000-00-0000-000-0] (printed version)

Investigation of Anti-corrosive Coatings Degradation Mechanism-The Use of Non-destructive Evaluation Techniques

Shu Li

PhD Thesis

May 31, 2023

Supervisor:	Kim Dam-Johansen	(DTU Chemical Engineering)
Co-supervisors:	Claus Erik Weinell	(DTU Chemical Engineering)
	Huichao Bi	(DTU Chemical Engineering)

DTU Chemical Engineering
Department of Chemical and Biochemical Engineering

HEMPEL FOUNDATION

Preface

This dissertation is the result of three years of research, from 2019 to 2023, conducted in the Hempel Foundation Coatings Science and Technology Centre (CoaST), at the Department of Chemical & Biochemical Engineering, Technical University of Denmark (DTU), in collaboration with the Institute of Process Engineering (IPE), Chinese Academy of Sciences (CAS). The research is performed within the framework of the Sino-Danish Centre (SDC) for Education and Research. The Ph.D. project was supervised by Kim Dam-Johansen (Professor at DTU CoaST), Claus Erik Weinell (Senior Executive Officer at DTU CoaST), Huichao Bi (Assistant professor at DTU CoaST) and Yangqiang Zhang (External supervisor from IPE).

Shu Li

.....

Signature

.....

Date

Acknowledgements

I would like to extend my sincerest gratitude and appreciation to my supervisors for their support and guidance, and for giving me the opportunity to obtain a Ph.D. without their incredible work for DTU CoaST, none of this would have been possible.

I am grateful to Kim Dam-Johansen, Claus Erik Weinell, and Huichao Bi for their discussions and continued support in helping and guiding me throughout my PhD project.

I would also like to thank the CoaST technicians and the KT workshop for their assistance in preparing the test panels. Additionally, I want to express my gratitude to everyone in CoaST for their contributions in making my time as a Ph.D. student enjoyable and memorable.

Above all, I want to thank my husband, parents, brothers and the rest of my family for their endless love, support, and understanding. They have always been there for me, providing a shoulder to lean on in both good and bad times, and for that, I am truly grateful.

Summary

This project aimed to investigate the degradation processes of commercial coatings using non-destructive evaluation techniques (NDTs). Various NDTs, including Electrochemical Impedance Spectroscopy (EIS), Scanning Acoustic Microscopy (SAM), gravimetric analysis, and Attenuated Total Reflectance Fourier-transform Infrared Spectroscopy (ATR-FTIR), were employed in combination or individually to assess the performance and degradation of zinc-rich primer, epoxy primer, ZnEP/PUR, and EP/PUR coating systems exposed to environments such as neutral salt spray, cyclic ageing test and field test.

EIS offers valuable insights into the degradation process of commercial coatings. For zinc-rich epoxy primers, the evolution of open circuit potential (OCP) indicates sacrificial protection duration, while the impedance modulus (|Z|) reflects the overall barrier properties of the coating. However, the primary protective mechanism of zinc-rich primers is sacrificial protection, and the impedance modulus threshold alone is insufficient for evaluating their corrosion protection effectiveness. In contrast, epoxy barrier coatings rely primarily on their barrier properties to prevent the penetration of aggressive substances to the coating/substrate interface. The impedance modulus is an appropriate parameter to assess coating performance and corrosion is expected to occur when |Z| falls below 10^6 $\Omega \cdot cm^2$ with continued exposure.

The water uptake of epoxy coating immersed in a 3.5 wt% NaCl solution was investigated using gravimetric analysis, EIS, SAM, and ATR-FTIR. Results showed that water uptake in epoxy free film involved rapid absorption, continuous uptake, and leaching of coating ingredients. Coated steel substrates exhibited rapid absorption and slower continuous uptake, attributed to swelling of the applied coating layer. SAM proved to be a feasible technique for non-destructive detection of swelling during water uptake. However, none of the techniques alone can provide accurate water uptake estimation due to their inherent limitations. Together, they offer a comprehensive understanding of epoxy barrier coating deterioration during water uptake.

Scanning acoustic microscopy has proven valuable for studying degradation mechanisms in EP/PUR and ZnEP/PUR coating systems exposed to the field and cyclic ageing test. It revealed distinct rust creep propagation mechanisms that traditional destructive evaluation methods may overlook. During field exposure, both systems exhibited rust creep through a filiform-like corrosion mechanism, indicating similar degradation processes. However, differences in rust creep growth rate were observed due to specific protective mechanisms provided by each coating system.

The cyclic ageing test significantly accelerated rust creep, with the ZnEP/PUR system experiencing a higher acceleration factor of approximately 12 compared to field exposure, while the EP/PUR system had an acceleration factor of around 2. The EP/PUR system showed asymmetric rust creep growth from the scribe, while the ZnEP/PUR system exhibited more uniform growth in cyclic ageing test. Importantly, neither coating system displayed the filiform corrosion mechanism as observed in the field. This highlights the limitations of using the cyclic ageing test alone to rank the performance of different anti-corrosive coating systems, as it may significantly differ from their real-field performance.

In conclusion, this project demonstrated the value of NDTs in assessing coating performance and degradation. The findings highlight the importance of sacrificial protection, barrier properties, water uptake, and rust creep propagation in different coating systems. These insights can contribute to better coating evaluation in the future, leading to improved coating formulations, reduced material consumption, and environmental protection through enhanced durability and performance of corrosion protection systems.

Dansk resumé

Dette projekt havde til formål at undersøge nedbrydningsprocesserne af kommercielle coatinger ved hjælp af ikke-destruktive evalueringsmetoder (NDT). Forskellige NDT-metoder, herunder elektrokemisk impedansspektroskopi (EIS), scanning akustisk mikroskopi (SAM), gravimetrisk analyse og Attenuated Total Reflectance Fourier-transform Infrared Spectroscopy (ATR-FTIR), blev anvendt til at evaluere ydeevne og nedbrydning af zinkrige epoxyprimer, epoxyprimer, ZnEP/PUR og EP/PUR coating systemer, der blev udsat for miljøer som neutral saltspray, cyklisk ældningstest og felteksponering.

EIS gav værdifuld indsigt i nedbrydningsprocessen for kommercielle coatinger. For zinkrige epoxyprimere indikerede udviklingen i det åbne kredsløbspotential (OCP) levetiden for den offerbaserede beskyttelse, mens impedansmodulet (|Z|) afspejlede coatings barriereegenskaber. Det er dog vigtigt at bemærke, at den primære beskyttelsesmekanisme for zinkrige primere er galvanisk beskyttelse, og at impedansmodulet alene ikke er tilstrækkelig til at vurdere deres korrosionsbeskyttelseseffektivitet. I modsætning hertil er epoxybarrierecoatinger primært afhængige af deres barriereegenskaber for at forhindre indtrængning af aggressive stoffer til coating/substrat-grænsefladen. Impedansmodulet er en passende parameter til at vurdere belægningens ydeevne, og korrosion forventes at forekomme, når |Z| falder under $10^6\ \Omega \cdot cm^2$ ved fortsat eksponering.

Vandoptagelsen af epoxycoatinger nedsænket i en 3,5 wt% NaCl opløsning blev undersøgt ved hjælp af gravimetrisk analyse, EIS, SAM og ATR-FTIR. Resultaterne viste, at vandoptagelsen i epoxyfri film involverede hurtig absorption, kontinuerlig optagelse og udvaskning af coatingsbestanddele. Belagte stålsubstrater viste hurtig absorption og langsommere kontinuerlig optagelse, hvilket skyldtes hævelse af det påførte coatingslag. SAM viste sig at være en anvendelig teknik til ikke-destruktiv påvisning af hævelse under vandoptagelse. Ingen af teknikkerne alene kan dog give en nøjagtig vurdering af vandoptagelsen på grund af deres iboende begrænsninger. Samlet set giver de en omfattende forståelse af nedbrydningen af epoxybarrierebelægninger under vandoptagelse.

Akustisk scanningmikroskopi har vist sig at være værdifuld til undersøgelse af nedbrydningsmekanismer i EP/PUR og ZnEP/PUR coating systemer under felt- og cyklisk ældningstest. Den afslørede tydelige mekanismer for rustkrybning, som traditionelle destruktive evalueringsmetoder kan overse. Begge coating systemer viste rustkrybning gennem en filiform korrosionsmekanisme under felteksponering, hvilket indikerer lignende nedbrydningsprocesser. Der var dog forskelle i hastigheden hvormed rusten udbredte sig fra ridsen på grund af de specifikke beskyttelsesmekanismer i hvert coating system.

Den cykliske ældningstest accelererede rustkrybning markant for ZnEP/PUR coating system, med en accelerationsfaktor på ca. 12 for ZnEP/PUR systemet sammenlignet med en accelerationsfaktor på ca. 2 for EP/PUR systemet med felteksponering. EP/PUR systemet viste asymmetrisk rustkrybningsvækst fra ridset, mens ZnEP/PUR systemet viste mere ensartet vækst. Det er vigtigt at bemærke, at ingen af coating systemerne viste den filiform korrosionsmekanisme, der blev observeret i feltet. Dette understreger begrænsningerne at bruge den cykliske ældningstest alene til at vurdere ydeevnen af forskellige korrosionsbeskyttende coating systemer, da den kan afvige betydeligt fra ydeevnen i feltet.

Dette projekt demonstrerede værdien af NDT-metoder til vurdering af coatingers ydeevne og nedbrydning. Resultaterne fremhæver betydningen af galvanisk beskyttelse, barriereegenskaber, vandoptagelse og rustkrybning i forskellige coating systemer. Disse indsigter kan bidrage til bedre evaluering af coatinger i fremtiden, hvilket kan føre til forbedrede coating formuleringer, mindre materialeforbrug og miljøbeskyttelse gennem øget holdbarhed og ydeevne af korrosionsbeskyttende coating systemer.

Contents

List of Figures

List of Tables

Nomenclature

Abbreviations

AC	Alternating current
ASTM	American Society of Testing and Materials
ATR-FTIR	Attenuated total reflectance fourier-transform infrared spectroscopy
CPE	Constant phase element
EDS	Energy dispersive X-ray spectroscopy
ECM	Equivalent circuit model
EIS	Electrochemical impedance spectroscopy
EP or EP-01	Commercial two components epoxy coating
EP50	Commercial two components epoxy coating with a nominal DFT of 50 µm
EP80	Commercial two components epoxy coating with a nominal DFT of 80 µm
EP/PUR	Two-layer coating systems with epoxy barrier primer and polyurethane topcoat
CPVC	Critical pigment volume concentration
GDP	Gross domestic product
ISO	International Standards Organisation
NDE	Non-destructive evaluation
NDFT	Nominal dry film thickness
OCP	Open circuit potential
PVC	Pigment volume concentration
SAM	Scanning acoustic microscopy
SCE	Saturated calomel electrode
SEM	Scanning electron microscopy
SHE	Standard hydrogen electrode
UVBs	UV light absorber
VOC	Volatile organic compounds
ZnEP	Commercial two components zinc-rich epoxy primer
ZnEP50	Commercial two components zinc-rich epoxy primer with a nominal DFT of 50 µm
ZnEP80	Commercial two components zinc-rich epoxy primer with a nominal DFT of 80 µm
ZnEP/PUR	Two-layer coating systems with zinc-rich epoxy primer and polyurethane topcoat

Physical and mathematical constants

a_{red}	Chemical activity of the reduced species
a_{Ox}	Chemical activity of the oxidised species
A	Area
C	Capacitance
C_{HF}	Coating capacitance determined at a fixed high frequency (HF)
C_{dl}	Double layer capacitance
E	Potential
$E(t)$	Potential as function of time
E_{Cell}	The equilibrium cell potential
E°_{Cell}	The standard cell potential
E°_{Ox}	The standard potential of the anode
E°_{Red}	The standard potential of the cathode
ΔG	Gibbs free energy
ΔG°	The standard Gibbs free energy
F	Faraday constant
f	Frequency
$I(t)$	Current as function of time
I_R	The amount of ultrasound intensity reflection
L	Inductor
l	Length
n	Number of electrons
R	Resistance
R_{ct}	Charge transfer resistance
R_{gas}	The gas constant
R_s	Electrolyte resistance
R_{SAM}	Ultrasound reflection coefficient
T	Temperature
T_{SAM}	Ultra sound transmission coefficient
t	Time or time of flight
v	Velocity
V_p	Volume of pigments and extenders/fillers
V_b	Volume of binder systems
Z	Electrochemical impedance
Z''	Imaginary part of the impedance
Z'	Real part of the impedance
$\|Z\|$	Electrochemical impedance modulus
Z_{SAM}	Acoustic impedance

Greek letters

ε_0	Electrical permittivity constant
ε	Dielectric constant
ρ	density
ω	Angular frequency
ω_{max}	Maximal angular frequency

1 Introduction

Anti-corrosive coatings provide essential technologies to protect all metallic constructions from corrosion in our modern society's infrastructure and the technologies can extend the utilisation lifetime of 20 % to the painted materials [1]. The direct cost of preventing and managing corrosion failures is currently estimated to be 3-4 % [2] gross domestic product (GDP) of a developed country. Besides, the economic expanses, corrosion failures can further lead to severe tragedies in safety and environmental aspects e.g. leakages, bridge collapses and other hazards. Furthermore, the global steel production is estimated to generate around 43.8 Gt CO_2 and between 560-1200 Mt CO_2 of these emissions can be associated with the replacement of corroded steel [3]. To contribute to the global fight against climate change e.g. the Paris Agreement in 2015 [4], where EU's nations have targeted to reduce greenhouse gases emission by at least 55 % compared to 1990 levels by 2030. Therefore, an optimisation of anti-corrosive coating technologies may contribute to the reduction of CO_2 through the extension of the steel construction's lifespan and thereby reduce the steel consumption applied for the replacement of corroded steel constructions.

Nowadays, the anti-corrosive technologies applied under harsh marine and offshore environments are dominated by epoxy based coatings due to their high crosslink density and relatively high resistivity for aggressive chemical species [5, 6, 7]. The commercial anti-corrosive coatings in the market provide at least 20 years [8] of protection which challenges the evaluation methods for new coating formulations' performance compared to the existing products. The long protective lifetime of commercial anti-corrosive coatings also makes the field data collection a time, resource and manpower demanding process.

Thus, the development of accelerated laboratory testings has been necessary where coating samples are exposed under controlled and severe environmental conditions to accelerate the coating degradation process. The widely accepted standardised testing protocols are specified by International Standards Organisation (ISO) and American Society of Testing and Materials (ASTM), and these protocols, known as accelerated testing, aim to minimise the experimental time and still capture the same degradation mechanisms as in natural exposure. The signs of coating degradation can be evaluated through numerous factors, e.g. degree of blistering, rusting, cracking, delamination and loss of adhesion or gloss [9]. The standardised approach for coating assessment exposed to harsh marine and offshore environments is through the evaluation of rust creep evolution around an artificial scribe on the test panel specified in ISO 12944. One drawback of the rust creep evaluation methods specified in ISO 12944 is the destructive approach for the rust creep evaluation, where the detached coating area around the scribe is removed before determination of the the rust creep underneath the coating. The destructive evaluation technique limits the further investigation of the panel, which is unable to study the degradation propagation. Therefore, non-destructive evaluation techniques would contribute to a faster and more accurate assessment of coating performance by providing a lot more information without causing damage, and enabling a better understanding of the degradation mechanism involved. Increasing knowledge of the degradation mechanism of coatings would enhance the efficiency of evaluating coating performance, and provide a strong tool for coating development, thereby reducing the production and consumption of materials.

1.1 Objectives of the Ph.D. project

This Ph.D. project aims at improving the current evaluation methodologies of anti-corrosive coatings, to facilitate the development of new environmentally friendly coatings for protection against corrosion. To attain this, the following objectives were addressed during the project:

- Investigation of applicability for existing non-destructive techniques for evaluation of anti-corrosive coatings performance
- Investigate water uptake process through anti-corrosive coating by applying non-destructive evaluation methods
- Investigate anti-corrosive coatings degradation in the field and in the accelerated laboratory test non-destructively

1.2 Outline of the thesis

Including the introduction, this thesis is divided into seven chapters.

Chapter 2: Literature survey

Chapter 3: Electrochemical impedance evaluation of coating performance

Chapter 4: Non-destructive evaluations of water uptake in epoxy coating

Chapter 5: A quantitative real-time evaluation of rust creep propagation in coating systems exposed to field testing and cyclic ageing test

Chapter 6: Conclusion

Chapter 7: Future work

2 Literature Review

2.1 Corrosion

Corrosion is a natural, thermodynamic favourable process that leads to the degradation of materials, particularly metals, due to chemical and electrochemical reactions with the surrounding environment. The process typically involves the oxidation of metal ions to metal oxides, which alters the property of the material and can result in a decrease in its performance, durability and lifespan.

The corrosion of steel structures is primarily caused by iron corrosion which can be a complex phenomenon governed by several factors, including the composition of the environment, the metal surface property, and the presence of corrosion inhibitors. To fully understand the corrosion process, thermodynamics can provide a useful framework for analysing the underlying mechanisms.

2.1.1 Thermodynamics of corrosion

The driving force for the corrosion of iron at standard conditions is determined by the potential difference between the electrochemical half cell reactions. The standard cell potential, denoted as E°_{Cell}, is calculated by adding the standard potential of the anode E°_{Ox} and the standard potential of the cathode E°_{Red} :

$$E^{\circ}_{Cell} = E^{\circ}_{Ox} + E^{\circ}_{Red} \tag{2.1.1}$$

The equilibrium cell potential of a reaction is given by Nernst Equation:

$$E_{Cell} = E^{\circ}_{cell} + \frac{R_{gas}T}{nF} \ln\left(\frac{a_{red}}{a_{Ox}}\right) \tag{2.1.2}$$

where R_{gas} is the gas constant, T is the temperature, n is the number of electrons involved in the reaction and F is Faraday constant. a_{red} and a_{Ox} are the chemical activity of the reduced and oxidised species, respectively.

The cell potential can be used to determine whether a corrosion reaction is thermodynamically favourable or spontaneous. The relationship between Gibbs free energy and the equilibrium cell potential is given by:

$$\Delta G^{\circ} = -nFE^{\circ}_{cell} \tag{2.1.3}$$

where n is number of electrons involved and F is Faraday constant.

As an example, the change of Gibbs free energy and standard equilibrium potential can be determined by considering the formation of ferrous hydroxides:

$$2\mathrm{Fe(s)} + \mathrm{O_2(aq)} + 2\mathrm{H_2O} \rightarrow 2\mathrm{Fe(OH)_2(aq)} \tag{2.1.4}$$

The standard electrochemical equilibrium potential is given by the half-cell standard potential for oxidation of iron ($E^{\circ}_{\mathrm{Fe}\rightarrow\mathrm{Fe^{2+}+2e^-}} = 0.447$ V/SHE) and the half-cell standard potential reduction of oxygen ($E^{\circ}_{\mathrm{O_2+H_2O+4e^-}\rightarrow\mathrm{4OH^-},\ \mathrm{pH=7}} = 0.82$ V/SHE).

$$E^{\circ}_{Cell} = E^{\circ}_{Ox} + E^{\circ}_{Red} = 0.447\ \mathrm{V} + 0.82\ \mathrm{V} = 1.267\ \mathrm{V}$$

Since the standard equilibrium potential is positive, the $\Delta G < 0$ calculated using Equation (2.1.3) will be negative indicating that the reaction is a spontaneous thermodynamic favourable process:

$$\Delta G = -2 \cdot 96485 \, \frac{\text{coulomb}}{\text{mole}} \cdot 1.267 \, \text{V} = -244.5 \, \frac{\text{kJ}}{\text{mole}}$$

2.1.1.1 Pourbaix diagram

The thermodynamic stability regions of different chemical species of iron as a function of pH and potential (E) are typically illustrated through a Pourbaix diagram. Figure 2.1.1 depicts the stability of different forms of iron compounds in a chloride aqueous system at 25 °C. The stable phases in a Pourbaix diagram are separated by solid lines, whereas the dashed lines A and B in Figure 2.1.1 enclose the stable region of water molecules undergoing oxidation and reduction. Water is oxidised to oxygen above the A-line, while water molecules are decomposed to hydrogen below the B-line.

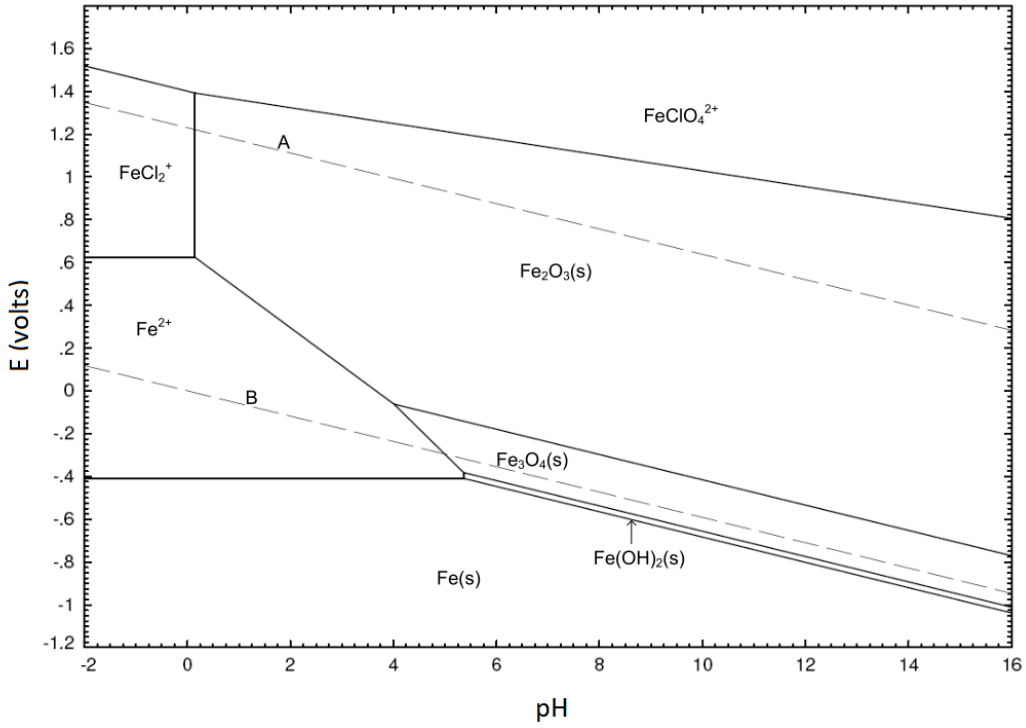

Figure 2.1.1: Pourbaix diagram for Fe-$H_2O - Cl^-$ system [10] at 25 °C. X-axis is the pH and y-axis is the equilibrium potential (V/SHE).

Figure 2.1.1 shows that solid iron is thermodynamically stable at a potential lower than -0.4 V/SHE at pH ranging between -2 to around 5, indicating the iron is stable against corrosion from a thermodynamic point of view. However, thermodynamics cannot provide information about the kinetics of electrochemical reactions, i.e., the corrosion rate. A metal may be thermodynamically unstable for a given set of conditions, but it degrades slowly due to reaction kinetics. Hence, unstable species from the previous stage may still be present due to the slow decomposition. These are not shown on the Pourbaix diagram

due to simplification and focus of interest. In practice, the assumption of equilibrium between metal and its ions, etc., may not be reached when corrosion reactions are kinetics-dependent. The pH-value in the diagram is a surface value, whereas in practice, pH can vary locally. Thus, the information from the Pourbaix diagram must be used with caution. However, the Pourbaix diagram provides a visual representation of the stability regions of chemical species in an aqueous solution, enabling the analysis of corrosion behaviour and prediction of predominated corrosion products.

2.1.2 Mechanism of corrosion

The major structural failures in the marine and offshore environments are due to the degradation of steel structures caused by corrosion. Corrosion in steel can be accelerated by physical damage in the protected surface, which causes a high excess of aggressive species such as water, oxygen and ions. Figure 2.1.2 illustrates the simplified corrosion process on a steel surface through electrochemical reactions.

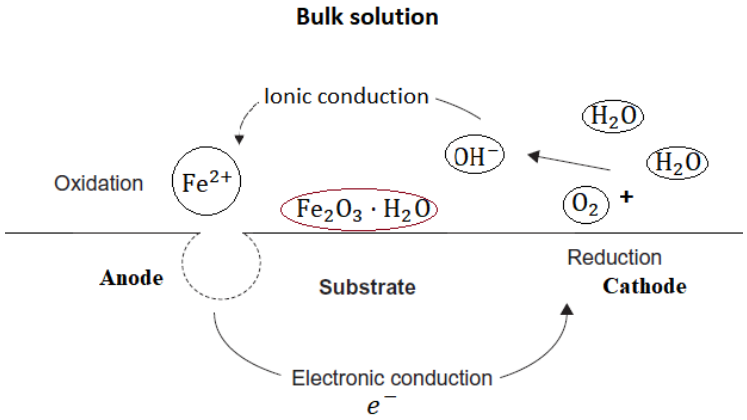

Figure 2.1.2: A simplified illustration of corrosion process of iron in a steel substrate in the presence of water, oxygen and electrolyte, at pH=7.

From the electrochemical perspective, corrosion occurs when there is a potential difference generated between an anode and a cathode sites in contact with an electrolyte. The Nernst equation (Equation (2.1.2)) indicates that the equilibrium cell potential is dependent on the activity/concentration of redox species. Thus, at a point on the steel surface where the concentration of oxygen is higher (cathode) compared to another point with a lower oxygen concentration (anode), a potential difference is generated on the steel surface. This potential difference causes iron to oxidise at the anode and oxygen to reduce at the cathode, as shown in Figure 2.1.2. These two half-cell reactions are balancing each other in the production and consumption of electrons, given as:

$$\text{Anode}: \quad 2\text{Fe(s)} \rightarrow 2\text{Fe}^{2+} + 4\text{e}^- \tag{2.1.5}$$

$$\text{Cathode}: \quad \text{O}_2\text{(aq)} + 2\text{H}_2\text{O(l)} + 4\text{e}^- \rightarrow 4\text{OH}^- \tag{2.1.6}$$

The iron(II) ions and hydroxide ions would be in equilibrium with the sparingly soluble iron(II)oxide (Fe(OH)_2). The iron(II) oxide can further be oxidised to form an unstable green hydrated magnetite, $\text{FeO} \cdot \text{Fe}_2\text{O}_3 \cdot \text{H}_2\text{O(s)}$:

$$6\text{Fe(OH)}_2\text{(aq)} + \text{O}_2 \rightarrow 4\text{H}_2\text{O} + 2\text{FeO} \cdot \text{Fe}_2\text{O}_3 \cdot \text{H}_2\text{O(s)} \tag{2.1.7}$$

The green hydrated magnetite will further decompose to black magnetite, $FeO \cdot Fe_2O_3(s)$:

$$FeO \cdot Fe_2O_3 \cdot H_2O(s) \rightarrow FeO \cdot Fe_2O_3(s) + H_2O(l) \tag{2.1.8}$$

The black magnetite will further be oxidised to stable red brown hydrated hematite commonly referred as rust, $Fe_2O_3 \cdot H_2O(s)$:

$$2FeO \cdot Fe_2O_3(s)(s) + \frac{1}{2}O_2(aq) + 3H_2O(l) \rightarrow 3Fe_2O_3 \cdot H_2O(s) \tag{2.1.9}$$

The overall reaction of corrosion of iron to rust is then [10]:

$$6Fe(s) + 4\frac{1}{2}O_2(aq) + 3H_2O(l) \rightarrow 3Fe_2O_3 \cdot H_2O(s) \tag{2.1.10}$$

In summary, the corrosion of iron is a thermodynamically favourable process that proceeds through the formation of intermediate products, such as green hydrated magnetite and black magnetite, before the stable corrosion product, rust, is formed under an excess supply of water and oxygen.

2.1.3 Classification of corrosion

The most common types of corrosion are uniform-, pitting-, filiform-, and galvanic corrosion. Each of these types has its own unique characteristics and can cause different forms of damage to the metal surface. In this section, each type of corrosion would be explored and discussed their causes and effects.

2.1.3.1 Uniform corrosion

Uniform corrosion occurs in a large fraction of the metal surface area due to exposure to the environment with a relatively constant corrosion rate. The spontaneous corrosion of materials in atmospheric proceed typically uniform corrosion, which the rate is affected by factors such as temperature, relative humidity, time of wetness, pH of the electrolyte, and the presence of contaminants such as Cl^-, NH_3, SO_2 and NO_2 in polluted industrial areas.

2.1.3.2 Pitting corrosion

Pitting represents an extremely localised corrosion attack that produces crevices in the metal or alloys and is classified as one of the most destructive localised corrosion. This is because localised pit attacks can cause accelerated structural component failure by either perforating them or initiating cracking [11]. Pitting corrosion initiation can be divided into four stages as shown in Figure 2.1.3.

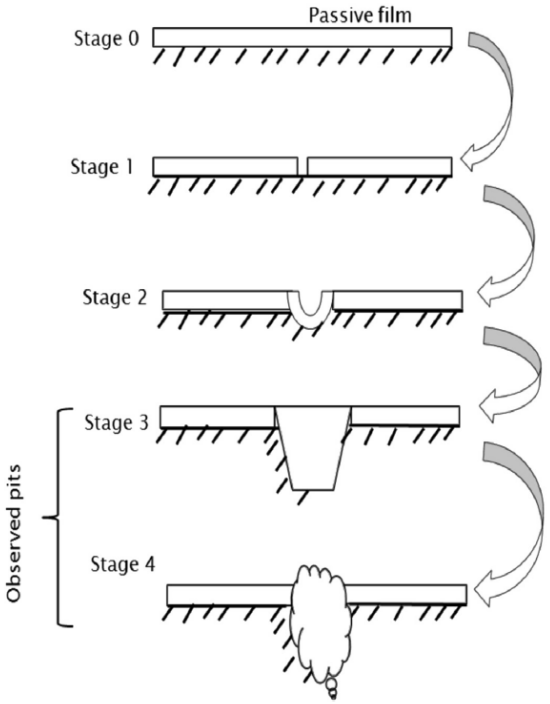

Figure 2.1.3: Schematic illustration of pit development adapted from [11].

Stage 0 represents an ideal perfect passive film, which could be an oxide layer or an organic coating covered over a metallic surface. Stage 1 involves micro-defects of the passive layer, where most of the substrate is still well-protected, except for the local defect, which is in contact with the corrosive species from the environment. Stage 2 is reached when pit growth conditions are established, and repassivation is not possible. Stage 3, the pit

begins to grow on the substrate and becomes around $1-10\ \mu m$, which can be detected under a microscope. At the final stage 4, the pits can be seen with the naked eye.

2.1.3.3 Galvanic corrosion

When a potential difference is established between two metals (or alloys) that are electrically connected in a conducting medium, electrons will flow and cause corrosion of the metal with more negative potential. The more positive the corrosion potential of a metal, the less reactive it is, whereas a more negative corrosion potential indicates a higher likelihood of the metal acting as an anode and undergoing corrosion. Galvanic corrosion occurs when the driving force of the corrosion is due to the potential difference between two metals. Figure 2.1.4 shows the galvanic series measured in seawater for common metals and alloys.

A common example of galvanic corrosion is the use of a zinc-rich primer on a steel substrate in anti-corrosive technologies. Zinc is not resistant to corrosion, and the primer cannot be classified as a barrier coating either. However, the zinc-rich primer protects the steel substrate because zinc has a more negative potential (less noble) and acts as the anode, thereby protecting the iron in steel.

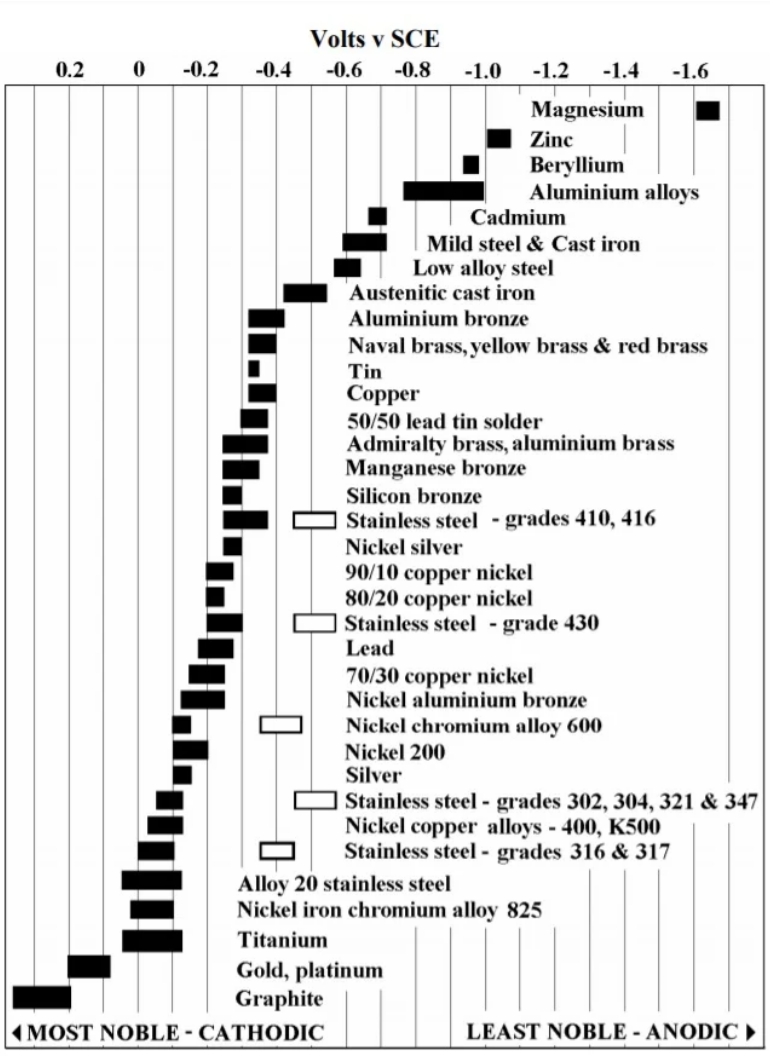

Figure 2.1.4: Galvanic series of metals and alloys in seawater [12].

2.1.3.4 Filiform corrosion

Filiform corrosion is observed under thin organic coatings, typically between 80-100 μm on aluminium and steel exposed to humid atmosphere [13, 14]. Filiform corrosion occurs when there is a local breakdown in organic coatings, enabling the local dissolution of the metallic substrate, leading to a gradual loss of adhesion between the coating and the steel substrate. As adhesion is lost, a small crevice can develop between the coating and the substrate, allowing aggressive species such as water, oxygen and ions to pass through. Figure 2.1.5a shows filiform corrosion underneath a transparent acrylic-coated steel, with filaments growing from the scribe defect. The mechanism of the filaments' growth in filiform corrosion is illustrated by Figure 2.1.5b. The head of the filament consists of the anode and acts as an active corrosion cell, where iron atoms are oxidised to form Fe^{2+} with an excess of electrons transported to the near-cathodic site, where oxygen and water react and form hydroxides via reduction. The formed hydroxides are believed to weaken the interface adhesion and increase the local pH, leading to cathodic delamination [15].

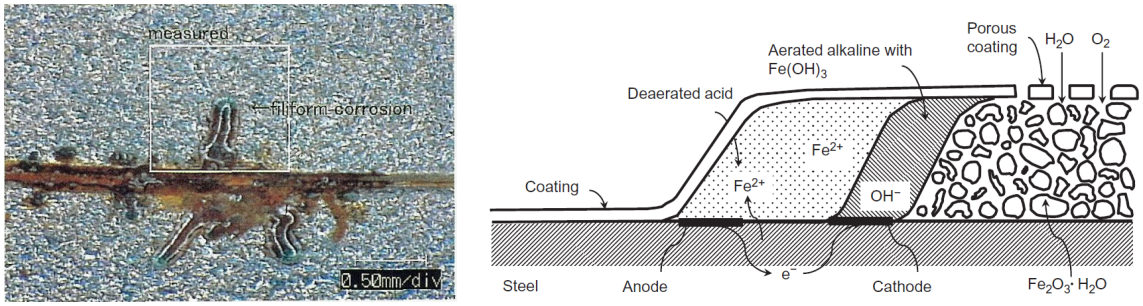

(a) From top (b) From side

Figure 2.1.5: (a) Filiform corrosion observed on transparent acrylic coated steel [16] and (b) an illustration of filiform corrosion mechanism on coated steel [14].

The filament tail is filled with inert rust, $Fe_2O_3 \cdot H_2O$, as shown in Figure 2.1.5b. Water and oxygen diffuse through the corrosion products under the coating into the delaminated area. A differential aeration cell is established between the deaerated filament head and aerated filament tail due to the thousand times slower oxygen transport rate through the coating layer compared to the transport rate via the corrosion products [13].

2.1.4 Classification of the corrosion environments- ISO 12944

ISO 12944-2 categorizes corrosive environments into three types of exposures: atmospheric, splash zone, and immersion. Steel structures may encounter these environments, and it is essential to determine the appropriate level of corrosion protection (coating system) required for different applications. The classification system also helps establish standard accelerated testing procedures for evaluating the performance of protective coatings in diverse corrosive environments.

2.1.4.1 Atmospheric

In atmospheric exposures, structures must withstand UV radiation, heat, moisture, salt and gases commonly in polluted areas. The degree of corrosion in the atmospheric environments can vary significantly depending on the local climate, such as the level of pollution and the distance to the sea. ISO 12944-2 classifies the atmospheric environments into six different corrosion intensities as presented in Table 2.1.1. The atmospheric exposure can further be divided into rural, industrial and marine environments, categorised as low, high and very high corrosivity. The industrial atmosphere consists of a high amount of solid particles, particularly soot, and sulphate salts. The structures are exposed to the acidic environment because of the high content of sulphur dioxide in the atmosphere, which results in acid rain. The extreme marine environment consists of a high amount of chloride ions, which are aggressive towards metals and is reported as one of the main corrosion propagation agents [17].

Table 2.1.1: Atmospheric-corrosivity categories and examples of typical environments after ISO 12944-2:2017.

Corrosion category	Corrosivity	Examples of typical environments
C1	Very low	**Interior**: Heated buildings e.g. offices, shops, schools, hotels
C2	Low	**Exterior**: Rural areas with low level of pollutions **Interior**: Unheated buildings possible for condensation e.g. depots, sports halls
C3	Medium	**Exterior**: Urban industrial atmospheres moderate SO_2 pollution coastal areas with low salinity **Interior**: Production rooms with high humidity and some air pollution e.g. food-processing plants laundries, breweries, dairies
C4	High	**Exterior**: Industrial- and coastal- areas with moderate salinity **Interior**: Chemical plants, swimming pools, coastal ships
C5	Very high	**Exterior**: Industrial areas with relative high humidity and aggressive atmosphere with high salinity **Interior**: Buildings or areas with almost permanent condensation and high pollution
CX	Extreme	**Exterior**: Offshore areas with high salinity, humidity and aggressive atmosphere, and tropical atmospheres **Interior**: Industrial areas with extreme humidity and aggressive atmosphere

2.1.4.2 Splash zone

The splash zone refers to the environment near the waterline of the sea and can be referred to as the surface structures that is periodically in and out of the water due to waves and tides. Structures such as the foundation of a ship, wind turbines and offshore plants are exposed to the splash zone. The extremely corrosive environment in the splash zone is caused by a combination of an oxygen-rich atmosphere with a continuous splashing of electrolytes (salt ions) from the sea, which enhances the corrosion process.

2.1.4.3 Immersion

Immersed environments are further divided into freshwater, seawater, and burial soil, as summarised in Table 2.1.2. For freshwater immersion, the corrosivity is mainly determined by the concentration of dissolved salt and oxygen. For seawater immersion, the aggressiveness of corrosion depends on factors such as temperature, pH, salinity, and contents of dissolved gases such as oxygen. In burial soil immersion, the aggressiveness is determined by factors such as humidity, bacteria, salt, oxygen, and pH.

Table 2.1.2: Immersion-corrosivity categories for water and soil with examples of typical environments after ISO 12944-2:2017.

Corrosion category	Environment	Examples of structures
Im1	Fresh water	River installation, hydro-electric power plants
Im2	Sea/ brackish water	Immersion structure without cathodic protection (e.g. harbour areas with structures like sluice gates, locks or jetties)
Im3	Soil	Buried tanks, steel piles, steel pipes
Im4	Sea/brackish water	Immersed structures with cathodic protection (e.g. offshore structures)

2.1.4.4 The aggressive offshore environment

Figure 2.1.6 illustrates an offshore structure immersion, which can further be divided into five zones: the atmospheric zone, splash zone, tidal zone, submerged zone, and subsoil zone. The atmospheric zone is located above sea level, and the degree of corrosion is dependent on the humidity and the atmospheric salt content. The splash zone is defined as the area that is occasionally wet due to tides and the wind. The corrosion rate of metal in the splash zone has been reported to be the highest [18], as there is a continuous supply of dissolved oxygen. In the tidal zone, the structure is alternately submerged and exposed to the splash zone as the tide varies. The corrosion rate in the tidal zone is affected by tidal flow, where higher flow movement increases the corrosion rate. The submerged zone is defined as the area of the structure that is always immersed in the seawater. The corrosion rate in the submerged zone is dependent on the oxygen transport to the cathodic sites, and as the distance to the sea surface increases, the dissolved oxygen concentration decreases. In the subsoil zone where the structure is burned, the oxygen concentration is relatively low, and hydrogen sulfide may be present.

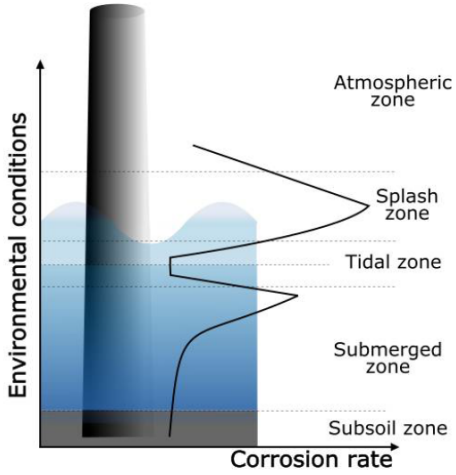

Figure 2.1.6: Corrosion zones of offshore structures with variation in corrosion rate at each zone adapted in [19].

Corrosion of steel

Imafuku et al. [18] evaluated the corrosion rate of a pure steel plate placed in real field offshore testing for 20 years and the results are presented in Figures 2.1.7 and 2.1.8. Figure 2.1.7 shows that the steel plate thickness loss is measured to be 1.5-2 mm during the exposure time of 2.5-19.5 years of exposure in the submerged zone due to a low supply of oxygen. The upper area of the tidal zone showed the lowest steel loss and corrosion rate (Figure 2.1.8), suggesting a large macro cell of steel is formed in steel structure, where the upper area of the tidal zone is cathodic protected by the splash zone steel. In the splash zone, the accumulated loss of steel plate is highest, where 1.9-7.1 mm loss of plate thickness was measured during 2.5-19.5 years of exposure. Additionally, the corrosion rate measured at the splash zone was also the highest measured from 0.68 mm/year (measured after 2.5 years) and stabilised at 0.35 mm/year from 14.5 years of exposure, as shown in Figure 2.1.8. The measured splash zone corrosion rate is consistent with the steel corrosion rate of >0.2 to 0.7 mm/year defined under CX extreme corrosivity in ISO 12944-2. The results presented in Figures 2.1.7 and 2.1.8 support the notion that the corrosion rate is highest near the splash zone and that it reaches a constant level as the exposure time increases to infinity.

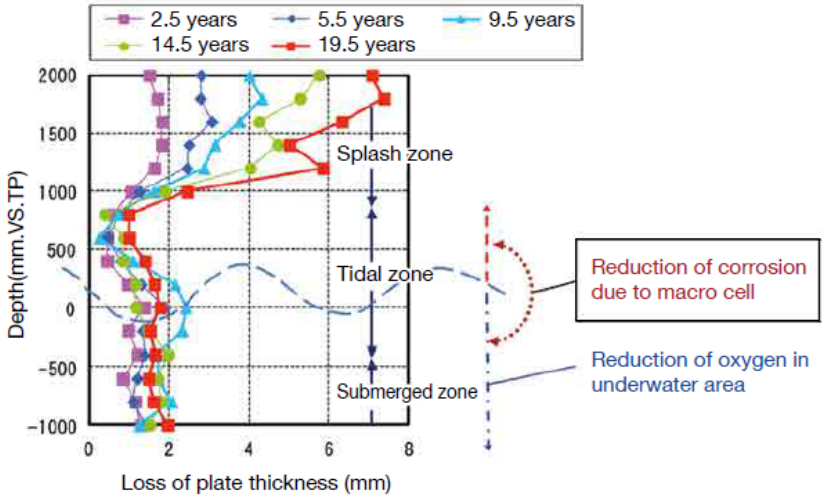

Figure 2.1.7: The loss of pure steel plate at splash zone, Tidal zone and submerged zone at the marine environment. Y-axis is the depth (mm) according to sea surface and x-axis is loss of the steel plate in (mm), adapted in [18].

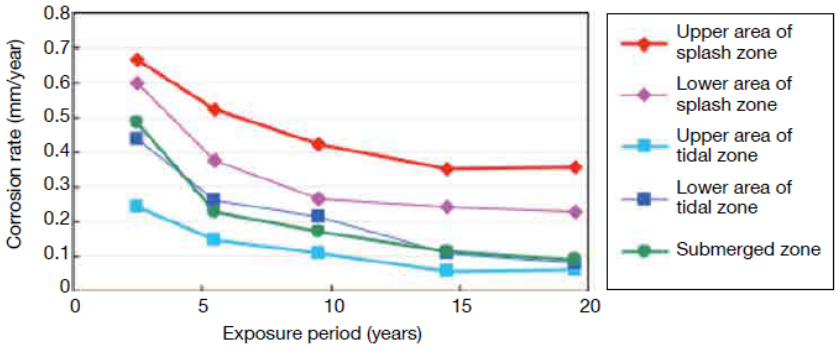

Figure 2.1.8: Corrosion rate of pure steel exposed for marine environment. Y-axis is the corrosion rate (mm/year) of the steel and x-axis is the exposure time (year), adapted in [18].

In conclusion, the ISO 12944-2 defined corrosivity levels are crucial in selecting the optimal corrosion protection and identifying the most corrosive spots for coating degradation within a short time period. The identification of the splash zone as the most corrosive spot provides valuable insights for the field study of this project.

2.2 Coating systems for corrosion protection

Anti-corrosive coatings are designed to provide a protective barrier between the substrate and the environment, offering high resistance to corrosion agents such as water, oxygen, and ions. In addition to these functional requirements, good performance is firstly dependent on strong adhesion to the metal substrate either directly or through a primer. A typical anti-corrosive coating comprises multiple layers, including primer, intermediate and topcoat, each layer with its formulation, properties and purpose. Generally, a coating formulation consists of binders, pigments, solvents, extenders, and additives, each with a unique function during formulation and application.

2.2.1 Coating components

2.2.1.1 Binder

A binder is a polymer resin that forms a continuous film on the substrate surface and is dispersed in a carrier, such as a solvent. The most important properties of a binder are to ensure adhesion to the metal substrate, cohesion within the coating, high mechanical strength and low permeability. Binders can be classified into classes of thermoset and thermoplastic. The thermoset binder based paint dries through chemically crosslinking, while a thermoplastic binder dries physically through solvent evaporation. After curing thermoplastic binder can be re-dissolved in the same solvent, while a thermoset binder is solvent independent. The widely used binders are epoxy-, polyurethane-, and alkyd resins and a detailed description of these resins and their functions can be found in [20].

2.2.1.2 Pigments

Pigments have multiple functions in the coating formulation, including providing colour, corrosion protection, and adding to the barrier effect. Solid powder pigments are commonly used in coatings and are dispersed into the binder with a particle size range of 5-10 μm [7]. Pigments can provide different types of protection, such as (i) barrier protection using chemically resistant pigments for acidic and alkaline environments, (ii) sacrificial pigments based on zinc to provide galvanic protection, and (iii) inhibition protection based on active pigments such as chromates. The widely used pigments in anti-corrosive coatings are metallic zinc, metallic aluminium flake and zinc phosphate.

An important parameter for coating formulation design is determination of the pigment volume concentration (PVC):

$$PVC = \frac{V_p}{V_p + V_b}$$

where V_p is the volume of pigments and extenders/fillers and V_b is the volume of the binder system.

The critical pigment volume concentration (CPVC) is the threshold value that ensures there is enough polymer matrix to wet individual pigment and extender particles. CPVC is determined experimentally by measuring the amount of linseed oil that a particular type of pigment can absorb. If the level of pigmentation exceeds the CPVC (PVC>CPVC), there would not be enough binder to wet and fill the voids between dry particles in the coating formulation. This can result in a coating with voids that may be highly permeable to aggressive species from the external environment, thereby accelerating coating failures.

2.2.1.3 Solvents

Solvents are added to coatings to dissolve or disperse the other constituents of the formulation such as binder and pigments. Additionally, solvents reduce the viscosity of coating to a suitable level for various application methods like brush, roller, conventional spray, and airless spray. After application, solvents evaporate and do not play a role in the dry coating film. Therefore, solvents balance the evaporation rate and dissolution of the binder for organic solvent-borne coating. However, many traditionally used solvents are slowly being banned due to their toxicity, volatility or explosiveness. This has led to extensive research on volatile organic compounds (VOC) compliant coatings such as water-borne, solvent-free and inorganic solvent-borne coatings.

2.2.1.4 Additives

Additives added in coating formulations are characterized by the fact that a small amount can lead to a big change in desired properties. Additives are usually the most expensive ingredients in the formulation. They can include defoamers, which reduce foam formulation during both production and application; thickeners, which improve pigment anti-settling properties; stabilizers, which adsorb UV light or heat; surfactants, which lower the surface tension and curing additives, which speed up the crosslinking reactions.

2.2.1.5 Extenders

Extenders are typically natural minerals, such as limestone and silicates, added to lower production costs. They can be used to adjust the desired pigment volume concentration. Generally, extenders do not improve anti-corrosive properties, although certain extenders have been reported to improve the mechanical properties of the coating [20].

2.2.2 Anti-corrosive protection technologies

The widely used technologies for protecting metal substrate against corrosion include: i) improving barrier properties to reduce the permeability of corrosive species; ii) adding sacrificial metals, such as zinc particles, into the coating formulation to protect the iron in the steel from corrosion; and iii) adding inhibitive pigments, which create a passive barrier at the surface of the metal substrate. In addition, to these protection technologies, a proper application of coatings and surface pretreatment of the substrate before application are prerequisites for the optimal use of these protection methods.

2.2.2.1 Substrate pretreatment

Surface pretreatments of the substrate before coating application are essential procedures prior to any anti-corrosion coating technologies. If the adhesion between the substrate and coating interface is poor, the substrate may experience failure before the activation of anti-corrosive coating technologies. Surface preparation can be mechanical or chemical, such as water jetting, wet abrasive blasting, power tools, and shot or grit blasting. Chemical practices include solvent cleaning, acid pickling, and flame cleaning [9]. Moreover, poor construction design, such as sharp edges, ship welds and crevices, can lead to early coating failure.

The application of coating material on ships is primarily done through spraying, rolling, or brushing. Before the coating application, it is essential to clean the substrate to remove any hydrocarbon, salt residues, water, microorganism deposits, and corrosion products such as oxides and rust that may interfere with the coating's ability to achieve adhesion and wetting. The interference can lead to issues such as blistering, peeling, and delamination. Experimental evaluation of the delamination rate was found to be larger in non-pre-cleaned substrates compared to cleaned substrates [20].

The surface pretreatments for coating applications on new constructions are also extremely important. All coatings require maintenance, and the time interval for maintenance is directly related to the efficiency of the initial application. Poor coating application can cause problems such as improper thickness, pinholes, sags mud cracking. Cracks in the coating would accelerate the corrosion and erosion processes. During coating application, surrounding conditions such as temperature and humidity should be considered. Painting under high humidity conditions can result in moisture condensation on the steel surface.

2.2.2.2 Barrier Protection

The principle of barrier protection is to reduce the permeability of corrosion agents such as water, oxygen and salt ions. This can be achieved by increasing the content of inert polymers and/or pigments in coating formulations. Lamellar pigments are commonly used because they can orient themselves parallel to the substrate surface, providing a longer diffusion pathway for unwanted species. In contrast, the barrier effect is weaker when using spherical pigments as they have a shorter diffusion pathway, as shown in Figure 2.2.1. However, it has been observed that using a mixture of spherical and lamellar pigments can provide the most effective barrier effect in coatings, as reported by Sørensen et al. [21].

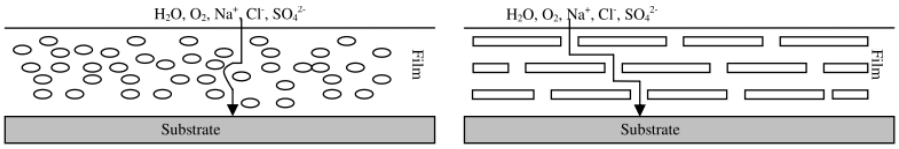

Figure 2.2.1: A simplified illustration of barrier effect using spherical- and lamellar pigments, respectively [10].

The effectiveness of barrier protection further depends on the applied coating thickness and binder properties, such as high crosslink density [10]. Ideally, increasing the coating thickness and crosslink density will increase the degree of impermeability. However, a high crosslink density can also cause the dry coating to become brittle, which can easily lead to the formation of cracks in the film. Therefore, the coating formulation design should generally aim to find a balance between increasing the protection ability, simplifying the application process, and minimizing economic consumption.

2.2.2.3 Sacrificial protection

In the sacrificial/cathodic/galvanic protection system, a less noble metal in the galvanic series (Figure 2.1.4) such as zinc, aluminium, or magnesium, is added to the paint formulation. Sacrificial coatings are usually applied as primers, as it requires direct contact between the substrate and sacrificial metal to establish electrical contact and thereby activate the galvanic corrosion. Zinc is often used as the sacrificial pigment in anti-corrosive coatings. In contact with corrosion agents, zinc particles act as an anode and corrode (sacrifice themselves) instead of the iron in the steel substrate, which becomes the cathode. This process is also called cathodic protection. Another reason for zinc's effectiveness as a sacrificial metal is that the zinc oxide formed is inert and dense, filling the pores in the coating system to the point where the local system becomes non-conductive. While zinc oxides enhances the barrier effect of the coating, it also decreases the sacrificial protection efficiency by reducing the electrical contact as more particles are consumed. To increase the contact between zinc particles during the sacrificial process, the zinc pigment volume must be high. The highest conductivity is reportedly achieved at zinc concentration in the

range of 92−95 % of the dry film [10]. However, according to the ISO 12944 zinc particle content ≥85 wt% is classified as a zinc-rich primer.

2.2.2.4 Inhibitive coatings

Inhibitive coatings protect the substrate by passivating it. This is achieved through the build-up of a protective layer consisting of insoluble metal complexes, which acts as a barrier against aggressive species. When moisture penetrates the coating, the inhibitive pigment dissolves, releasing anions and cations that penetrate the substrate surface and passivate it by slowing down the anodic and cathodic partial reactions [22]. Thus, the inhibitive coating needs some degree of permeability due to the required solubility and mass transport within the coating. Inhibitive coatings are suitable for the environment with atmospheric corrosion and not recommended for immersion in water [20].

Chromate, phosphate and silicate pigments belong to significant categories of corrosion inhibiting pigments. However, the usage of chromate pigments in paint formulations is being gradually phased out due to concerns over their toxic hazard.

2.2.2.5 Encapsulated pigments

Encapsulated pigment technology aims to achieve a controlled release rate of active components/pigments while also protecting them from early dissolution. The encapsulation process makes the pigments more stable in the coating formulation and typically requires a trigger to release the active components. Encapsulation of inhibitive pigments into mesoporous silica nanoparticles has been reported to provide better barrier properties [23], as the empty capsules can fill the voids that may be generated in case of non-encapsulated inhibitive pigments.

Synthesis of microcapsules is a promising approach for the self-healing of anti-corrosive coatings. The idea involves encapsulating small polymer sequences into micro-sized capsules. When the coating is physically damaged and comes into contact with substances like seawater, the shell of microcapsules dissolves and releases the small polymer sequences. These sequences heal the damaged area via polymerization. However, microcapsule protection technology is not yet mature, and still faces challenges such as producing stable microcapsules, avoiding the formation of undesirable nanoparticles, and preventing excessive agglomeration of microcapsules [24].

2.3 Anti-corrosive coating degradation

2.3.1 Factors affecting anti-corrosive coating degradation

In general, coatings degrade under service when exposed to corrosive media and mechanical damage in the environment. The earliest environmental effects arise from factors such as water diffusion, UV radiation, and media erosion. Cyclic stress applied on coatings in service due to weathering conditions such as humid/dry and high/low temperatures also provokes the degradation of the coating.

2.3.1.1 Water

Water diffusion into anti-corrosive coatings is the primary cause of coating deterioration when exposed to humid environments. Water diffusion into the organic coating can result in blistering, loss of coating adhesion, and corrosion initiation of a metallic substrate under an aerobic environment [25, 26, 27, 28, 29, 30]. Water diffusion into the coating can also cause hydrolysis of the coating resin, resulting in the cleavage of the polymer chain, which can lead to the deformation of the coating. Additionally, the washing action of liquid

water can lead to the loss of gloss and chalking of the coating. It has been reported that coating degradation is faster in pure/distilled water than in 3.5 wt% NaCl solution [17]. However, other research has reported that the extent of water absorption into the coating film decreases as the concentration of NaCl solution increases [31].

2.3.1.2 UV

UV radiation between 295-400 nm is the most damaging spectrum, as this electromagnetic radiation may initiate photooxidation [32]. Photooxidation is the degradation of organic compounds in the coating in the presence of light and oxygen through the formation of free radicals. This structural damage is causing the loss of crosslink density in the coating, which leads to an increase in permeability. The use of additives as UV light absorber (UVAs) can inhibit the photooxidation process and prolong the lifetime of the coating in outdoor exposures. Additionally, polyurethane resin is often applied as the topcoat to prevent UV radiation damage.

2.3.1.3 Temperature

A high temperature acts to accelerate both hydrolysis and propagation steps in photooxidation reactions as they both are thermally activated. A darker coloured coating typically experiences a higher actual temperature than a lighter coloured coating. The absorption of light in a coating formulation can be adjusted by using pigments that absorb more in the infrared region than others. In addition, a high temperature also increases the diffusivity of aggressive species from the environment into the coating which can result in faster coating degradation.

2.3.2 Delamination

Delamination refers to the weakening or loss of adhesion to the substrate or the underlying coating. The loss of adhesion can be a result of either internal stress or internal stress combined with other degradation factors. The factors could be inadequate surface contamination during formulation or incorrect surface preparation [33].

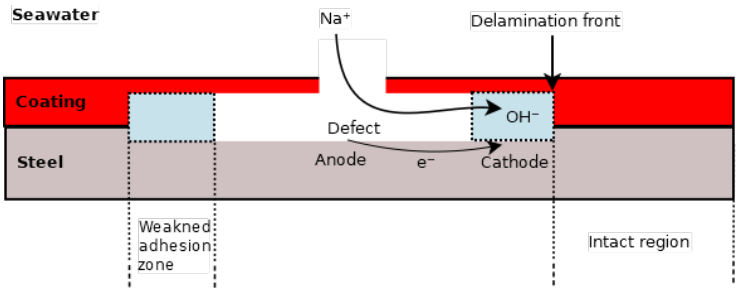

Figure 2.3.1: A simplified illustration of cathodic delamination process in coating-steel interface.

Cathodic delamination mainly occurs in coatings that have physical damage, where corrosion has initiated in the damaged region. Cathodic delamination is a parallel process to corrosion, as illustrated in Figure 2.3.1. Corrosion involves electrochemical reactions of anodic oxidation of irons atoms (Reaction 2.1.5) and cathodic reduction of oxygen to hydroxyl ions reaction (Reaction 2.1.6). The produced hydroxyl ions will increase the local pH, which has been reported to expand the delamination front into the intact coating regions [10, 34, 35]. Accumulation of hydroxyl ions near the cathodic region causes an

imbalance of charge in the coating/metal interface. To re-establish a charge neutral environment, cations from the bulk will migrate to the cathode either along with the interface or perpendicular through the coating. The transport of cations to the delamination front is generally considered to be the rate determining step in cathodic delamination. Furthermore, Sørensen et al. [34] observed experimentally that the delamination rate increases with increasing cation concentration until the concentration of dissolved oxygen at the interface becomes insufficient to maintain the corrosion rate.

2.3.3 Blisters

Blisters are local coating defects that form dome-shaped projections in the coating due to a local loss of substrate adhesion. The blisters may contain liquid or gas. Osmotic blistering can be caused by the presence of soluble salt, pigment or retained solvents. Cathodic blistering is a following damage of the corrosion process which is often seen as a circular pattern of blisters around a defect.

General coating failures under application in marine environments are summarised in Table 2.3.1, and commonly visual coating defects are described in detail by Fitzsimons and coworkers [33]. Nazir and Khan et al. [36] developed a theoretical model for cathodic blister growth, and their simulation results show that increasing the coating thickness is not a significant factor for cathodic blister prevention, whereas an increase of coating flexibility can decrease the disbonding driving force and thereby improve the coating against blistering.

Table 2.3.1: General coating failures under marine environment [9].

Failure type	Failure expressions	Reasons
Alligatoring	Rapid surface curing relative to the underlying layer	Coating cure by oxidation-polymerization if heated
Blistering	Dome- or irregular-shaped projections of the coating film, often filled with water, solvent, caustic, gas, crystals or rust	Contaminants left on the surface-poor surface cleaning
Chalking	Formation of a chalky powder on the surface of the paint	Degradation of the coating due to weathers, Sunshine and moisture
Cracking	Cracking failure at weaker locations	Due to shrinkage in the coating and stress in the coating film Wrong selection of coating for the requirements
Flaking, Chipping or peeling	Section of coating completely lift off the substrate	Due to poor adhesion caused by contamination, improper surface preparation, insufficient mixing and curing
Wrinkling	A rough and crinkled surface	Improper drying and too thick coating film
Orange Peel	Coating surface becomes a orange like skin	High temperature cause by rapid solvent loss or a coating with high viscosity
Telegraphing	Organic coating flow defects	Due to surface tension gradient induced by temperature gradient
Sagging	Irregular and unwanted organic coating material flow on a vertical steel surface	Gravity force
Pinholes	Gas entrapment in coating and premature failures	Malfunctioning application equipment and curing processes
Solvent popping	Bursting of bubbles failures in the coating	Evaporation by solvent gas bubbles in the coating
Over spray	Wet particles falling on the previously painted area adjacent	Incorrect spray application or spray under windy conditions

2.4 Analysis and testing of anti-corrosive systems

2.4.1 Accelerated laboratory testing

Accelerated exposure testing is commonly used to quickly evaluate the coating performance in a matter of weeks and months. The environment of the accelerated exposure testing is often made more aggressive by increasing or decreasing temperature, decreasing pH, increasing the concentration of corrosive agents, increasing UV exposure, and deliberately inducing mechanical damage to the coating. To select the appropriate accelerated test protocols for estimating field exposure, consideration should be given to the local climate. For example, exposure in Miami and Florida can be considered as 4 times [22] harsher compared to European climates in terms of field exposure. Hence, different standards protocols are applicable, such as ISO (International Organisation for Standardisation) and ASTM (American Society for Testing and Materials), and the selection of standards should be made in the context of the required environment for the coating to achieve representative experimental data. Table 2.4.1 summarises some commonly used exposure protocols for protective coating performance determination. However, results from accelerated tests should be used with caution, as accelerated tests will not include all natural exposure factors.

Table 2.4.1: Examples of accelerated laboratory tests from ISO standards.

Test Method	Protocols	Comments
Neutral Salt Spray	ISO 9227	Exposure of samples to a 5 wt% NaCl fog with neutral pH at 25°C
QUV	ISO 16474-3	Artificial cabinet UV exposure. UV sources used include carbon arc-, xenon arc- and fluorescent UV lamps for spectral between 250-400 nm
Cathodic Disbondment	ISO 15711	Testing coating disbondment under full immersion in sea water. Determining the ability of coatings to withstand cathodic disbonding.
Immersion	ISO 2812-2	Evaluation of coatings resistance to liquid/water with partly or fully immersion.
Water condensation	ISO 6270-1	Water resistance testing

2.4.1.1 Accelerated cyclic test

The traditional salt spray exposure test and/or humidity test are not adequate for selecting coating systems used for offshore structure applications. Therefore, standard protocols for accelerated cyclic testing have been developed to provide a basic selection of high-quality coating systems. In ISO 12944-9:2018, specialised laboratory test methods of coating systems used for offshore structures have been introduced. According to the qualification test defined in ISO 12944-9, a coating system used in extremely corrosive (CX) environment must pass a duration of 4200 hours in the cyclic ageing test specified in Table 2.4.2, and a coating system used in CX and Im4 environments have to pass 4200 hours of all test methods defined under ISO 12944-9. For a qualified coating system applies in immersion

category Im4, 4200 hours of test duration is required for both cathodic disbonding and seawater immersion.

NORSOK M501 is a standard developed in Norway. The laboratory accelerated cyclic test specialised for offshore coating system selection is summarised in Table 2.4.2. The main difference between ISO 12944-9 and NORSOK M501 is the immersion test and a freezing cycle which are included in ISO 12944-9 whereas in the NORSOK M501 the drying process in the air is included under the cyclic test. Knudsen et al. [37] compared different accelerated cyclic tests with real field testing. Their results revealed that drying and wetting processes indicating to contribute a better correlation between accelerated laboratory testing and real field testing. Moreover, a higher cyclic frequency of the exposure conditions has also been reported to better simulate coating degradation under natural exposures [38].

Table 2.4.2: ISO 12944-9 and NORSOK M501 define the accelerated cyclic tests for coating systems used for stainless steel in submerged and splash zones

Test Method	Protocols	Comments
	ISO 12944-9	
Cyclic Ageing test	ISO 16474-3 ISO 9227	a) 4h exposure to UV-340 lamps at (60±3)°C and 4h exposure to condensation at (50±3)°C b) 72 h of exposure to neutral salt spray: 5% NaCl fog with neutral pH at 25°C c) 24h exposure to low temperature (-20 ± 3)°C
	NORSOK M501	
Cyclic test	ISO 7253 ATSM G53	a) 72 hour exposure to salt spray b) 16h drying in air c) 80h exposure to UV-A 340nm weatherometer
Cathodic Disbondment	ASTM G8	Testing coating disbondment under full immersion in sea water. Determining the ability of coatings to withstand cathodic disbonding.
Prohesion Testing	ASTM G85 Annex 5 [39]	a) 1h exposure of continues fog of diluted acidified electrolyte of 0.4 wt% $(NH_4)_2SO_4$ + 0.05 wt% NaCl at 21°C-27°C b) 1h drying at 35°C

2.4.2 General laboratory characterisation methods

The standardised coating degradation evaluations of different defects are summarised in Table 2.4.3, which defines the degree of a defect by assessing quantity, size and intensity. It is observed that most of the evaluation methodologies used herein are destructive and rely heavily on visual inspection, which can be subjective.

Table 2.4.3: ISO standards summarising coating degradation features evaluation.

Evaluation method	Protocols	Methodology	Results
Pull off	ISO 4624	Destructive	Coating adhesion test
Blistering	ISO 4628-2	Visual image assessment	Degree of blistering
Rusting	ISO 4628-3	Visual image assessment	Degree of rust broken through
Delamination and Corrosion around a defect	ISO 4628-8	Destructive	Degree of rust creep
Filiform corrosion	ISO 4628-10	Visual image assessment	Degree of filiform corrosion

2.4.3 Field testing

Field testing allows for a more accurate assessment of coating system performance and durability in actual environments, as it takes into account various factors such as weather, temperature, and exposure to corrosive agents that cannot be replicated in a laboratory setting. By conducting field testing, coating system manufacturers and users can gain confidence in the performance and reliability of the coating system, and make informed decisions about their selection and use. However, field testing has the disadvantage of being a time-, manpower- and resources-consuming process. Despite these challenges, field testing of coating systems is still relevant as it aims to collect coating performance data under real conditions. These data can be used to validate the results obtained from accelerated laboratory testing [37, 40], estimate the acceleration factor [41], or develop coating performance prediction models [42, 43].

2.5 Non-destructive evaluation techniques

Non-destructive evaluation (NDE) techniques can be used to assess the quality and integrity of coatings without causing damage to the coating or the substrate. These techniques use various physical principles, such as electromagnetic waves, sound waves, and thermal imaging, to detect and analyse coating defects, thickness, and adhesion. Some of the commonly used NDE techniques for coating assessment include scanning electron microscopy (SEM), Attenuated Total Reflectance Fourier-transform infrared spectroscopy (ATR-FTIR), optical 3D profilometry, Electrochemical impedance spectroscopy (EIS) and scanning acoustic microscopy (SAM). These techniques provide a non-destructive and cost-effective way to assess coating performance and detect deterioration before they become critical.

2.5.1 Scanning Electron Microscopy

Scanning Electron Microscopy (SEM) is an imaging technique that can be used to assess the surface topography and morphology of a sample at high resolution. The SEM consists of several components, including an electron gun, a vacuum chamber, and a detector. The electron gun generates a beam of electrons, which is focused onto the sample by a set of electromagnetic lenses. As the electrons hit the sample, some of them are scattered back or absorbed, producing a signal that is detected by a detector. The detected signal is then used to create an image of the sample surface.

The resolution is typically in the range of 1-20 nanometers. SEM can also provide information about the sample's elemental composition by using an energy-dispersive X-ray spectroscopy (EDS) detector. EDS works by detecting X-rays that are emitted from the sample when it is bombarded with electron beams. The X-rays carry information about the elements present in the sample, allowing researchers to identify the sample's chemical composition.

In summary, SEM is able to scan a solid material's surface from milimeter to nanometer scale and also provides atomic distribution analysis on the examined surface.

2.5.2 Attenuated Total Reflectance Fourier Transform Infrared Spectroscopy

Attenuated Total Reflectance Fourier Transform Infrared Spectroscopy (ATR-FTIR) is used to identify and quantify chemical bonds and functional groups in a wide range of samples, including liquids, solids, and gases. ATR-FTIR is based on the interaction between infrared radiation and the molecules in a sample, causing certain types of vibrations that are characteristic of different chemical bonds and functional groups. ATR-FTIR spectroscopy involves placing a sample in contact with a crystal, such as diamond or zinc selenide, which has a high refractive index. The sample is then exposed to infrared radiation, which is directed into the crystal and undergoes total internal reflection.

As the infrared radiation penetrates the sample at a shallow angle, it interacts with the molecules at the surface of the sample. The resulting vibrations are transmitted back to the crystal, where they are detected by a detector. The intensity of the resulting spectrum is then measured and analysed to identify the chemical composition of the sample.

ATR-FTIR has several advantages over other spectroscopic techniques. It is non-destructive and requires minimal sample preparation, making it useful for analyzing small or fragile

samples. It can also be used to study samples in situ or under different environmental conditions. Additionally, ATR-FTIR spectra are highly reproducible and can provide detailed information about the chemical composition of a sample, including the identity and concentration of individual elements.

2.5.3 3D profilometry

3D profilometry is a non-contact surface metrology technique that measures the surface topography of an object in three dimensions. It is used to analyze surface roughness, flatness, waviness, and other geometric features.

The basic principle behind 3D profilometry is to measure the height of the surface at different points, which are then used to construct a 3D model of the surface. This is typically done using a profilometer, which uses the white light scanning technique to capture surface images and then uses a confocal optical system to create a 3D representation of the surface.

Overall, 3D profilometry is a powerful tool for analyzing surface topography.

2.5.4 Open circuit potential

Open Circuit Potential (OCP) is a widely used electrochemical technique to assess the corrosion potential and the tendency of materials to corrode in a given environment. The OCP measures the voltage difference between a metallic material and a reference electrode and determines the tendency of the metal to corrode spontaneously in the given environment. In the coating degradation studies, the OCP is often applied for the study of zinc-rich primer degradation whereas based on the measured OCP value of the system, the effectiveness/protection duration of zinc-rich primer coated on a metallic substrate can be estimated by knowing the difference between zinc and iron corrosion potentials/OPC as shown in Figure 2.1.4.

In practice, OCP measurement is often used in combination with other electrochemical techniques such as electrochemical impedance spectroscopy to examine the stability of the system before measurement.

2.5.5 Electrochemical Impedance Spectroscopy

Electrochemical impedance spectroscopy (EIS) has been applied for decades to assess the corrosion resistance and performance of coating materials [44, 25, 45, 46]. The EIS technique involves placing the coated metal sample in an electrolyte solution, which is typically a saline solution that simulates the corrosive environment. A small AC (alternating current) voltage is then applied to the sample surface, and the resulting current response is measured. EIS measures the impedance of the coating system, providing information about the electrical resistance that hinders the flow of electrons. This information can be interpreted as an indication of the barrier properties of the coating system.

In coating evaluation, EIS can be used to detect changes in the coating properties due to environmental exposure such as humidity, temperature, and UV radiation. EIS can also provide information about the effectiveness of a coating system, such as the presence and thickness of a barrier layer, and the coating's ability to prevent corrosion. Overall, EIS is a powerful tool for evaluating the performance of coatings in terms of their barrier properties.

2.5.5.1 Impedance

EIS works by applying an small alternating current (AC) or voltage to a coated metal surface and measuring the resulting current as [47]:

$$I(t) = C\frac{dE(t)}{dt}$$

where $I(t)$ is current as function of time t, C is the capacitance and $E(t)$ is the voltage as a function of time.

By varying the frequency of the applied voltage to the conducting system, resulting in a characteristic electrical response known as impedance. Impedance provides information about the coating's electrical properties and corrosion resistance. Impedance is defined as the applied voltage divided by the current and can also be described by complex quantities expressed as the sum of real and imaginary parts:

$$Z = \frac{E(t)}{I(t)} = a + bj$$

where $j = \sqrt{-1}$, a is the real part of impedance Z and b is the imaginary part of Z. The impedance is a point in the complex plane as shown in Figure 2.5.1. The complex number can be interpreted with a polar from:

$$\begin{aligned} Z &= r(\cos\varphi + j\sin\varphi) \\ a &= r\cos\varphi \\ b &= r\sin\varphi \\ r &= |Z| = \sqrt{a^2 + b^2} \\ \tan\varphi &= \frac{b}{a} \end{aligned}$$

where r represents the magnitude of the number (modulus) and φ is the phase angle in radians (argument).

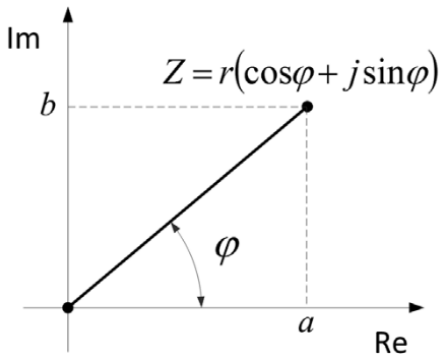

Figure 2.5.1: Graphically illustration of impedance adapted in [47] where r represents the magnitude of the number (modulus) and φ is the phase angle in radians (argument). The impedance Z is a point in the complex plane.

The impedance can also be expressed in exponential form by applying Euler's formula:

$$Z = r(\cos\varphi + j\sin\varphi) = re^{j\varphi}$$

2.5.5.2 Electrical components

Electrical components such as resistors, capacitors and inductors are needed in electrical circuit models to accurately describe and analyse the behaviours of electrical systems. These components' behaviour can often be mathematically modelled using the fundamental principle of electricity.

Resistor

For a resistor, the current and voltage are always in phase as shown in Figure 2.5.2a and there is no imaginary component to the impedance. Thus, the impedance of a resistor is equal to the resistance.

$$Z_R = R,$$

where Z_R is impedance of a resistor and R is resistance. The impedance diagram for a resistive component exhibits a single straight line on its real axis that approaches infinity depending on the time and frequency domain.

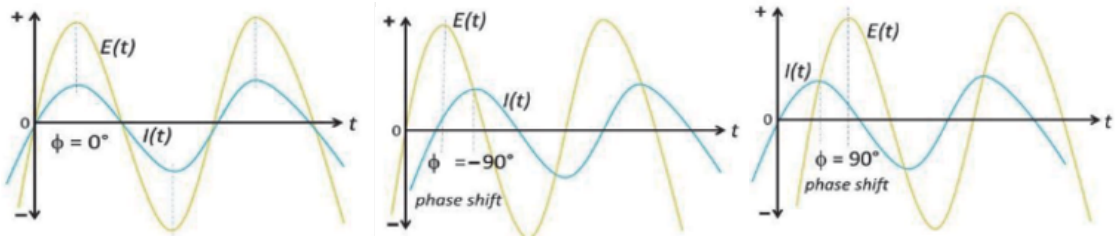

(a) A resistor (b) A capacitor (c) A Inductor

Figure 2.5.2: Phase shift angle responds between voltage ($E(t)$) and current ($I(t)$) profiles for electrical components of (a) Resistor (R) (b) Capacitor (C) and (c) Inductor (L) adapted in [48].

Capacitor

A pure capacitor (C) represents a component with the capacity to store electrical charge and would have a phase shift angle of -90° as shown in Figure 2.5.2b describing the sinusoidal response of voltage is retroceded at least by -90° which gives an imaginary component dependent on time and frequency. The impedance of a capacitor is given:

$$Z_C = -\frac{1}{j\omega C}, \quad \omega = 2\pi f$$

where ω is the angular frequency.

Inductor

An inductor (L) is the opposite case of a capacitor and it occurs when the phase shift of the current waveform signal to 90° as shown in Figure 2.5.2c with the impedance given as:

$$Z_L = j\omega L$$

Constant phase element

A constant phase element (CPE) is a mathematical expression which is often applied to

replace the capacitor element since a pure capacitor is often unsuitable in describing real systems. In the case of coating performance analysis, a CPE element is often applied in the electrical circuit model instead of a pure capacitor due to surface inhomogeneity, electrode porosity surface disorder, geometric irregularities etc. The impedance of a CPE is given as:

$$Z_{CPE} = \frac{1}{Y(j\omega)^n}$$

where Y and $n \in [0; 1]$ are the admittance and exponent constant of CPE, respectively. The CPE element has been utilised to represent a circuit parameter with limiting behaviour as an ideal capacitor for $n = 1$, a resistor for $n = 0$ and an inductor for $n = -1$ [49]. These different distributions of CPE underlined an unclear physical meaning of this circuit element.

2.5.5.3 EIS data presentation

EIS raw data consists of real and imaginary impedance values measured at predetermined frequencies. These values are typically represented in a Nyquist or a Bode plot as illustrated in Figure 2.5.3. The Bode plot shows the magnitude (blue curve) and phase angle (red curve) of the impedance as a function of frequency as shown in Figure 2.5.3a.

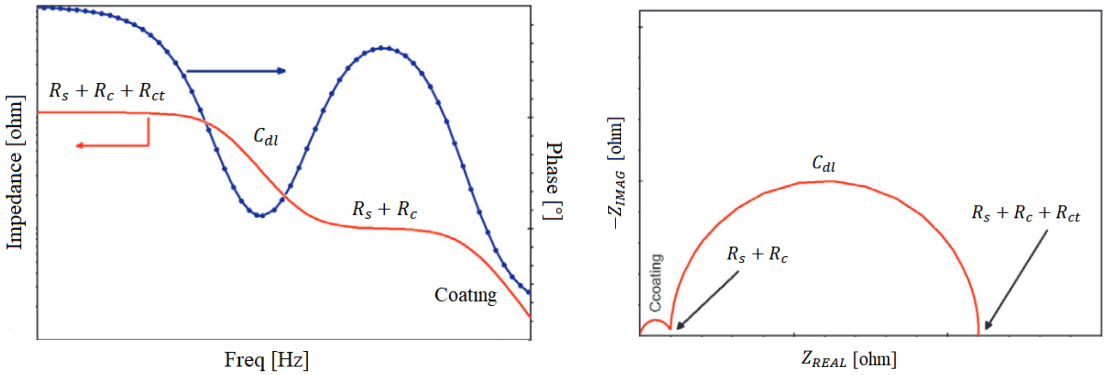

(a) A Bode plot (b) A Nyquist plot

Figure 2.5.3: Illustration of curve trajectories of a Bode plot (a) and a Nyquist plot (b) adapted in [50].

The Nyquist plot is often a semicircle that shows the real and imaginary parts of the impedance as illustrated in Figure 2.5.3b. Ideally, the number of semicircles on the Nyquist plot should be equal to the number of extrema on the phase-frequency curve in the Bode plot. From the impedance-frequency curve on the Bode plot, the regions dominated by resistance appear a slope of zero and regions dominated by capacitances appear a slope of negative values (ideally -1) as shown in Figure 2.5.3a.

Two semicircles are observed in the Nyquist plot (Figure 2.5.3b) corresponding to two separated time constants occurring in the examined system. In the case of the coated metallic sample, the electrolyte resistance R_s can be read as the first x-axis interception on the Nyquist plot, while the sum of coating pore resistance R_c and R_s can be read on the

x-axis as the end of the first semi-circle. Graphically, the diameter of an ideal semicircle on the Nyquist plot gives the value of capacitance as:

$$C_{dl} = \frac{1}{\omega_{max} R_{ct}}$$

2.5.5.4 EIS data interpretation

Interpretation of EIS raw data involves fitting an equivalent circuit model (ECM) to the measured impedance spectrum. The equivalent circuit model consists of a combination of electrical components that represent the physical and chemical processes occurring in the electrochemical system. The parameters obtained from the fitting process provide information about the electrochemical behaviour of the system. Some commonly applied ECM models for coating analysis are presented in Figure 2.5.4.

ECM1 show the arrangement of a resistor (R_1) connected in parallel to a capacitor (C_1) and then connected in series with another resistor (R_s) as shown in Figure 2.5.4a. The impedance response of ECM1 model can be expressed as a function of frequency in the following:

$$Z_{\text{ECM1}} = \frac{R_1}{1 + (j\omega C_1 R_1) + R_s}$$

The ECM1 model is also known as Randles circuit and it is typically applied to describe an ideal intact paint film [50], where R_1 and C_1 describing coating properties and R_s is the electrolyte resistance.

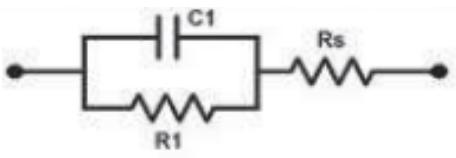

(a) ECM1: R(RC)

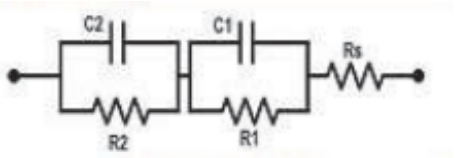

(b) ECM2: R-RC-RC

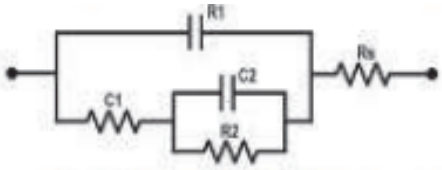

(c) ECM3: R(RC(RC))

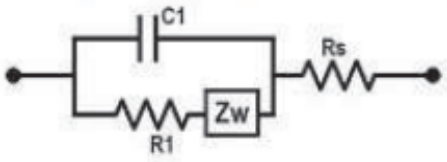

(d) ECM4: R(RC(W))

Figure 2.5.4: Equivalent circuit models used to describe the electrochemical processes adapted in [48].

Two time constants could be expected in ECM2 model with a combination of parallel RC in series and ECM3 model with a parallel arrangement of RC in parallel connection, respectively. These ECM models are used to model the impedance response for coated-metallic samples under exposure. Where C_1 is the capacitance of coating or oxide film connected in parallel to R_1 that is the coating or oxide resistance, both connections in series or parallel to another RC components contribute to the electrical response of the

inner barrier layer or the double layer interface (coating or oxide/metal interface). The capacitance of coating C_c depends on it's dielectric constant ε and its thickness l given by:

$$C_c = \frac{\varepsilon_0 \varepsilon A}{l} \tag{2.5.1}$$

where $\varepsilon_0 = 8.854 \cdot 10^{-12} \frac{\mathrm{F}}{\mathrm{m}}$ is the electrical permittivity constant of free space and A is the coated area exposed to the electrolyte.

ECM4 model is derived from ECM1 by adding a Warburg diffusion component Z_W in series of the resistor R_1. Z_W describes the diffusion control phenomenon in the studied system which can happen when the concentration of an electrochemically active species changes during the AC cycle. The Warburg diffusion component is very characteristic and it appears as a straight line tail with 45 ° angle to the abscissa would be observed on the Nyquist plot [48].

Accurate analysis and validation of EIS data rely heavily on the fitting of mathematical models, specifically equivalent circuit models. These critical and challenging processes enable the acquisition of important electrical parameters that can be used to determine the corrosion rate of the material under investigation and its electron charging capacity. Ultimately, EIS aims to obtain information about the system and its evolution over time, achieved through the application of a sinusoidal voltage in a range of frequencies.

2.5.6 Scanning Acoustic Microscopy

Scanning Acoustic Microscopy (SAM) utilising high-frequency sound waves to create images of the interior of a material and interface between materials. SAM has been widely applied for the assessment of materials in composite structures, chip manufacturing and bio-pharmaceutical industries. Recently, SAM has also been applied for coating failure studies of delamination [51, 52, 53, 54] and blistering [51, 55].

2.5.6.1 Basic principles of SAM

SAM consists of an ultrasonic emitting transducer, a mechanical scanner and an image processor. The transducer acts both as a lens and detector that delivers and focuses the acoustic waves produced by the piezoelectric array, while also detecting the reflected echo that originates from the sample as illustrated in Figure 2.5.5. The acoustic sound wave will freely propagate in liquids and solids, and when it encounters an interface between two materials, a reflection occurs due to the difference in velocities of the sound waves within these two materials. Additionally, a water coupling medium between the transducer and the sample is very important for the efficient delivery of acoustic sound waves. The reflected signal (echo) is collected and converted into an electrical signal with spatial coordinates. The electrical voltage is amplified and digitized using an image processor. The scanning motion of the transducer on the sample surface would collect the acoustic echo signals at each point and the depth information is also stored. Recording the duration of time is also crucial to consider the transition time (t) of reflections within the sample that occur during a series of acoustic excitations.

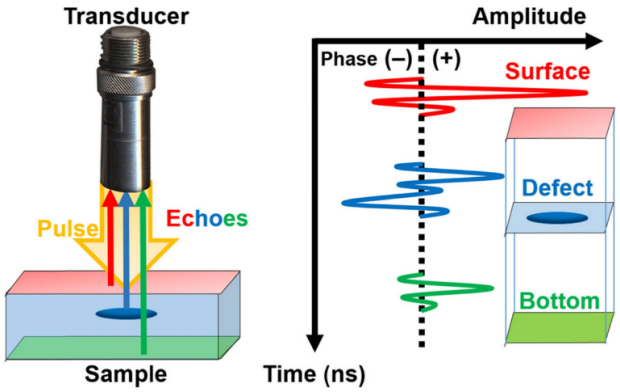

Figure 2.5.5: Schematic showing the incident and reflected ultrasonic pulse (left) and histogram (right) showing the amplitude of the reflected echo (A-scan) after an ultrasonic pulse interacts with a sample adapted [56].

Figure 2.5.5 illustrates the reflection mode SAM applied to a material that includes defects such as grain boundaries, cracks, delamination, voids bubbles, and contaminants. The ultrasonic pulse generated from the transducer is delivered to the sample through a water medium. During this process, some of the pulses would be reflected at the sample surface (red arrow in Figure 2.5.5) because of the change of the acoustic impedance between water and sample surface.

The acoustic impedance (Z_{SAM}) is defined as the amount of resistance an ultrasound beam experiences as it passes through an examined material, which is given by:

$$Z_{SAM} = \rho \cdot v$$

where ρ is material density $\left(\frac{kg}{m^3}\right)$ and v is the velocity of sound within the material $\left(\frac{m}{s}\right)$.

As shown in Figure 2.5.5, when an ultrasound beam reached an interface between two materials, some of the energy is reflected back and some amount is further transmitted through the interface. The ratio of the reflected waves to the transmitted waves is determined by the impedance difference between the two materials. The ultrasound intensity (I) or the amount of the reflected and transmitted waves can be evaluated by using reflection coefficient R_{SAM} expressed as [57]:

$$R_{SAM} = \frac{I_R}{I_0} = \frac{(Z_{SAM,2} - Z_{SAM,1})^2}{(Z_{SAM,2} + Z_{SAM,1})^2}$$
$$T_{SAM} = \frac{I_T}{I_0} = 1 - R_{SAM} = \frac{4Z_{SAM,2} \cdot Z_{SAM,1}}{(Z_{SAM,2} + Z_{SAM,1})^2}$$

where $Z_{SAM,1}$ and $Z_{SAM,2}$ are the acoustic impedance of 1st and 2nd material and T_{SAM} is transmission coefficient. The higher the acoustic impedance difference between two materials, the larger the intensity of the reflection the brighter would be the obtained pixel. In practice not only do reflection and transmission occur, but the ultrasound beam into a material can also be attenuated by diffraction, scattering, and adsorption.

As illustrated in Figure 2.5.5, the acoustic pulse passes through three boundaries - surface, defects, and bottom - allowing for the time-of-flight (t) of the pulse reflected from each surface to provide the sample's depth information. A series of reflected waveforms are recorded and designated as an A-scan of the reflection mode in the SAM. The ultrasonic wave experiences a phase inversion at the interface of the high and low acoustic impedance region, which results in three consecutive amplitudes of the signal.

2.5.6.2 The SAM analysis modes

The three basic scanning analytical modes of SAM applied for material characterisation are A-scan, B-scan and C-scan as illustrated in Figure 2.5.6.

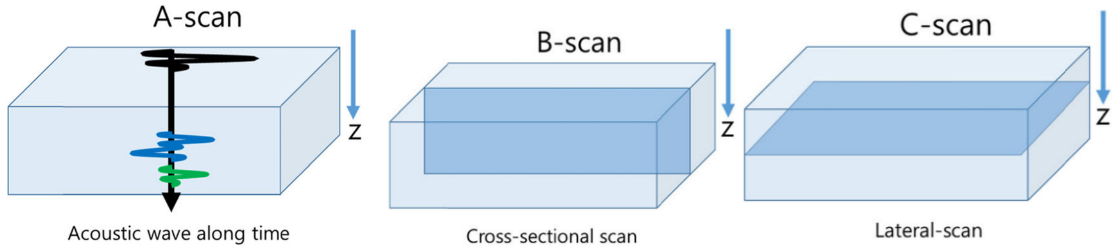

(a) A-scan (b) B-scan (c) C-scan

Figure 2.5.6: Different types of scanning analytical modes of SAM adapted in [56].

The A-scan mode is a raw waveform that records the amplitude of the echo along the ultrasonic transit time. When operating in this mode, the optimal conditions are maintained by adjusting the amplitude to the maximum so that the transducer is focused on the desired point. The depth information of a defect in the material can be determined by the following relation [56]:

$$d = \frac{t \cdot v}{2}$$

where d is distance inside the material, t is the time of flight for echo signal reflection, v is the velocity of sound within the material and factor 2 accounts for the round trip of the sound wave.

Once the scanning process in the A-scan mode has been conducted, acoustic images can be processed further using a B-scan or a C-scan. The B-scan mode provides a cross sectional view through the material which enables the extraction of the depth information of the material. When performing a C-scan, a single image of the target layer at a specific depth is captured. Regardless of the scan mode being used, it is crucial to move the transducer along each vertical axis until the echo signal is reflected at a moderate intensity for the region of interest to achieve the best SAM scanning results.

The advantage of SAM lies in its ability to visualise the internal structure of a non-transparent solid material below its surface, due to the favourable propagation properties of acoustic waves. Additionally, SAM offers an efficient non-destructive inspection method for detecting defects, failures, delaminations, and cracks at various depths within a material. This makes it interesting to apply SAM for the assessment of various coating defects and degradation in real time.

2.6 Summary

Corrosion in steel structures exposed to aggressive marine environment is a significant degradation phenomenon that leads to economic, environmental and safety issues. The corrosion process in coated steel structures evolves over time and is influenced by environmental factors such as humidity, temperature, salinity, pH, and wet/dry or thermal cycles. The organic coating systems commonly used for corrosion prevention in offshore and marine environments consist of a combination of sacrificial and barrier protection coatings. The evaluation methods applied for coating performance assessment are still dominated by visual imaging and destructive methods, which are manpower- and resources demanding tasks. These destructive and visual evaluation techniques also suffer from subjective predetermined evaluation, only detecting severe (visual) corrosion failures and limiting the study of initial coating deterioration and coating degradation over time.

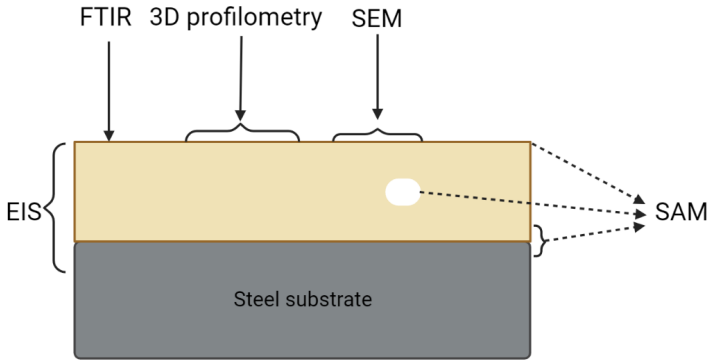

Figure 2.6.1: Sketch of NDT application range applied on coated steel substrate.

To contribute these lacking areas, non-destructive techniques are in focus to be applied to study the coating degradation over time. Figure 2.6.1 provides an overview of the NDT techniques discussed in the literature survey. ATR-FTIR measures changes in functional groups on the coating surface by analysing the absorbance of infrared light. However, its limitation lies in assessing surface changes at a single point, and the assumption is often made that the localised results represent the entire surface. 3D profilometry can monitor changes in coating topography and height profile over a large surface area with micrometer resolution. SEM provides detailed coating morphology at the nanometer scale, and EDX analysis allows examination of elemental distribution on the material surface. EIS provides information on changes in the barrier properties of the entire coating layer, but advanced ECM models are required for mechanism studies of coated steel.

SAM scanning, with a resolution down to 10 µm, offers information about interfaces between two materials by analysing differences in sound velocities. Based on these introduced NDT techniques, three objectives are formulated in this project to study the early degradation of commercial coatings exposed in different environments, as specified in Section 1.2.

3 Electrochemical Impedance Evaluation of coating performance

3.1 Introduction

The evaluation of coating performance is crucial for ensuring the protection of substrates against corrosion in various environments. Coatings act as a protective barrier, preventing the interaction of aggressive species with the underlying substrate. Among the various techniques available for coating evaluation, Electrochemical Impedance Spectroscopy (EIS) has gained significant attention [58] due to its non-destructive nature and ability to provide valuable insights into the coating behaviour. EIS involves the application of an alternating current (AC) potential to the coated system and measuring the resulting impedance response. This technique enables the assessment of coating properties such as barrier effectiveness, corrosion resistance, and degradation mechanisms. By analyzing the impedance spectra, valuable information about the electrochemical processes occurring at the coating/substrate interface can be obtained.

The objective of this chapter is to utilise EIS as a tool for evaluating different types of coatings, with a particular focus on zinc-rich epoxy primers and epoxy barrier coatings. The selected exposure environments for investigation are neutral salt spray and field conditions. By exposing the coatings to these environments, it becomes possible to observe their behaviour and degradation patterns under accelerated and realistic conditions, respectively. These two types of coatings have distinct protective mechanisms and exhibit different behaviour during EIS measurements. By studying their impedance responses, a comprehensive understanding of their performance and behaviour can be achieved.

The sacrificial protection duration of zinc-rich primers can be monitored by analyzing the evolution profile of the Open Circuit Potential (OCP) during EIS measurements. Additionally, the impedance modulus (|Z|) can provide insights into the barrier properties.

On the other hand, epoxy barrier coatings primarily rely on their barrier properties to prevent the penetration of aggressive species to the coating/substrate interface. EIS measurements offer valuable information regarding the impedance modulus of these coatings, which reflects their ability to impede the aggressive species that activate the electrochemical corrosion processes.

By comparing the EIS responses of zinc-rich epoxy primers and epoxy barrier coatings, a deeper understanding of their distinct behaviour and performance can be achieved, highlighting the differences in their impedance characteristics. Understanding the behaviour of these coatings through EIS measurements is crucial for optimising their formulation, improving their protective performance, and ensuring their long-term durability. Ultimately, this work aims to contribute to the development of more effective and reliable coating systems for corrosion protection.

3.2 Experiment

3.2.1 Sample preparation

Two commercial organic coating systems, namely zinc-rich epoxy primer (ZnEP) and epoxy barrier coating (EP-01), both cured with aromatic amine adduct, were airless sprayed onto S235JR steel panels that were sandblasted to a cleanness of Sa½ (ISO 8501) and had dimensions of 75 mm x 150 mm x 3 mm. The back side and edges of the panels were sealed with a two-component commercial epoxy coating and left to cure in a fume hood for at least 7 days. The cured samples were then stored in sealed plastic bags to minimise contact with the environment before testing. To ensure electrical flow during electrochemical impedance spectroscopy (EIS) measurements, a wire was connected to the steel panel, and the wire connection spot was sealed with epoxy glue to protect it from corrosion. The dry film thickness (DFT) of each sample was measured using an Elcometer 355 Coating Thickness Gauge and is presented in Table 3.2.1.

Table 3.2.1: Prepared samples with the corresponding coating system and measured dry film thickness DFT.

Sample No.	Coating system	Average DFT	Environment
S2	ZnEP50	52 µm($\pm$3)	Salt spray
S3	ZnEP50$_{rep}$	59 µm($\pm$5)	Salt spray
S4	ZnEP50$_{rep}$	52 µm($\pm$3)	Salt spray
S12	ZnEP80	84 µm($\pm$6)	Salt spray
S13	ZnEP80$_{rep}$	82 µm($\pm$7)	Salt spray
S31	EP50	67 µm($\pm$3)	Salt spray
S32	EP50$_{rep}$	60 µm($\pm$4)	Salt spray
S33	EP50$_{rep}$	71 µm($\pm$6)	Salt spray
S41	EP50$_{rep}$	127 µm($\pm$4)	Salt spray
S43	EP50	103 µm($\pm$4)	Salt spray
S5	ZnEP50F	54 µm($\pm$6)	The field
S6	ZnEP50F$_{rep}$	50 µm($\pm$6)	The field
S7	ZnEP50F$_{rep}$	47 µm($\pm$10)	The field
S14	ZnEP80F$_{rep}$	91 µm($\pm$6)	The field
S15	ZnEP80F	91 µm($\pm$4)	The field
S16	ZnEP80F$_{rep}$	101 µm($\pm$4)	The field
S34	ZnEP50F	68 µm($\pm$4)	The field
S35	ZnEP50F$_{rep}$	67 µm($\pm$7)	The field
S36	ZnEP50F$_{rep}$	59 µm($\pm$3)	The field
S44	ZnEP80F	90 µm($\pm$3)	The field
S45	ZnEP80F$_{rep}$	94 µm($\pm$3)	The field
S46	ZnEP80F$_{rep}$	111 µm($\pm$10)	The field

3.2.2 Exposure

3.2.2.1 Salt spray test

The samples were subjected to an accumulated exposure time of 450 hours in a neutral salt spray chamber (in accordance with ISO 9227:2017) containing a 5 wt.% NaCl solution at 35 °C. Periodically, samples were removed from the chamber for electrochemical impedance spectroscopy (EIS) measurements to monitor the extent of coating degradation over the exposure period.

3.2.2.2 Field exposure

The same coating systems were exposed on a floating raft at CoaST Maritime Test Centre (CMTC) located in Hundested, Denmark [59]. The field exposure was initiated in April 2021 and lasted up to 15 months of accumulated exposure time with methodological data presented in Figure 3.2.2. The exposed samples were periodically retrieved from the site and transported to the laboratory for EIS measurements. Nonetheless, it is assumed that the coating systems' degradation characteristics remain unaltered despite the intermittent removal of roughly one week from the field and stored in room conditions.

3.2.3 OCP measurement

OCP is monitored for each examined sample to ensure the stability of the coating system immersed in 3.5 wt.% NaCl electrolyte before running the EIS measurement. Additionally, the OCP value of zinc-rich epoxy system is essential for estimating the duration of sacrificial protection provided by zinc particles in the formulation.

3.2.4 EIS measurement

EIS measurements were conducted using a Gamry Reference 600+ potentiostat. The measurements were taken within a frequency range of 10 mHz or 50 mHZ to 100 kHz, utilizing a sinusoidal voltage with an amplitude of 10-20 mV.

The three-electrode configuration presented in Figure 3.2.1 consisted of a coated steel panel as the working electrode (WE), graphite as the counter electrode (CE), and a saturated calomel electrode (SCE) as the reference electrode. A glass cylinder was affixed to the coated sample and sealed with a rubber ring to hold the electrolyte of 3.5 wt.% NaCl solution at 25 °C. The exposed area of coated samples to the electrolyte is at 10 cm^2, controlled by a cell sticker. The sample setup, connected to the potentiostat, was placed inside a Faraday cage to avoid external interference signals. The exposure duration in the salt spray for each coating system varied and the experiments were stopped when the measured OCP value stabilised above -0.78 V/SCE for zinc-rich primer exposed to the neutral salt spray.

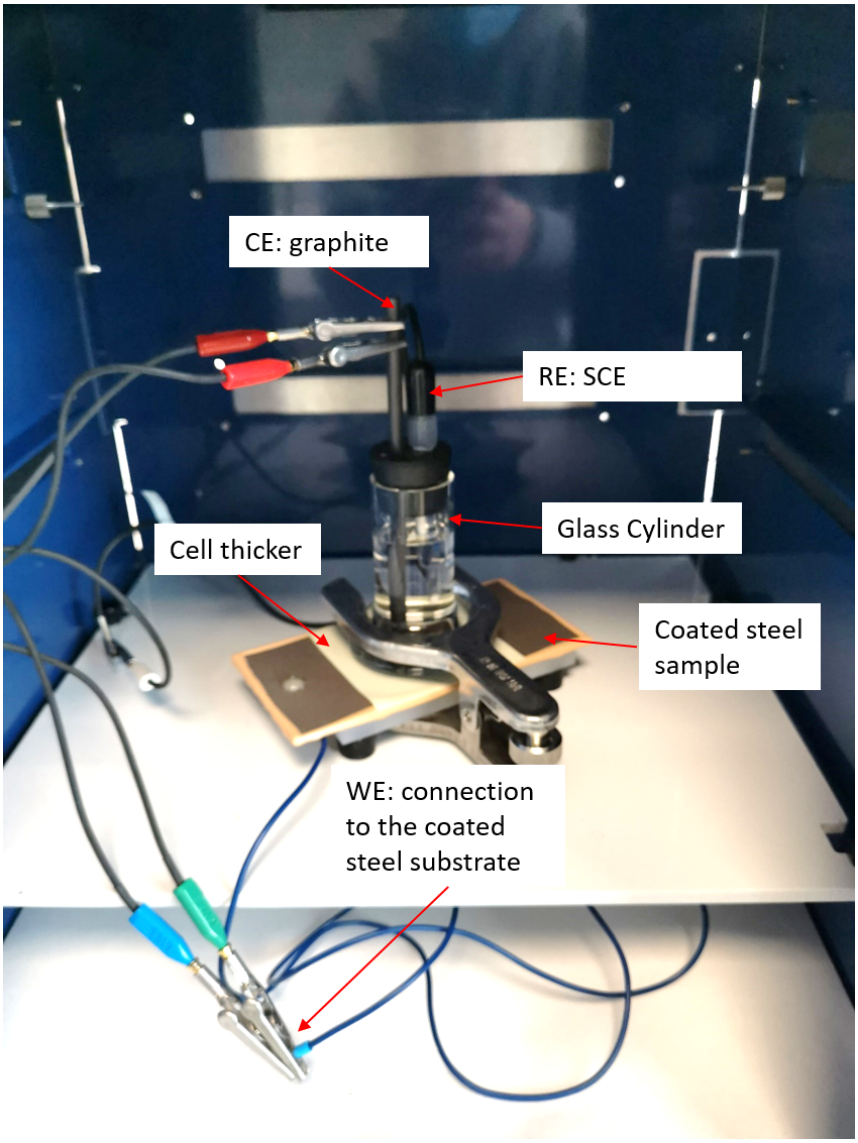

Figure 3.2.1: Illustration of the three-electrode configuration for EIS measurement of a coated steel sample placed inside a Faraday cage with electrodes connected to a potentiostat which is outside the Faraday cage.

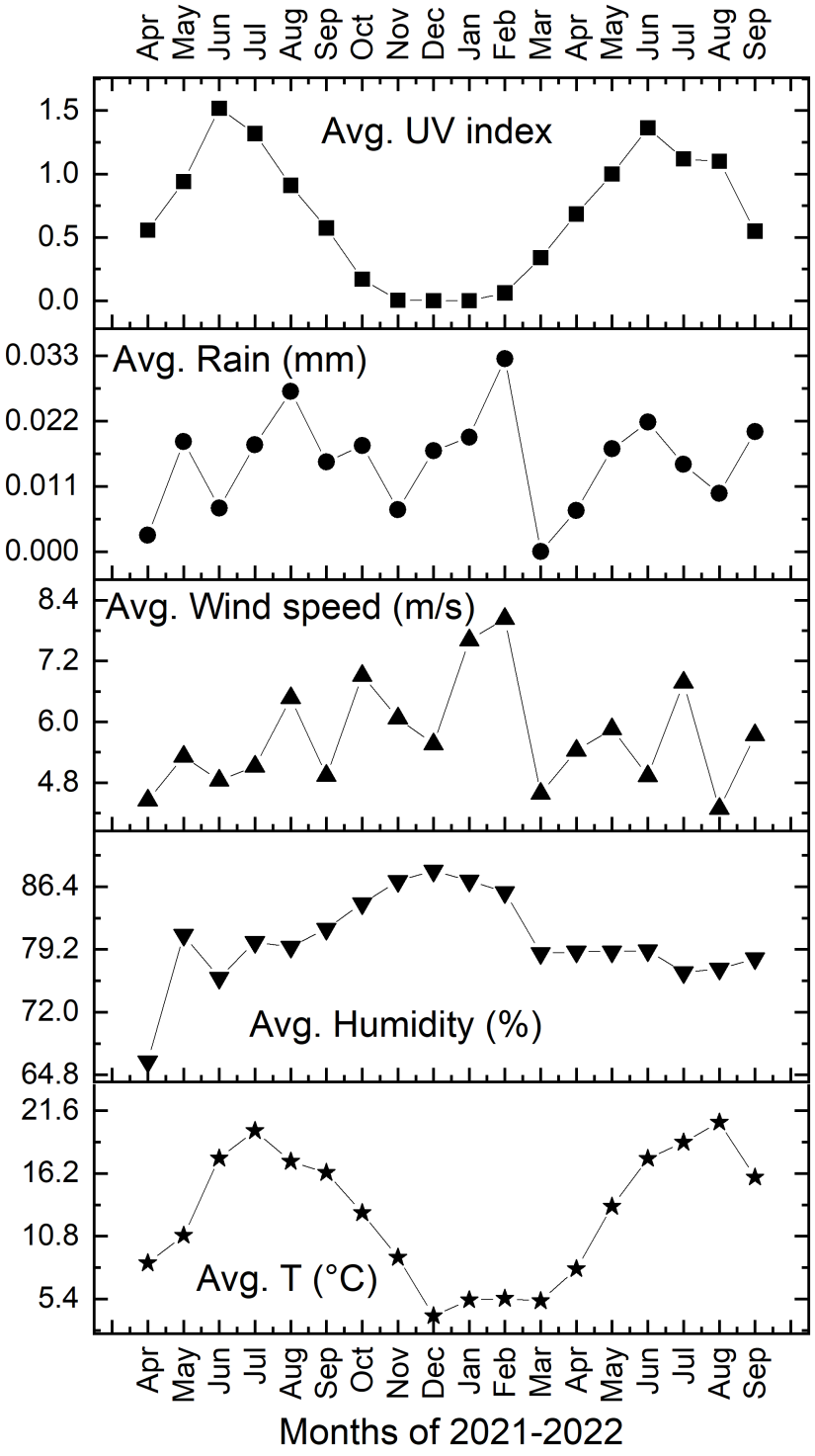

Figure 3.2.2: Weathering data of averaged UV index, Rain fall (mm), wind speed (m/s), humidity (%) and temperature (°C) recorded in the field (Hundested, Denmark) during 2021-2022 by CMTC weathering station.

3.3 Results and discussion

3.3.1 ZnEP degradation in salt spray

3.3.1.1 Open circuit potential

The OCP profile of zinc-rich epoxy sample S2 with a NDFT of 50 µm exposed to the salt spray is presented in Figure 3.3.1a, with its replications given in Figure A.1.1a. The OCP evolution shows that the zinc-rich primer undergoes three phases of activation and degradation. Phase I describes the activation of sacrificial protection by zinc through the penetration of water, oxygen, and ions from the environment, causing a decrease in OCP from -0.9 to -1.0 V/SCE. Phase II indicates that zinc corrosion dominance results in sacrificial protection as the OCP stabilises below the threshold of -0.78 V/SCE [60, 61]. Herein, zinc acts as an anode and corrodes while iron in the steel substrate acts as a cathode, as explained by the standard corrosion potential of iron being higher than zinc.

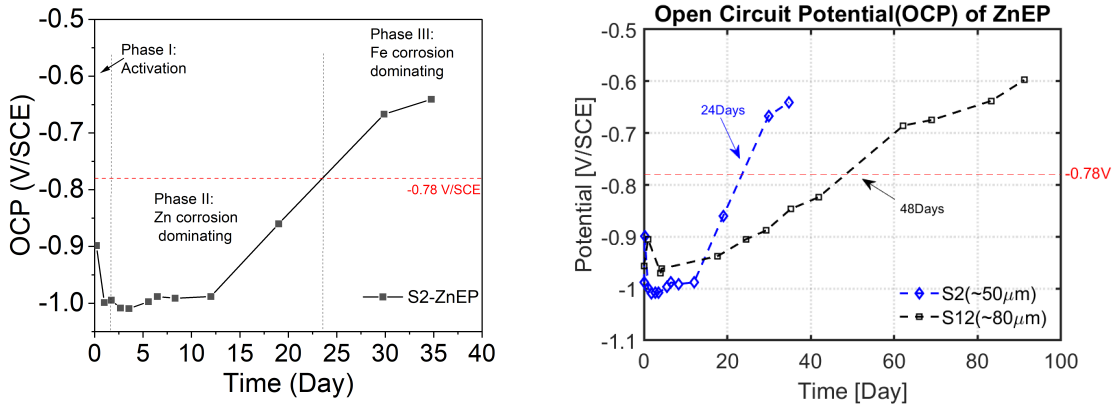

(a) ZnEP with NDTF=50 µm

(b) ZnEP 50 µm vs. 80 µm

Figure 3.3.1: The evolution of OCP was monitored for (a) the ZnEP coating system (50 µm), and (b) a comparison of the OCP evolution of different zinc-rich primers with varying DFT, exposed to the salt spray chamber.

Phase III is characterised by the OCP crossing the threshold of -0.78 V/SCE, indicating the fading of sacrificial protection. The increase in OCP is attributed to the consumption of active zinc to form zinc oxides, which reduces the overall conductivity of the zinc-rich primer. In this phase, cathodic protection from zinc becomes ineffective, and the primary corrosion process gradually shifts to iron.

Effect of increased DFT to 80 µm

The OCP profile of zinc-rich epoxy primer with NDFTs 50 µm (S2) and 80 µm (S12) exposed to salt spray is compared in Figure 3.3.1b. It is observed that the zinc-rich primer with an increased DFT of 80 µm also undergoes three phases of degradation, although the duration of each stage is extended due to the higher DFT. Replication of S12 sample is given in Figure A.1.1b. As shown in Figure 3.3.1b, the sacrificial protection of the zinc-rich primer increased from 24 days to 48 days with an increase of DFT around 50 to 80 µm.

3.3.1.2 EIS impedance data

The impedance modulus (|Z|) of zinc-rich epoxy system with a DFT of 50 µm exposed to salt spray is shown in Figure 3.3.2a, read at the lowest frequency point. The initial |Z| magnitude of 10^5 indicates a poor barrier protection property, which is reasonable as the activation of sacrificial protection of zinc requires a certain level of permeability of corrosive species from the environment. After 3.5 days (85 hours) of exposure time, the |Z| of zinc primer decreases to a magnitude of 10^3 due to the penetration of water, oxygen, and ions, consistent with Phase I-activation observed from the measured OCP in Figure 3.3.1a. Starting from 3.5 days of exposure time, the |Z| of the zinc-rich epoxy system increases up to a magnitude of 10^4 until 29.9 days (717 hours), indicating the formation of dense zinc oxides during sacrificial protection (Phase II in Figure 3.3.1a). However, between 30-35 days (717-834 hours), no significant increase in |Z| is observed due to the phasing out of sacrificial protection, as evidenced by the OCP value increasing above the threshold of -0.78 V/SCE, indicating major iron corrosion occurring after this point.

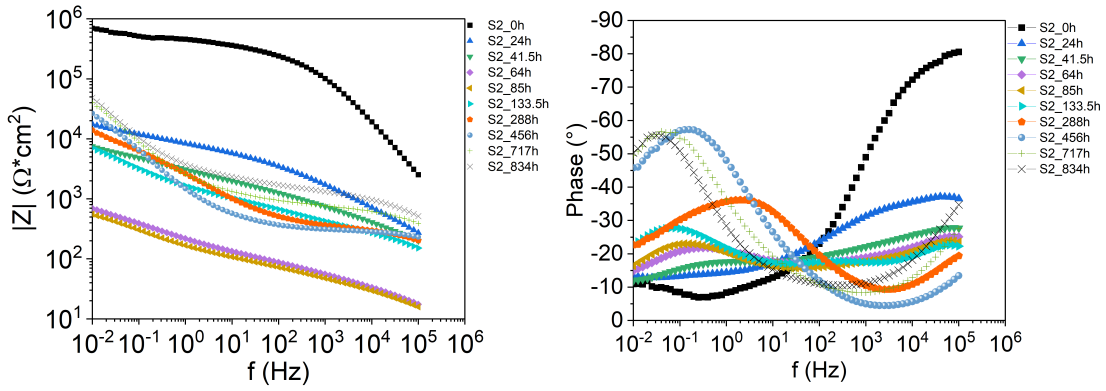

(a) Bode plot of ZnEP 50 µm

(b) Phase shift of ZnEP 50 µm

Figure 3.3.2: EIS data of zinc-rich epoxy primer (S2) exposed to salt spray with (a) Bode plot and (b) Phase shift.

The phase diagram depicting the evolution of the zinc-rich epoxy primer is presented in Figure 3.3.2b. At time 0 hours, the phase shift is close to 0 ° in the low frequency range, indicating a resistive behaviour with relatively low conductivity and a high impedance modulus. Conversely, at high frequency range of $10^3 - 10^5$ Hz, the phase shift is close to -90 °, reflecting the capacitive part of the material dominating, indicating the zinc-rich primer's ability to store electrical charge. As the exposure time in the salt spray increases, the resistive part of the zinc-rich primer (low frequency range) exhibits more capacitive behaviour, implying that the material becomes more conductive or less resistant to electrical current flow due to the penetration of corrosive species into coating/metal interface. Conversely, the capacitive part of the zinc-rich primer (high frequency range) exhibits more resistive behaviour, indicating that the primer becomes less conductive or more resistant to th electrical current due to the formation of insulating zinc oxides with increased exposure time in the salt spray. Overall, changes in the phase shift diagram are consistent with the behaviours observed in the |Z| and OCP of the system, as depicted in Figures 3.3.1a and 3.3.2a, respectively.

Effect of increased DFT to 80 µm

An increase of zinc-rich primer to 80 µm, the initial impedance modulus increased to 10^7 by a factor of 10^2 through the whole coating's lifetime (Figures 3.3.2a and 3.3.3a), indicating higher barrier protection, as expected from a thicker coating layer. However, the degradation pattern of the zinc-rich primer is the same, with an initial decrease in |Z| during Phase I activation, followed by a gradual increase in |Z| modulus through the formation of zinc oxides under sacrificial protection. The |Z| remains at the same magnitude of 104 at the end of the exposure period, at this point the iron corrosion dominates as indicated by OCP > -0.78 V/SCE in Figure 3.3.1 because rust is more porous than zinc oxides.

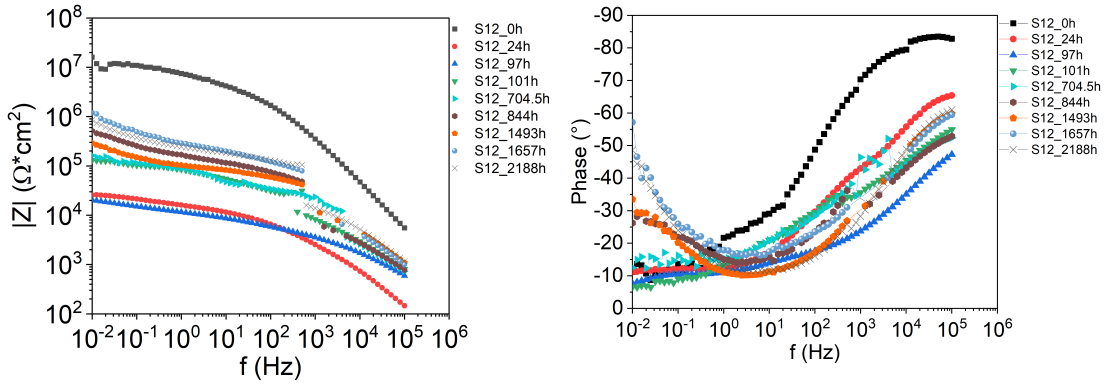

(a) Bode plot of ZnEP 80 µm

(b) Phase shift of ZnEP 80 µm

Figure 3.3.3: EIS data of zinc-rich epoxy primer exposed to salt spray with (a) Bode plot and (b) Phase shift.

The phase shift diagram in Figure 3.3.3b also exhibits the resistive property at the low frequencies and gradually changes to a more capacitive behaviour as aggressive species penetrate. The initial capacitive behaviour at the high frequencies becomes more resistive during exposure due to the formation of zinc oxides. Despite differences in protection duration and initial impedance modulus due to increased DFT, the degradation mechanisms of zinc-rich primer with DFTs of 50-80 µm follow the same pattern.

3.3.2 ZnEP degradation in the field

The same zinc-rich primer-coated steel panels with DFTs of 50 µm and 80 µm were exposed to the field and evaluated by EIS, with a frequency of measurement every month.

3.3.2.1 Open circuit potential

The OCP profile of zinc-rich primer with DFTs of 50 µm (S5) and 80 µm (S15) exposed to the field are shown in Figure 3.3.4, with their replications presented in Figure A.1.2. As shown in Figure 3.3.4, the higher DFT of 80 µm provides longer sacrificial protection compared to 50 µm. After 450 days of exposure in the field, the OCP of S15 remains below the threshold of -0.78 V/SCE, indicating that the sacrificial protection is still significant. In contrast, the OCP value of S5 crossed the threshold after 292 days of exposure, suggesting that sacrificial protection is fading out.

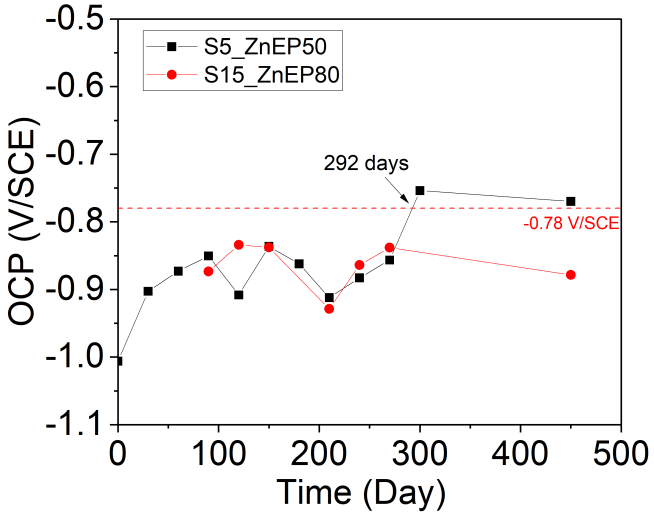

Figure 3.3.4: The evolution of OCP was monitored for ZnEP coating system with DFTs of 50 µm and 80 µm exposed to the field.

3.3.2.2 EIS impedance data

The EIS raw data of zinc-rich primer with DFTs of 50 µm and 80 µm are presented in Figure 3.3.5. As observed, there is a decrease of |Z| for ZnEP 50 µm from the initial measurement of 10^4 to 10^2 after 30 days (1 month) of exposure, indicating the Phase I-activation with penetration of aggressive species from the environments. As the exposure time increases, the impedance modulus of the coating system also increases by a factor of 10^2, indicating the progression of sacrificial protection and the transition to Phase II. Between 300-450 days (10-15 months) of exposure time, the |Z| does not change significantly, suggesting that limited active zinc is left for sacrificial protection. This is confirmed by the measured OCP value after 300 days (15 months) of exposure time reached above -0.78 V/SCE as shown in Figure 3.3.4. This means that at continuous exposure, the corrosion of iron would be the major proceeding process reaching Phase III.

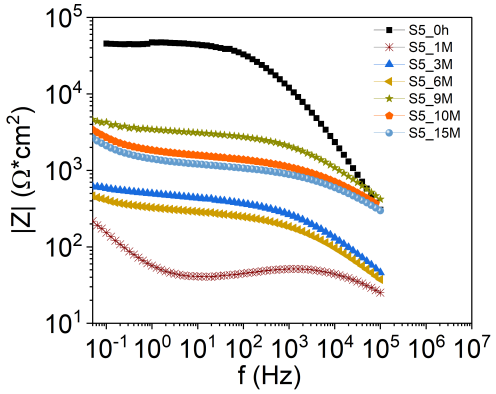

(a) Bode plot of ZnEP 50 µm

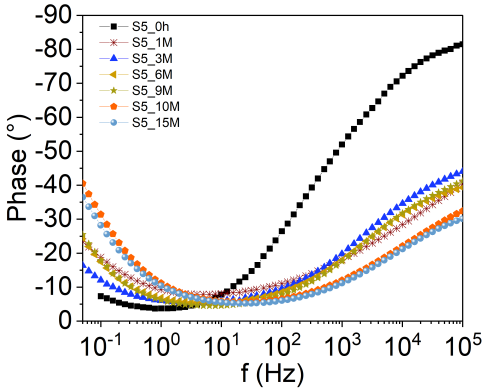

(b) Phase shift of ZnEP 50 µm

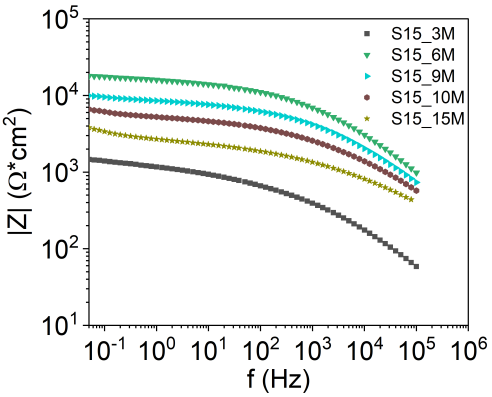

(c) Bode plot of ZnEP 80 µm

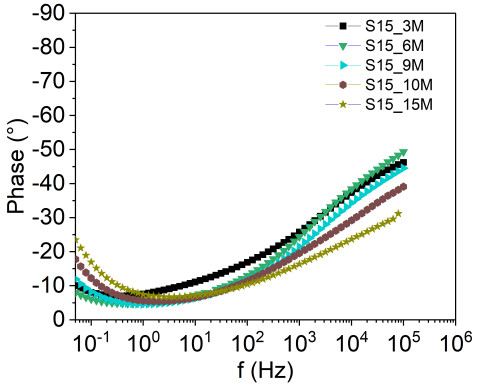

(d) Phase shift of ZnEP 80 µm

Figure 3.3.5: EIS data of zinc-rich epoxy primer exposed to the field with (a) Bode plot of ZnEP 50 µm, (b) Phase shift of ZnEP 50 µm, (c) Bode plot of ZnEP 80 µm, and (d) Phase shift of ZnEP 80 µm.

The phase shift diagram in Figure 3.3.5b, indicates that the initial resistive behaviour at the low frequency range gradually becomes more capacitive with an increase of exposure time due to penetration of the aggressive species. Additionally, the initial capacitive property

at the high frequency range becomes more resistive as gradual formation of zinc oxides occurs in the coating layer.

The EIS data of ZnEP with a DFT of 80 µm exposed to the field are presented in Figures 3.3.5c and 3.3.5d. Unfortunately, valid EIS data was only obtained after 3 months of exposure in the field due to previous instability measurements of the sample system. However, it was observed that after 3 months of exposure time sample S15 continues to provide sacrificial protection until the end of the exposure time since no clear stabilisation of |Z| is seen in Figure 3.3.5c. This is confirmed by the measured OCP profile given in Figure 3.3.4, where the OCP of S15 remains below -0.78 V/SCE after 15 months of exposure. The phase shift diagram in Figure 3.3.5d also supports the previously observed behaviour with an more negative phase shift at the low frequency range and a more positive phase shift behaviour at the high frequency compared to the initial unexposed coating. These are due to the formation of zinc oxides through consumption of active zinc particles.

3.3.3 ZnEP degradation in the neutral salt spray and the field

The degradation of zinc-rich primer was evaluated by applying OCP and EIS in both neutral salt spray and field environments. In the salt spray test, ZnEP with a DFT of 50 µm exhibited significant corrosion of iron after 24 days of exposure, while ZnEP with a DFT of 80 µm provided longer sacrificial protection duration, with significant corrosion of iron initiating after 48 days of exposure time. In the field test, ZnEP with a DFT of 50 µm showed significant iron corrosion proceeding after 292 days exposure in the field, while for ZnEP with a DFT of 80 µm, the sacrificial protection remained active after 450 days of exposure. Table 3.3.1 summarises the significant protection duration of zinc-rich primer exposed to the neutral salt spray and the field, respectively. Based on the sacrificial protection time given in Table 3.3.1, the accelerated factor of zinc-rich primer with a DFT of 50 µm in the salt spray test is determined to be 12 times faster compared to the field exposure. The sample S15 may lose its sacrificial protection in the field exposure after at least 576 days of exposure based on the accelerated factor of 12.

Table 3.3.1: Zinc rich epoxy primer protection duration in the neutral salt spray and the field.

Sample No.	Average DFT	Environment	Sacrificial protection duration t	Accelerated factor $\frac{t_{field}}{t_{saltspray}}$
S2	52 µm($\pm$3)	Salt spray	24 days	$\frac{292}{24}$= 12
S12	84 µm($\pm$6)	Salt spray	48 days	$\frac{>450}{48}$= > 9
S5	54 µm($\pm$6)	The field	292 days	
S15	91 µm($\pm$4)	The field	> 500 days	

Zinc-rich primer degradation in both the salt spray and the field was found to involve the same degradation mechanisms based on electrochemical measurements. The gradual consumption of active zinc particles in the coating film was tracked through the measured OCP profiles while changes in the barrier properties of the primer were expressed through impedance modulus |Z| from EIS measurements. At low frequencies, the phase shift diagram exhibited a more capacitive behaviour with increased exposure time due to the

penetration of aggressive species and activation of sacrificial protection at the coating/steel interface. In contrast, a more resistive behaviour developed at the high frequencies caused by the formation of zinc oxides in the coating layer.

In summary, the degradation of zinc-rich primer exposed to the salt spray and the field proceeds through the following stages: Phase I involves penetration of aggressive species from the environment and activation of sacrificial protection, and Phase II involves sufficient sacrificial protection period. However, with continuous exposure where the OCP is above the threshold of -0.76 V/SCE reaches Phase III, major iron corrosion in the steel occurs as the essential sacrificial protection of the zinc-rich primer fades out, leaving only slight barrier protection from the primer over the substrate.

3.3.4 Epoxy primer degradation

One-layer epoxy primer (EP-01) with nominal dry film thicknesses (DFTs) of 50 µm and 80 µm were exposed to neutral salt spray and the field, respectively. The coated samples were evaluated using EIS at different exposure times to monitor the degradation over time.

3.3.4.1 Neutral salt spray exposure

The epoxy primer coated steel samples, with nominal DFTs of 50-80 µm, were evaluated for degradation when exposed to neutral salt spray using EIS technique. The corresponding data are presented in Figure 3.3.6, and the replications are shown in Appendices A.2.1 and A.2.2. The bode plots in Figures 3.3.6a and 3.3.6c reveal that the coating barrier properties of the epoxy primer decrease with increasing exposure time for both DFTs. Initially, the epoxy primer with a DFT of 50 µm exhibits an impedance modulus ($|Z|_0$) in the order of 10^9, whereas an increase in DFT to 80 µm results in an increased $|Z|_0$ value of 10^{10}. The discontinuities and jumps observed in the phase shift plots in Figures 3.3.6b and 3.3.6d at 0-hour measurement are believed to be caused by the wire connected to the steel substrate which has been observed to affect the high frequency ranges.

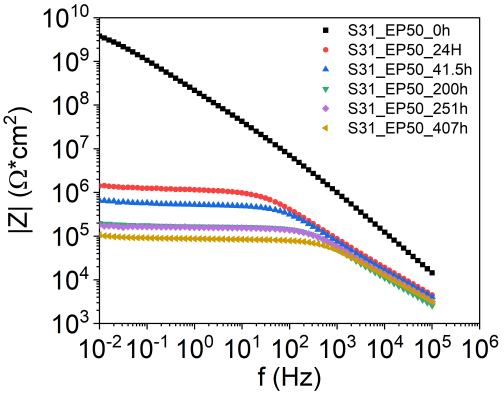

(a) Bode plot of EP50 µm

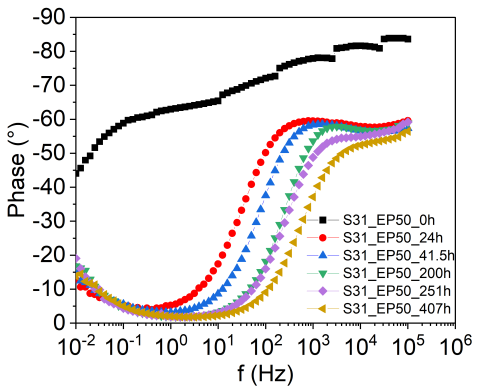

(b) Phase shift of EP50 µm

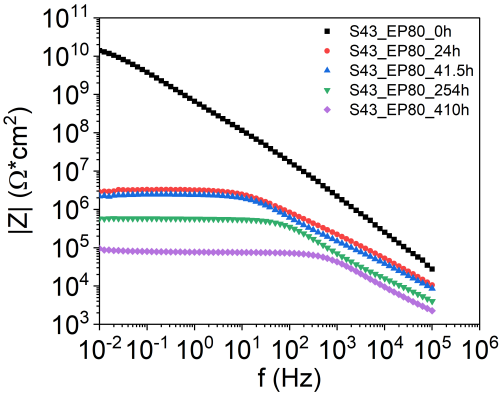

(c) Bode plot of EP80 µm

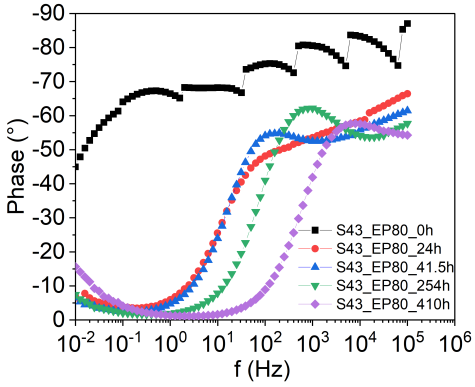

(d) Phase shift of EP80 µm

Figure 3.3.6: EIS data of epoxy primer exposed to neutral salt spray with (a) Bode plot of EP-01 50 µm, (b) Phase shift of EP-01 50 µm, (c) Bode plot of EP-01 80 µm, and (d) Phase shift of EP-01 80 µm. The discontinuities and jumps of the phase shift plot at 0 hour of exposure time is caused by the wire connected to the steel sample (insufficient sample design).

When comparing the barrier protection properties provided by the epoxy primers, it is evident that sample S31 EP50 exhibits non-sufficient barrier protection after 41.5 hours of exposure in neutral salt spray, as indicated by $|Z|<10^6\ \Omega \cdot cm^2$. On the other hand, sample S43 EP80 demonstrates sufficient barrier protection for up to 254 hours of exposure to neutral salt spray. This highlights the fact that increasing the epoxy barrier primer thickness from 50 to 80 µm extends the barrier properties of the coating. The phase shift diagrams shown in Figures 3.3.6b and 3.3.6d further support these findings. Initially, the coatings exhibit a phase shift close to -90 °C, indicating highly capacitive behaviour and suggesting that the initial coating acts as an insulator, preventing the passage of current. However, as the epoxy primer is exposed to the salt spray and undergoes degradation or deterioration, the phase shift increases towards more positive values, which can be attributed to various factors, such as moisture and ion ingress into the coating and/or corrosion of the underlying steel substrate.

3.3.4.2 Epoxy primer exposure in the field

The epoxy barrier coatings with NDTFs of 50-80 µm were exposed to the field and evaluated with EIS measurements with results presented in Figure 3.3.7. Unfortunately, stable impedance measurements were only achieved after 3 months of exposure time.

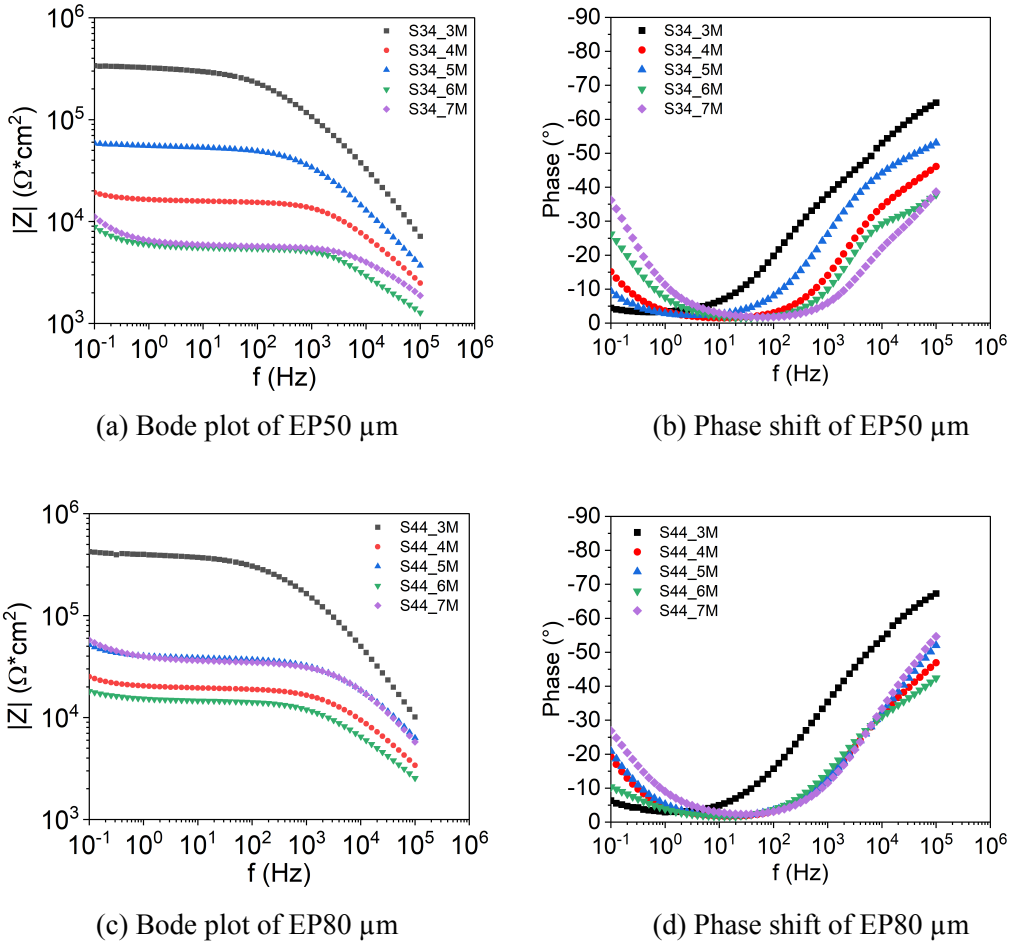

(a) Bode plot of EP50 µm

(b) Phase shift of EP50 µm

(c) Bode plot of EP80 µm

(d) Phase shift of EP80 µm

Figure 3.3.7: EIS data of epoxy primer exposed to neutral salt spray with (a) Bode plot of EP-01 50 µm, (b) Phase shift of EP-01 50 µm, (c) Bode plot of EP-01 80 µm, and (d) Phase shift of EP-01 80 µm. Replications are presented in Appendices A.3.1 and A.3.2.

From bode plots in Figures 3.3.7a and 3.3.7c, it can be seen that after 3 months of exposure in the field, the epoxy coatings have lost all their barrier properties for both DFTs between 50-80 µm. The measured impedance modulus of 10^5 is smaller than the threshold of sufficient barrier protection, which is 10^6. This observation is further supported by the optical images taken during the exposure period, as shown in Figure 3.3.8, where significant pitting corrosion spots were observed on both coating surfaces after 3 months of exposure. However, Figures 3.3.8d and 3.3.8h reveal that sample S44 (80 µm) has fewer pitting corrosion spots on its surface compared to sample S34 (50 µm). This indicates that the increased DFT provides slightly better protection. Interestingly, this slightly improved protection is not evident from the impedance modulus values from EIS measurements, as shown in Figure 3.3.7. Therefore, the optical images are presented to complement the

impedance data and provide a comprehensive assessment of coating deterioration.

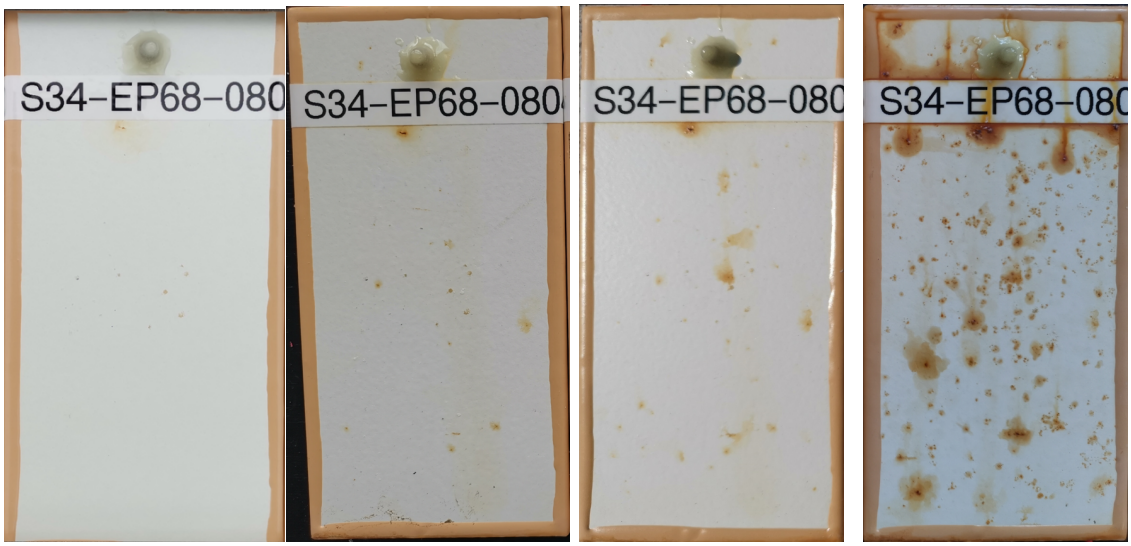

(a) S34 0h (b) S34 1 month (c) S34 2 months (d) S34 3 months

(e) S44 0h (f) S44 1 month (g) S44 2 months (h) S44 3 months

Figure 3.3.8: Optical images of S34 (50 µm) and S44 (80 µm) after 0, 1, 2, 3 months exposure in the field. Replications are presented in Appendix A.3.3.

In summary, the epoxy coating barrier coating system exposed to neutral salt spray and the field evaluated by the EIS followed the same pattern with decreasing impedance modulus as increasing exposure time. Once barrier property is lower than the threshold magnitude of $10^6\ \Omega \cdot cm^2$, no sufficient barrier protection is provided by the epoxy barrier coating for further exposures.

3.3.5 Conclusion

Electrochemical impedance measurements are valuable for studying the degradation process of commercial coatings exposed to different environments in a non-destructive manner. In the case of zinc-rich epoxy primers, the duration of sacrificial protection can be monitored by analyzing the evolution profile of the Open Circuit Potential (OCP). Additionally, information about the barrier properties and performance of the sample at specific exposure times can be obtained through the impedance modulus (|Z|) in EIS measurements. However, it is important to note that the primary protective mechanism of zinc-rich primers is sacrificial protection rather than barrier properties. Therefore, the impedance modulus threshold of $10^6\ \Omega \cdot cm^2$ cannot be used as the significant factor to evaluate the effectiveness of corrosion protection provided by zinc-rich primers.

When exposed to neutral salt spray and field conditions, the zinc-rich epoxy primer undergoes a degradation process characterised by similar mechanisms. The OCP gradually increases from around -0.9 V/SCE, indicating sufficient sacrificial protection. However, once the OCP value surpasses -0.76 V/SCE, the sacrificial protection becomes inadequate. Simultaneously, the impedance modulus of the zinc-rich primer exhibits an increase of approximately 1 to 2 orders of magnitude on a logarithmic scale. This increase can be attributed to the formation of zinc oxides, which enhance the barrier properties of the exposed zinc-rich primer system.

In contrast, epoxy barrier coatings primarily provide anti-corrosive properties through barrier protection, preventing the penetration of aggressive species from the environment to reach the coating/steel interface. In this case, the impedance modulus is a suitable parameter to describe sufficient coating performance. Once the measured |Z| falls below $10^6\ \Omega \cdot cm^2$, corrosion of the substrate is expected to occur with continuous exposure.

Based on the evolution of OCP, the neutral salt spray test is found to accelerate the degradation of zinc-rich primer by 12 times compared to the field exposure. This can be attributed to the harsh testing environment, characterised by a constant temperature of 35 °C, which enhanced the diffusivity of aggressive species such as water, oxygen and ions into the coating. Consequently, this promotes the degradation process of the coating.

In summary, the degradation of the zinc-rich epoxy primer can be monitored in both neutral salt spray and field conditions by evaluating its performance through actual measured OCP values and impedance modulus. However, the studied epoxy primer (EP-01) exhibited poor performance under both exposure conditions. In the neutral salt spray, the barrier properties of EP-01 coatings with DFTs between 50-80 µm were already compromised after just 24 hours, as indicated by the impedance modulus evaluation. Similarly, in the field study, the first evaluation of the impedance modulus for the EP-01 coating system occurred after three months of exposure, and it was found that insufficient barrier properties remained. Therefore, a less aggressive exposure condition is desired to further investigate the deterioration of the EP-01 coating system, which will be explored in the next chapter by studying water uptake in EP-01 coatings immersed in a 3.5 wt% NaCl solution at room conditions non-destructively.

4 Non-destructive evaluations of water uptake in epoxy coating

Highlights

1. *Four different methods for water uptake in epoxy coating have been compared.*
2. *SAM can monitor the swelling of the coating caused by water uptake non-destructively.*
3. *Leaching and swelling processes are detected during water uptake.*

Abstract

A commercial epoxy coating was applied on steel panels and in the form of free films. Both steel panels and free film samples were immersed in 3.5 wt.% NaCl solution to investigate the water uptake process through the coating films using non-destructive evaluation techniques (Gravimetric analysis, Electrochemical Impedance Spectroscopy (EIS), Attenuated Total Reflection-Fourier Transform Infrared Spectroscopy (ATR-FTIR) and Scanning Acoustic Microscopy (SAM)). The gravimetric analysis showed that the water uptake process in the epoxy free films exhibited rapid water absorption initially, followed by a slower uptake due to counteracting process between water uptake and leachable content. Towards the later stage, a decrease in mass was observed, indicating the dominance of the leaching process. The water uptake process into coated steel substrate measured by EIS proceeded through rapid water absorption within 72 hours, followed by a continuous slower water uptake rate up to 336 hours of immersion time. This continuous increase in the water content in the coating layer was attributed to the swelling process observed on the coated steel substrate, which was confirmed by SAM. Furthermore, the ATR-FTIR analysis indicated that the majority of absorbed water molecules were hydrogen bonded to the epoxy matrix. By combining the results from the applied non-destructive techniques, the water uptake mechanisms into the epoxy coating film were proposed.

Keywords: *Water uptake processes, Epoxy coating, Gravimetric analysis, EIS, SAM.*

4.1 Introduction

Organic epoxy coatings are extensively applied for corrosion protection of metallic substrates in harsh marine and offshore environments due to their high crosslink density and relatively high resistivity for aggressive chemical species [5, 6, 62]. However, this resistivity behaviour will not remain constant and will weaken over time when exposed to the environment. One of the earliest deterioration processes for organic coatings in humid environments is the diffusion and absorption of water [63, 64, 65]. The diffusion of water into the organic coating can lead to blistering, loss of coating adhesion, and, in combination with an aerobic environment, initiate the corrosion process of a metallic substrate [25, 26, 27, 66, 29, 30]. Therefore, understanding of water uptake process is crucial for optimising coating performance, ensuring their durability and minimising their environmental impacts.

In recent decades, various experimental designs and techniques have been utilised to study the water uptake process in organic coating films or polymer resins. These include gravimetric analyses [20, 67, 68, 69, 70], High-resolution NMR-imaging [71, 72], Fourier Transform Infrared Reflection spectroscopy (FTIR) [47, 73, 74], and especially Electrochemical Impedance Spectroscopy (EIS) [30, 67, 68, 75, 76, 77]. While EIS measurements have been widely used for water uptake estimation, challenges remain in accurately interpreting EIS data to determine the level of water uptake. This study aims to apply diverse non-destructive evaluation techniques to evaluate the water uptake process using different measurement parameters. Both free films and coated steel samples would be investigated, and the accuracy of each technique in describing the water uptake process in the organic coating will be discussed.

Anticorrosive coatings provide substrate protection through barrier, inhibitive, and/or cathodic protection mechanisms. These technologies utilise different active pigments in the formulation, leading to diverse protection and degradation mechanisms [20]. Consequently, the interpretation of the EIS measurements and the selection of an appropriate equivalent circuit model (ECM) for fitting EIS data depend on the specific coating system being studied. The common approach for estimating water uptake from EIS data is to determine the coating capacitance as a function of exposure time and then use Brasher-Kingsbury equation [78] to calculate the water content inside the coating. However, the accuracy of the water uptake estimation using the Brasher-Kingsbury equation has been questioned, and some studies [67, 68] have reported an overestimation of water uptake from EIS results compared to gravimetric data. It has also been reported to consider the coating swelling process during water uptake estimation from EIS data in order to obtain more consistent results for the gravimetric evaluation of water uptake [68, 70, 71]. Another challenge is that there are several approaches in the literature to determine the coating capacitance from constant phase parameters based on applied ECM models, and there is limited discussion about how these approaches affect the accuracy of the water uptake determination. Furthermore, the role of the swelling process in water uptake within the organic coating film requires further investigation.

In this study, primarily non-destructive evaluation techniques such as EIS, ATR-FTIR, gravimetric analysis, and Scanning Acoustic Spectroscopy (SAM) are applied to a coated commercial epoxy primer to monitor the water uptake process when immersed in 3.5 wt% NaCl solution at 25 °C. Non-destructive evaluation enables continuous monitoring of wa-

ter diffusion in the coating film, allowing for a continuous evaluation of water uptake as a function of exposure time, without destroying the sample. This approach is cost-effective as it reduces sample material consumption and saves time. Additionally, continuous monitoring of the water diffusion process in epoxy coating films allows for a kinetic study of this phenomenon. The results of each technique are compared, and the advantages and limitations of the evaluation tools are discussed. The combination of these non-destructive techniques could contribute to a comprehensive understanding of the water uptake process in the epoxy coating film, including the different deterioration mechanisms caused by water uptake.

4.2 Theoretical background

Water uptake determination using the EIS technique is based on the theory of changes in coating capacitance during exposure, primarily attributed to the uptake and transport of water into the coating film. This can be assumed because of the significant difference between the dielectric constant of water (ε_w=80 at 25°C) and organic coating material ($\varepsilon \approx$3). As water diffuses into the coating film, the dielectric constant of the film increases, leading to an increase in coating capacitance. Thus, the change in coating capacitance can be used to track water uptake in organic coatings.

4.2.1 Water uptake estimation through effective capacitance

At high frequencies, the capacitor acts as a "short circuit" since the voltage oscillates rapidly compared to the time required to polarise the coating film. As a result, the coating film is not significantly polarised, and the capacitor offers minimal resistance to the oscillating current, making the capacitance property dominant. At low frequencies, where the cycle time is longer, the coating layer may be polarised and recovered within the cycle time, but this behaviour does not contribute significantly to the overall response. Essentially, all of the current flows through the resistors of the studied system [72, 47]. Consequently, to reflect the coating capacitance change during water uptake, a fixed high frequency in the range of 10k-100k Hz is widely accepted to apply for coating capacitance determination [69, 73, 74]. An equivalent circuit model consists of a resistance R (Ωcm^2) in parallel with a capacitance C (F) that represents the coating film properties can be determined as [74, 69]:

$$C_{HF} = \frac{-Z''}{2\pi f|Z|^2} = \frac{-Z''}{2\pi f(Z'^2 + Z''^2)} \tag{4.2.1}$$

where C_{HF} is coating capacitance determined at a fixed high frequency (HF), Z'' and Z' are the imaginary and real parts of the impedance (Ωcm^2) at the fixed frequency f. $|Z|$ is impedance modulus.

In real cases, the studied sample would rarely act as a pure capacitor. Instead, it often exhibits non-ideal capacitance behaviour, which is represented by a constant phase element (CPE). This irregular capacitance behaviour can be caused by factors such as surface inhomogeneity and electrode porosity [76]. The physical interpretation of constant phase elements is still debatable, as well as the approaches used to determine capacitance values from constant phase elements.

Brug et al. [77] proposed the following equation for the double-layer capacitance determination of a blocking system where a constant phase element is applied in the equivalent

circuit model. They assumed a surface distribution of time constants and included a solution resistance (R_s) in the analysis of the CPE behaviour. They further proposed that the effective capacitance determination of an electrical double-layer should only consider the solution resistance, which is given as [79]:

$$C_{Brug} = Y^{\frac{1}{n}} \left(\frac{1}{R_s} \right)^{\frac{n-1}{n}} \tag{4.2.2}$$

Where Y ($S \cdot s^n \cdot cm^{-2}$) and n are the CPE parameters.

Hsu et al. [79, 80] proposed a method based on the observation that the capacitance of a CPE can be determined by identifying the frequency at which the imaginary part of the impedance reaches its maximum, known as the critical frequency. They proposed the following equation for determining the double-layer capacitance:

$$C_{Hsu} = \frac{(Y \cdot R_p)^{\frac{1}{n}}}{R_p} \tag{4.2.3}$$

Where R_p is the polarisation resistance in the coating film, and Y and n are CPE parameters.

In contrast to Equation (4.2.2), Equation (4.2.3) neglected the effect of solution resistance R_s and instead emphasises the significance of the polarisation resistance in the coating film for double-layer capacitance determination.

Equations (4.2.1) to (4.2.3) for coating capacitance determination have been extensively utilised in the literature [81]. Once the change in coating capacitance change over time is known, the amount of water uptake can be determined using the Brasher-Kingsbury equation [78]:

$$\varphi = \frac{\log\left(\frac{C(t)}{C(0)}\right)}{\log(\varepsilon)} \tag{4.2.4}$$

$C(t)$ and $C(0)$ represent the capacitance at time t and the capacitance of the initial unexposed coating ($t = 0$), respectively. ε_w=80 at 25 °C is the dielectric constant of water, and φ is the volume fraction of water inside the coating. Brasher-Kingsbury equation is proposed based on several assumptions to describe the coating film. These assumptions include the film being composed of three phases: the solid phase (polymer and non-soluble additives), the water and the air. It is assumed that each layer has a parallel distribution of these three phases to the coating surface, with components that are insoluble among them. The swelling process of the coating film is neglected, and a random water distribution is assumed inside the coating film.

4.2.2 Water estimation using a linear rule of mixture

The permittivity (ε') of the film can be expressed as a function of the capacitance, based on the geometry of the film, and is given by the following equation [74]:

$$\varepsilon'(C) = \frac{l}{\varepsilon_0 A} C \tag{4.2.5}$$

where l is coating thickness, $\varepsilon_0 = 8.854 \cdot 10^{-12} \frac{\mathrm{F}}{\mathrm{m}}$ is the vacuum permittivity, A is the area exposed to the electrolyte, and C is capacitance of the coating film.

Bonin et al. [82] presented another approach to determine water uptake by utilising the fixed high frequency calculated capacitance from the impedance data and determining the coating permittivity $\varepsilon'(f)$ given in Equation (4.2.6). This is achieved by substituting Equation (4.2.1) into Equation (4.2.5), resulting in the following expression:

$$\varepsilon'(f) = \frac{-Z''}{2\pi f C_v |Z|^2} \quad , \quad C_v = \frac{\varepsilon_0 A}{l} \tag{4.2.6}$$

Where Z'' is the imaginary part of the impedance and $|Z|$ is the impedance modulus given at frequency f, respectively. The permittivity at the frequency of 100 kHz was used, assuming that the high frequency represents the properties of the coating film.

From the change in coating permittivity, the water uptake in the coating film is determined by applying a linear rule of mixture that considers the composition of the coating (including polymer matrix, fillers and additives) and the absorbed water [82, 83, 84]:

$$\phi(t) = \frac{\varepsilon'(t) - \varepsilon'(0)}{\varepsilon_{water} - \varepsilon'(0)} \tag{4.2.7}$$

$\phi(t)$ is the volume fraction of water inside the coating film, $\varepsilon'(t)$ is the coating permittivity determined by EIS at time t, $\varepsilon'(0)$ is the initial coating permittivity, and ε_{water}=80 is the water permittivity at 25 °C.

4.3 Experimental Methodologies

4.3.1 Preparation of coated sample

A commercial epoxy paint (EP-01) consisting of epoxy resin bisphenol A cured with aromatic amine adduct, was airless sprayed onto a cleaned and sandblasted (Sa 2½, ISO8501) S235JR steel surface (150 mm x 75 mm x 3 mm). The coating samples were left for curing under a fume hood for at least 7 days and stored in sealed plastic bags to minimise exposure to the environment before testing. The cured coated steel samples were labelled as S47 (DFT=106 ± 6 µm), S48 (DFT=109 ± 6 µm) and S49 (DFT=108 ± 5 µm), respectively, with their dry film thickness measured using an Elcometer gauge. Samples S48 and S49 were used to check the reproducibility of S47 and prepared from the same batch of EP-01 coating.

4.3.1.1 Free film preparation

The free films were produced by applying the EP-01 coating onto acrylic panels with a 150 µm gap applicator, and the final dry film thickness was measured with an Elcometer gauge to 100 ± 5 µm. After 24 hours of curing, the EP-01 coating film was carefully removed from the acrylic substrate and kept for additional 6 days in the fume hood for curing. The fully cured free films were then cut into sizes of 4 cm x 5 cm and 6 cm x 6 cm and stored in a desiccator before immersion in a 3.5 wt.% NaCl for water uptake study using gravimetric analysis, EIS and FTIR techniques, respectively.

4.3.2 Electrochemical Impedance Spectroscopy (EIS) measurements

EIS measurements were performed using a potentiostat from Gamry Reference 600+, covering a frequency range of 10 mHz to 100 kHz. The measurements were taken at an acquisition rate of 10 points per decade and a sinusoidal voltage amplitude of 10 mV at the open

circuit potential. To minimise external interference signals, all EIS measurements were carried out with the cell placed inside a Faraday box. EIS measurements were performed at a stabilised open circuit potential to ensure the equivalent stability of the system.

4.3.2.1 Three-electrode test cell configuration on coated steel samples

A three-electrode configuration was utilised to study the EP-01 coated steel substrates, where the coated panel served as a working electrode (WE), a graphite rod was used as a counter electrode (CE), and a Saturated Calomel Electrode (SCE) served as a reference electrode (RE). The exposure area of the coated steel sample is limited to 10 cm^2 by a cell thicker mask attached to the sample surface. A glass cylinder cell, sealed with a rubber ring underneath, was used to hold the electrolyte, which consisted of a 3.5 wt.% NaCl solution.

4.3.2.2 Four-electrode test cell configuration of free film

The EIS evaluation of free films aims to overcome the potential effect of water accumulation between the coating layer and the steel substrate. For this purpose, a four-electrode configuration was utilised to monitor the water uptake through the free films using EIS measurements. The setup consists of two half-cells with an opening channel diameter of 5 cm^2, connected with a free film sandwiched in between, dividing the channel into two identical zones as illustrated in Figure 4.3.1a. In each zone, a graphite rod and a SCE electrode were placed to measure the potential inside the electrolyte, specifically the voltage drop across the free film within the electrolyte. The four-electrode configuration (shown in Figure 4.3.1b) involved two SCE electrodes, one connected to the working sense lead and the other to the reference lead. One of the graphite rods served as the working electrode and the other acted as the counter electrode. The electrolyte used is a 3.5 wt.% NaCl solution.

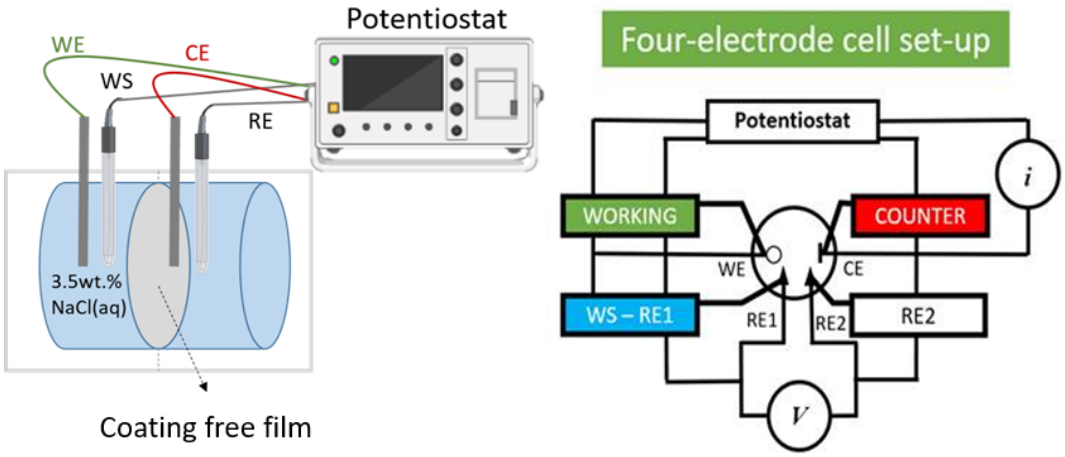

(a) EIS setup for a free film (b) Four-electrode setup in Gamry

Figure 4.3.1: Four-electrode configuration for EIS measurements of a free film involves using graphite rods as Working Electrode (WE) and Counter Electrode (CE), respectively. Two SCE electrodes are connected to Working Sence (WS) and Reference Electrode (RE), respectively. Schematic illustration of the cell setup is provided in (a), while the electrical circuit diagram for the four-electrode cell connection to Gamry potentiostat is given in (b), adapted from Gamry. Photos of the implemented cell are presented given in Appendix B.3.

4.3.3 Gravimetric measurements of free films

Three EP-01 free films, each measuring 4 cm x 5 cm, were immersed in a 3.5 wt.% NaCl solution. The water uptake on the free films was measured using a Sartorius balance with a precision of 0.1 mg. Before each measurement, the free films were quickly wiped with tissue paper until no water droplets were visible on the film surface. The mass of the water absorbed by the free films was calculated using the following equation:

$$X_m(t) = \frac{m_t - m_0}{m_0} = \frac{m_{water}}{m_{coating}} = \frac{V_{water} \cdot \rho_{water}}{V_{coating} \cdot \rho_{coating}} = X_v(t)\frac{\rho_{water}}{\rho_{coating}} \tag{4.3.1}$$

where $X_m(t)$ is the mass fraction of water uptake at time t and $X_v(t)$ is the volume fraction of water uptake at time t. m_t and m_0 are the mass of the free film at time t and time 0, respectively. The density of the EP-01 coating, $\rho_{coating}$=2272 $\frac{kg}{m^3}$ was determined based on the free films (see Appendix B.2), and the water density is ρ_{water}=997 $\frac{kg}{m^3}$.

4.3.4 Attenuated Total Reflection-Fourier Transform Infrared Spectroscopy Testing

Attenuated Total Reflection-Fourier transform infrared spectroscopy (ATR-FTIR) was applied before and end of immersion of EP-01 coating free films in order to qualitatively identify the water uptake. This was accomplished using a Thermo Scientific Nicolet is50 ATR-FTIR spectrometer. The O-H bending peak in FTIR spectra is subsequently deconvoluted [85, 86, 87] into four specific wavelengths (3623 cm^{-1}, 3555 cm^{-1}, 3419 cm^{-1} and 3264 cm^{-1}) using Gaussian function fitting (Origin 2019b) to differentiate the possible forms of water interactions inside the epoxy coating.

4.3.5 Scanning Acoustic Microscopy Evaluation

Scanning Acoustic Microscopy (SAM) is utilised to follow the changes in coating thickness during the water uptake process on coated steel samples. The examined sample was immersed in deionised (DI) water, which served as the connecting medium between the sound wave emitted from the transducer and reflected from the coated steel sample. Each scanning time is within 5 min, which limits the exposure of the examined samples in the DI-water. Thus, it is assumed that no significant impact on the water uptake process would be made. SAM was firstly operated in C-scan mode, where the designated area of 10 cm^2 inside the cell thicker was scanned, as illustrated in Figure 4.3.2a. Subsequently, five red lines were drawn on the C-scan image (Figure 4.3.2a) to define the positions of the cross-sections to be scanned in B-scan mode. This results in the generation of five B-scan images. The B-scan image of the cross-section through the coated steel sample is illustrated in Figure 4.3.2b, where the coating thickness can be monitored in situ. Figure 4.3.2b provides an enlarged illustration of one red line in Figure 4.3.2a.

The coating thickness monitored by SAM is based on the five cross-sections (red lines) of the exposed area. For each cross-section image (B-scan images), the coating thickness has been measured in five different positions, equidistant from each other. Hence, the final coating thickness is an averaged value of 25 measurement points at the evaluated exposure time. This value is then assumed to represent the thickness of the entire exposure area. The coating layer is measured from the intensive reflective acoustic impedance between water and coating until the first significant acoustic impedance reflection occurs between coating and steel.

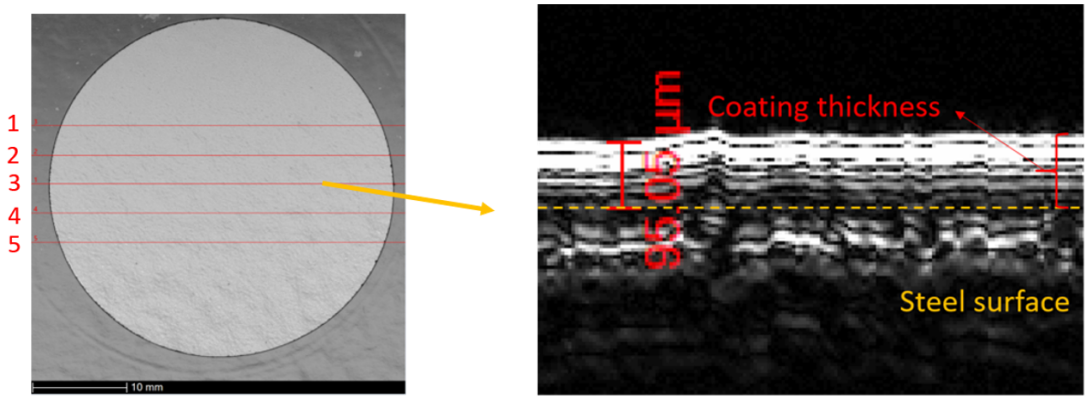

(a) C-scan image (b) B-scan image

Figure 4.3.2: (a) illustration of SAM image using C-scan mode of the exposed coated sample area, (b) SAM image using B-scan mode illustrating an enlarged part of the cross-section of the coated sample.

4.4 Results and Discussion

Four different non-destructive techniques were applied to evaluate the water uptake into the coating layer in two sample forms: free films and coated steel substrates. The gravimetric and ATR-FTIR evaluations were performed on the free film samples, while the EIS technique was used for both the free film and coated steel substrate. Scanning Acoustic Microscopy (SAM) was applied specifically to the coated steel substrate.

4.4.1 Gravimetric measurement of water uptake

The percentage of mass increase for EP-01 free films is presented in Figure 4.4.1a. Each measured point is determined as an averaged mass increase of all three free film samples, with the corresponding standard deviation shown as the grey area. The percentage of mass increase plotted as a function of $\sqrt{t}$ is represented in Appendix B.3 to assess whether the diffusion is Fickian. It still shows three phases of mass increase in the epoxy free films, indicating that this water uptake process cannot be purely described by Fickian diffusion behaviour with a linear dependence of $\sqrt{t}$.

A rapid water absorption phase, named phase P1, is observed within the first 8 hours, as shown in Figure 4.4.1. During this phase, an increase of water up to 1.4 wt.% is determined. This rapid water uptake may be attributed to the significant concentration gradient between the initial dry coating free film and the bulk solution, as illustrated in Figure 4.4.1b. The initial rapid increase shortly after exposing the samples to the electrolyte has been reported to be primarily due to the fast diffusion of water molecules [88].

The subsequent slower water uptake process observed during phase P2 (Figure 4.4.1) may be attributed to water diffusion into the coating film counteracting with the initiated leaching process from the coating film, as illustrated in Figure 4.4.1b. This counteracting effect of water uptake and leaching process resulted in a slower overall increase in mass compared to phase P1. During phase P2, the mass increase reached its highest level at around 2.4 wt.%.

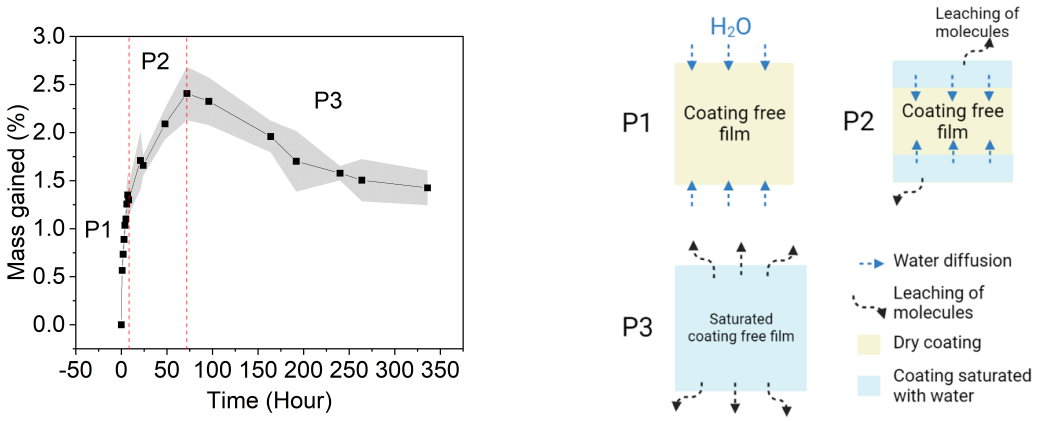

(a) Mass increased of epoxy free film

(b) Illustration of water uptake

Figure 4.4.1: (a) The averaged mass percentage evolution of water uptake into epoxy free film. The data points are based on gravimetric measurements of three epoxy free films in 3.5 wt.% NaCl solution with the standard deviation represented by the grey area. (b) The water uptake process in the free films is simplified into three phases, namely P1, P2 and P3.

During phase P3, a mass loss in the free films is observed, indicating that the films are saturated with water and a swelling process may be significant. However, the swelling and water uptake in the coating layer may be counteracted by the dominant leaching process, resulting in the total mass of the free film to decrease. This observed mass loss has also been reported as leaching of ingredients [89] in the coating formulation e.g. rheological agents and/or plasticizers [83].

It should be noted that water uptake, leaching and swelling occur simultaneously during phases P2 and P3. The total measured mass reflects the sum of all processes, with one process being more dominant than the other during each phase. Additionally, sodium and chloride ions may also diffuse into the epoxy coating along with water molecules contributing to the overall mass increase.

4.4.2 ATR-FTIR on free films for water uptake

The studied free film has been evaluated by ATR-FTIR before and after 14 days of immersion with results shown in Figure 4.4.2b. The peak area at a wavelength of 3421 cm^{-1} represents the O-H bending/stretching mode, indicating water absorption inside the film. The area under the O-H peak was normalised to the peak area for the inert aromatic C=C mode at a wavelength of 1508 cm^{-1}, showing a ratio increase from $\frac{A_{peak,OH}(0)}{A_{peak,aromatic}(0)} = 5.81$ to $\frac{A_{peak,OH}(336)}{A_{peak,aromatic}(336)} = 9.33$. This ratio increase demonstrates a qualitative sign of water absorption inside the coating films.

The O-H peak at wavelength 3421 cm^{-1} is deconvoluted into four specified wavelengths (3623 cm^{-1}, 3555 cm^{-1}, 3419 cm^{-1} and 3264 cm^{-1}) using Gaussian function fitting, as shown in Figure 4.4.2a, to distinguish different states of water in the epoxy coating. Figure 4.4.3 illustrates the possible states of water inside the epoxy coating matrix with the corresponding wavelength footprints on the ATR-FTIR spectra. In Figure 4.4.2a, the total peak area of wavelengths 3555 cm^{-1}, 3419 cm^{-1} and 3264 cm^{-1} is larger than the peak area at the wavelength of 3623 cm^{-1}, indicating a greater amount of water in the hydrogen-bound state (which may include water-water interactions) compared to the free water state.

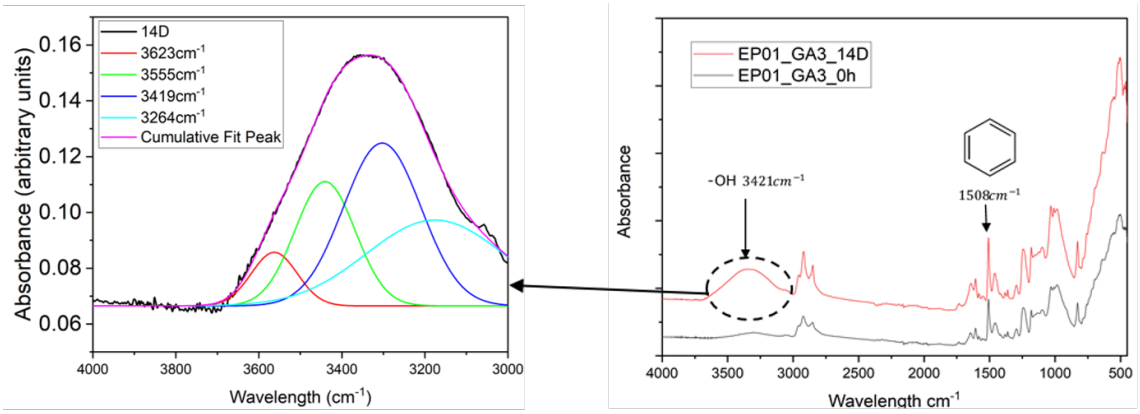

Figure 4.4.2: The OH peak was deconvoluted into four peaks at 3623cm^{-1}, 3555cm^{-1}, 3419cm^{-1} and 3264cm^{-1} (a), and the ATR-FTIR spectra of the free film before and after immersion are shown in (b).

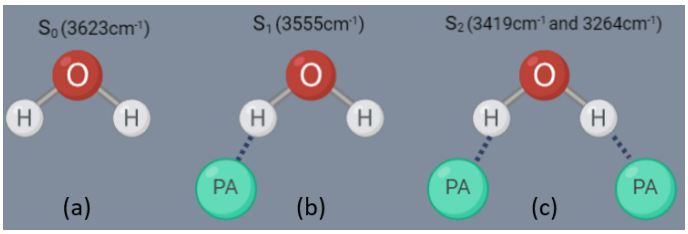

Figure 4.4.3: Water states: (a) S_0 illustrates free water molecules expressed in 3623 cm^{-1}, (b) S_1 represents a water molecule with one hydrogen bonding with a Proton Acceptor (PA) expressed in 3555 cm^{-1}, (c) S_2 stands for water molecules with two hydrogen bonding with a PA on each side expressed with 3264 cm^{-1} and 3419 cm^{-1}.

One limitation of the ATR-FTIR technique is that it only reaches 6 µm on the surface of the solid sample non-destructively. Therefore, if there is a gradient of water concentration throughout the coating layer, this technique as a standalone approach would be inadequate. Additionally, the deconvolution of the ATR-FTIR spectra only provides a theoretical indication of possible water states. Further experimental assessments are needed to support it.

4.4.3 SAM scanning of coating thickness

The SAM cross-section scanning results for the evolution of the coating thickness of coated steel sample (S47) are summarised in Table 4.4.1. It shows that the average coating thickness is slowly increasing as exposure time increases, particularly from 120 hours of immersion time. Comparing the initial coating thickness of 106±6 μm to the final thickness of 116±7 μm, a significant increase in coating thickness is observed.

Table 4.4.1: Coating thickness evolution of coated steel sample S47 evaluated from SAM B-scans.

Immersion time (hours)	Averaged coating film thickness (μm)	ϕ_{SAM} Water volume fraction inside coating determined by SAM
0	106±6	0
24	107±6	0.0052
48	108±7	0.0095
120	110±4	0.0323
216	113±5	0.0537
336	116±7	0.0890

The volume fraction of water uptake estimated from the SAM images is determined using Equations (4.4.1) and (4.4.2):

$$V_{water} = \Delta L(t) \cdot A = (L(t) - L(0)) \cdot A \tag{4.4.1}$$

where V_{water} is the volume of water inside the coating, $L(t)$ and $L(0)$ are coating thickness at time t and 0, respectively, and A is the exposed coating area.

The volume fraction of the water inside the coating film, denoted as ϕ_{SAM}, is then determined by:

$$\phi_{SAM} = \frac{V_{water}(t)}{V_{coating}(0)} \tag{4.4.2}$$

where $V_{coating}$ is the volume of the exposed coating.

The swelling process is monitored by scanning the coated steel substrates using SAM, where coating thickness is monitored from the cross-section images as shown in Figure 4.4.4 for sample S47. The B-scan images of one cross-section scan at 0 hours and 336 hours of exposure time are illustrated in Figure 4.4.4. It should be noted that the average coating thickness, as determined in Table 4.4.1, is based on five cross-section images with a total of 25 measurement points at one evaluation time.

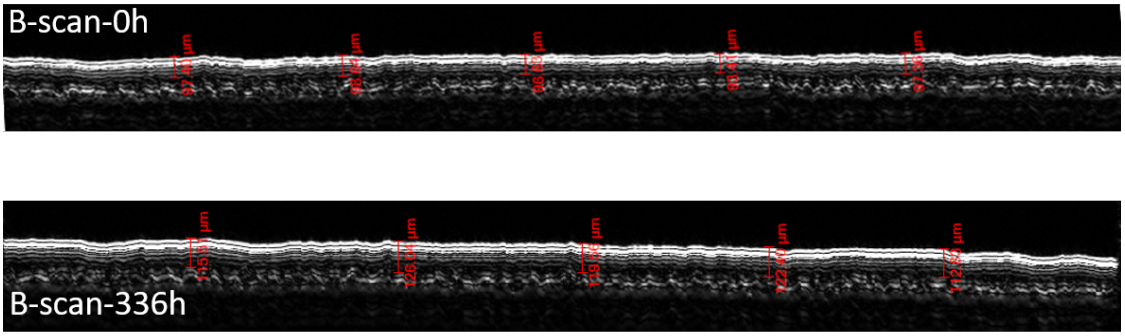

Figure 4.4.4: B-scan images of one cross-section scan at 0 hours and 336 hours of exposure time

The SAM results show the coating thickness has increased by 9 % (corresponding to 9 vol.% of water uptake by assuming all the expansion is due to water molecules) after 14 days of immersion. This demonstrates that the swelling process is occurring on the EP-01 coated steel sample and cannot be neglected. The SAM technique is suitable to measure swelling of the coating layer in situ during the water uptake process.

4.4.4 EIS measurement of water uptake

EIS measurements were used to study the water uptake into the epoxy coating free films and epoxy coated steel samples by monitoring the capacitance change over time. The EIS data from the EP-01 free films were fitted with an equivalent circuit model (ECM) such as R(RQ), which consists of resistance from the electrolyte R_s and the constant phase element (Q) in parallel with a resistance (R) element. This ECM model was utilised to describe the change of epoxy coating free films under immersion in 3.5 wt% NaCl solution.

For the coated steel sample, three electrical circuit models, namely R(RQ), R(RQ)(RQ), and R(RQ)-(Q(RW)), were utilised to fit the EIS data at different periods of exposure time, as illustrated in Figure 4.4.5. ECM 1-3 models were used to fit three different periods of water uptake: ECM 1 for 0-4 hours, where water diffusion is limited to the coating layer; ECM 2 for 6-48 hours, where water diffusion reaches the coating-steel interface and an extra (RC) element is added in parallel to describe the gradual coating-steel interface change; and ECM 3 for 72-336 hours, where a diffusion tail in the Nyquist plot at low frequency indicates a significant mass transport phenomenon. The raw EIS data for sample S47, along with reproducibility checks, are presented in Appendix B.4. The fitted data graphs with the corresponding equivalent circuit models are provided in Appendix B.4.4, and the fitting parameters are presented in Appendix B.4.5.

One may wonder how water can penetrate a commercial coating-steel interface within just 6 hours of immersion in the 3.5 wt% NaCl solution. However, a previous study observed

that the same EP-01 coating, when exposed to neutral salt spray, exhibited an impedance modulus lower than 10^6 Ωcm^2 after 24 hours of exposure. This confirms that the studied EP-01 commercial coating provides exceptionally weak barrier protection. Therefore, it is reasonable to assume that water reached the coating-steel interface after approximately 6 hours of immersion and fit the data with ECM 2 model, as all three samples show the same trend. Additionally, it should be addressed that once water molecules reach the coating-steel interface, it does not necessarily mean that corrosion process is occurring immediately.

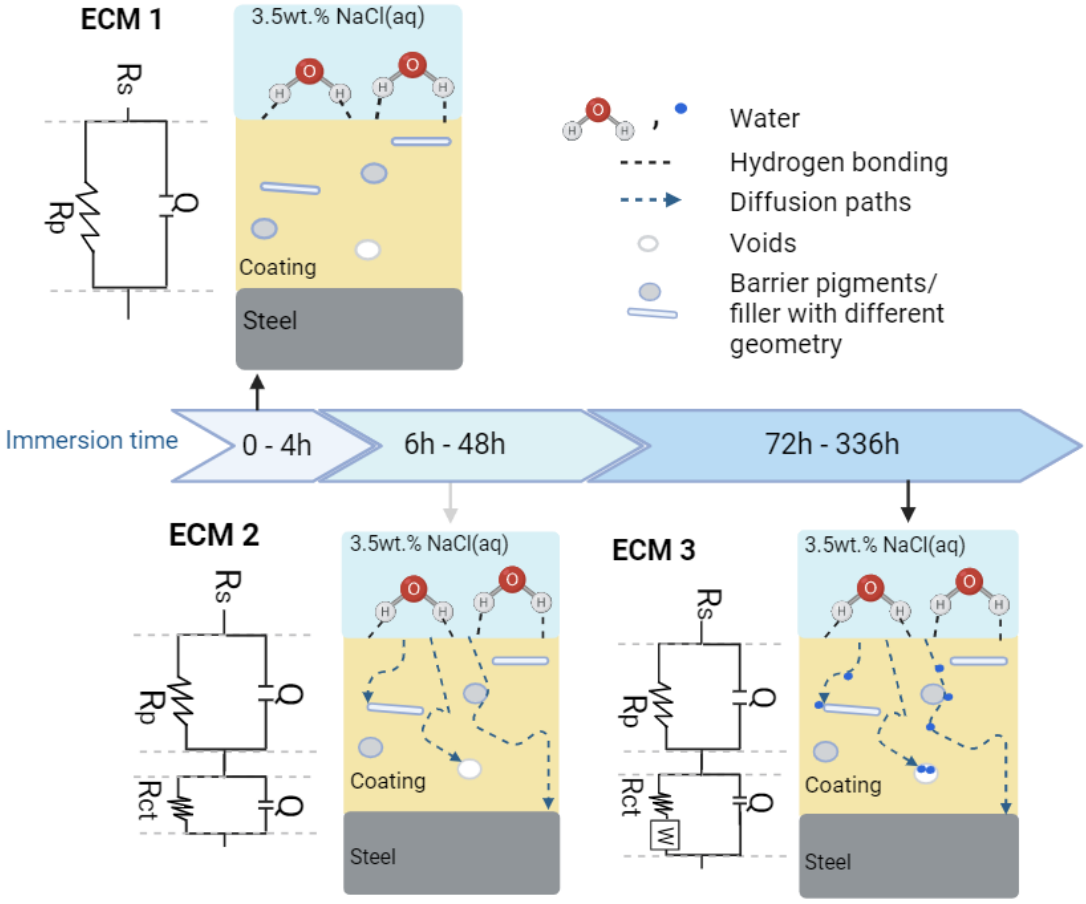

Figure 4.4.5: Equivalent circuit models applied for fitting the EIS data measured at different exposure periods ECM 1 between 0-4 hours, ECM2 from 6 – 48 hours and ECM 3 from 72 – 336 hours.

4.4.5 Coating capacitance determinations

Four different approaches for water uptake determination are presented by Equations (4.2.1) to (4.2.4) and (4.2.7). These approaches were applied to analyse the same data set, and the results are compared in Figure 4.4.6. A significant difference in the water uptake fraction ϕ is observed among the applied capacitance equations in Figure 4.4.6. One notable observation is that the water fraction inside the coated steel substrate, as determined by the high-frequency method and the mixing rule, follows the same pattern. A rapid water uptake occurs up to 48 hours, followed by a slower rate of water uptake up to 336 hours of immersion time. However, the estimated water uptake fractions at the end of the exposure

time differ between the two methodologies, with $\phi_{Mixing\ rule}$ being 18 vol.% and $\phi_{C_{HF}}$ being 27 vol.%.

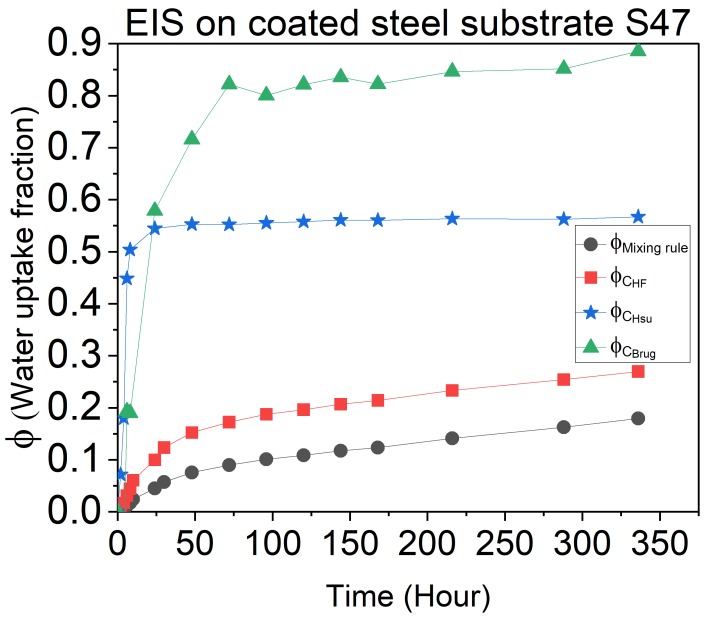

Figure 4.4.6: Water fraction (ϕ) estimated for coated steel sample using the Brasher Kingsbury equation with three different approaches (Brug et al. $\phi_{C_{Brug}}$, Hsu et al. $\phi_{C_{Hsu}}$, a fixed high-frequency $\phi_{C_{HF}}$) to determine the effective capacitance and compared them with the water uptake determination using the mixing rule $\phi_{Mixing\ rule}$).

The water uptake fractions determined by applying C_{Brug} and C_{Hsu} exhibit unrealistic patterns and/or excessively high water content levels. The estimated values of $\phi_{C_{Brug}}$=56 vol% and $\phi_{C_{Hsu}}$=89 vol% at the end of the exposure time are considered unrealistic, especially since no signs of blistering formation were observed. The significant deviation in the water uptake fraction estimated by the applied Brug et al. and Hsu-Mansfeld equations may be attributed to the original equations, which were designed to describe the double-layer capacitance between an electrolyte and a metal system. In this case, these equations are found to be unsuitable for a coated metal system immersed in an electrolyte. Another factor contributing to the inaccuracy of the applied equations could be the sensitivity of the Brug et al. and Hsu-Mansfeld equations to the actual value of the constant phase parameter (n). Kakaei et al. [79] reported that for n<0.8, the determined values of capacitance can vary by several magnitudes. The CPE parameters (Y and n) fitted with the applied equivalent circuit models for coated sample S47 are provided in Appendix B.4.5. Thus, careful consideration is necessary when selecting a suitable equation for the water uptake study of the investigated coating system, particularly for assessing a commercial coating film where the recipe is confidential and limited information is available. Therefore, it is essential to employ multiple evaluation techniques to cross-check the reliability of the obtained water uptake levels. In this study, the mixing rule approach is adopted for further determination of water uptake, as the results obtained are relatively closer to those from the gravimetric analysis.

4.4.6 Comparison of the applied techniques for water uptake monitoring

The results obtained from the applied non-destructive evaluation techniques: 1) Gravimetric analysis, 2) SAM, and 3) EIS on both coated film on steel substrate and free films, respectively, are represented in Figure 4.4.7.

The gravimetric and EIS evaluations on free films show three stages of uptake: 1) rapid water absorption within 8 hours, 2) a slower rate of water uptake between 8-72 hours of the exposure time, and 3) a decrease in the water content after 72 hours of exposure time. Furthermore, the results in Figure 4.4.7 demonstrate that the trends of water uptake measured by EIS and gravimetric analysis on the free film exhibit similar patterns. However, the maximum water uptake level estimated from gravimetric analysis on the free films (5 vol%) differs from that estimated by EIS measurements (13 vol%), indicating that EIS measurements may tend to overestimate the water uptake level compared to gravimetric measurements.

In addition, both gravimetric results (red triangle data points in Figure 4.4.7) and EIS measurements of the epoxy free film (blue star data points in Figure 4.4.7) show a decreasing trend. This can be attributed to the leaching of components from the free films during the immersion time, as reported in previous studies [83, 89].

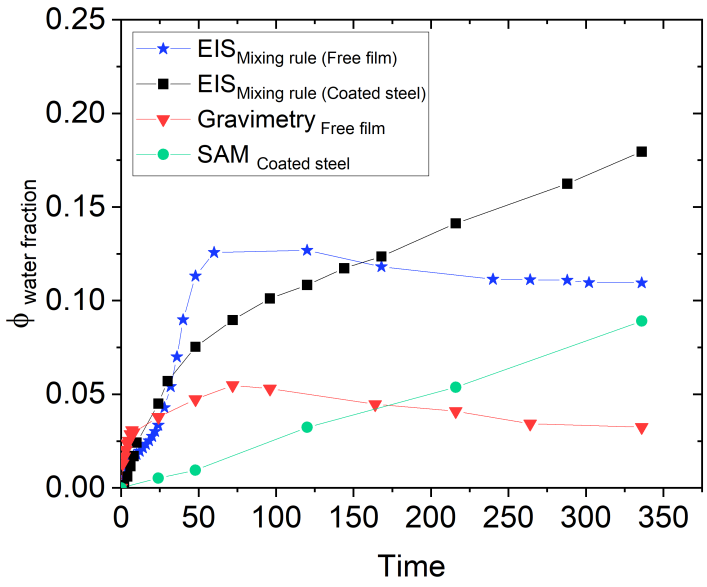

Figure 4.4.7: (a) Water uptake results obtained by gravimetric evaluation of the free films, SAM scanning of coated steel sample S47, EIS measurements of coated steel sample S47 and the free film (with replications presented in Appendix B.4.6)

The water uptake process differs between a coating free film and a coating film applied on a substrate, as shown in Figure 4.4.7. This difference can be explained by the larger area available for water diffusion into the free film samples (with double sides) compared to the coated steel substrate (with only one side) as illustrated by Figure 4.4.8. The difference in the exposure area may accelerate the water uptake process, resulting in a faster

initial uptake in the free films (red triangle data in Figure 4.4.8) compared to the coated steel substrate (black square data in Figure 4.4.8) within the first 8 hours of the immersion. Gravimetric and EIS evaluation of independent free film samples show both that a slower water uptake rate appears after 10 hours of immersion, this may be due to counteracting effects between water uptake, swelling and leaching processes as discussed in Section 4.3.3.

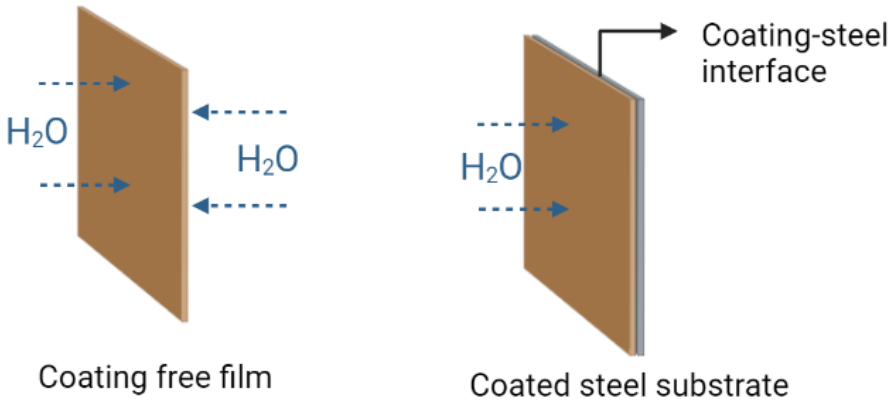

Figure 4.4.8: Simplified illustration of water diffusion paths through a free film and a coated steel substrate.

For the coated steel substrate S47 evaluated by EIS technique (black square data in Figure 4.4.8), the water uptake process appears slower compared to the free films due to one side exposure area, a longer diffusion path for water to the coating-steel interface to reach a saturation stage leads to a gradual swelling process. The water uptake profile of coated steel sample S47 (black square data in Figure 4.4.7) shows a slower rate of water uptake between 72-336 hours similar to the phase P2 (Figure 4.4.1b) observed in the free films. During 72-336 hours, the swelling of the coating layer on S47 is significant, as confirmed by SAM measurements (green dot data in Figure 4.4.7). It is seen that SAM evaluation of water uptake trend is completely different compared to the results of EIS and gravimetry. This indicates that the SAM technique is not suitable for water uptake level estimation as it is unable to capture water uptake before swelling. Therefore, the technique is only suitable for the swelling process detection of the coating layer.

4.4.7 Mechanism of water diffusion into epoxy coated steel substrate

Figure 4.4.9 illustrates a proposed mechanism for the water uptake process into epoxy coated steel substrate. The diffusion of ions is excluded from the illustration for simplification, but it should be noted that ions also ingress into the coating layer during exposure. Step 1 in Figure 4.4.9 presents a proposed idea for the early stage of immersion when a dry epoxy coating film is immersed in a 3.5 wt.% NaCl solution. The first chemical interaction between the epoxy coating surface and water molecules in the bulk solution may be the hydrogen bonding interaction. However, it should be clarified that none of the applied techniques have confirmed this phenomenon.

Figure 4.4.9 Step 2 illustrates that besides the hydrogen bonding interaction of water molecules at the coating surface, water molecules may gradually diffuse into the epoxy coating film through diffusion paths and fill up the voids. As a result, the epoxy coating film layer becomes gradually saturated, and water uptake, swelling, and leaching processes coexist. These processes were observed through gravimetry, EIS, and SAM evaluations.

Figure 4.4.9 Step 3 demonstrates the simultaneous process of quasi-saturation and swelling. The water molecules are believed to be randomly distributed within the coating film, and a significant swelling process of the coating layer is occurring. Additionally, as illustrated, some of the water molecules may also reach the coating-steel interface.

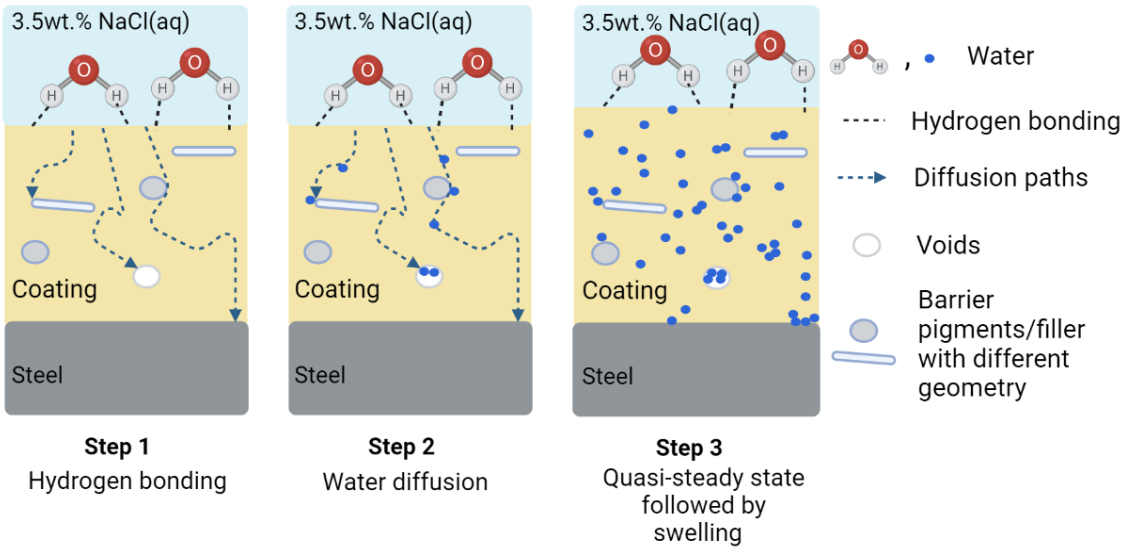

Figure 4.4.9: A sketch illustrates the water uptake process into organic barrier coating film divided into three steps: hydrogen bonding, water diffusion, and a quasi-saturation state followed by swelling. For simplification, ions in the bulk solution (3.5 wt.% NaCl solution) and leaching process are excluded from the illustration.

For further immersion times, which were not reached in this study, it is expected that the accumulation of water molecules at the coating-steel interface generates a potential difference. This potential difference can cause the anodic corrosion reaction of iron atoms in the steel substrate, while simultaneously, the cathodic reduction reaction of oxygen atoms also occurs, as shown in Figure 4.4.10a. The swelling of the coating film may be attributed to the occupation of voids inside the coating matrix by water molecules.

The interaction of water molecules with the coating matrix can also plasticise the epoxy matrix, leading to polymer matrix expansion, as illustrated in the enlarged polymer network in Figure 4.4.10b. For incomplete wetting of pigments/filler inside the coating layer, water molecules may also form hydrogen bonding to the pigments, as illustrated by Figure 4.4.10c.

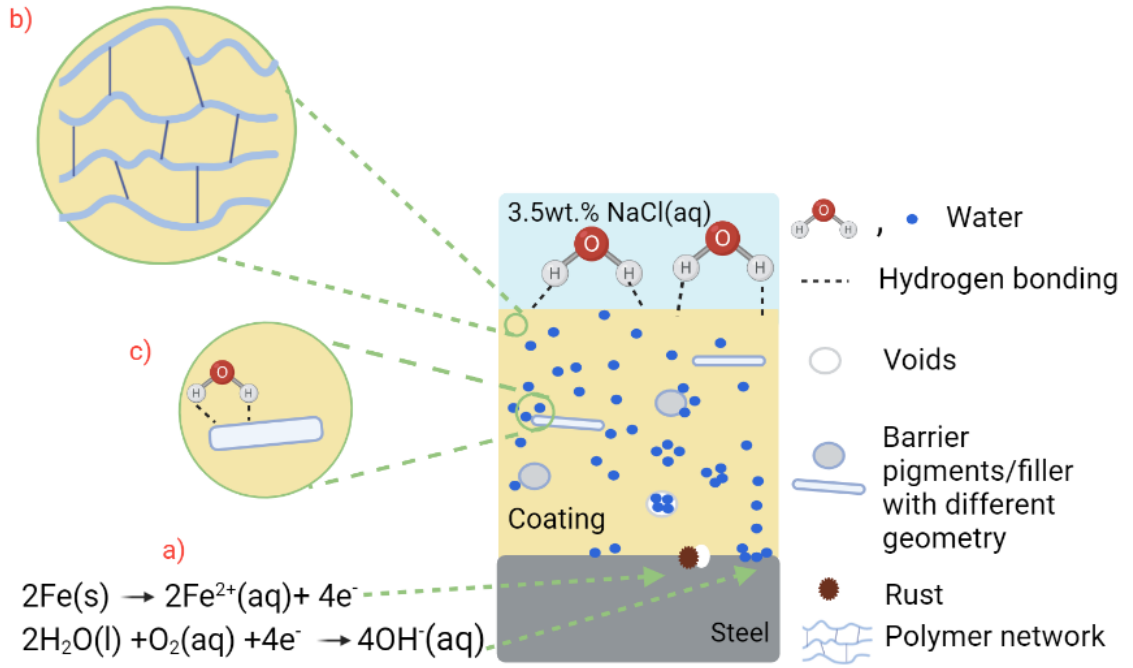

Figure 4.4.10: Sketch of water uptake after the quasi-saturation stage where a) iron corrosion initiation at the coating-steel interface, b) swelling of the coating film initiates through polymer matrix expansion, hydrogen bonding interaction both on the coating surface and c) on incompletely wetted pigments. Ions in the bulk solution (3.5 wt.% NaCl solution) and leaching process are excluded in the illustration for simplification.

4.4.8 Advantages and limitations of the applied techniques

The non-destructive techniques applied in this study are summarised in Table 4.4.2. The table includes the actual measured parameter for each technique, the sample form requirement, measurement time, and limitations. The gravimetric measurement is easily operated as it monitors the mass change of the sample using a balance. However, uncertainty can arise when there is leaching of components, so the measured mass should be adjusted to account for the mass loss leached into the bulk solution, in order to precisely isolate the mass change due to water uptake.

The ATR-FTIR technique is also straightforward for performing measurements and analysis. However, a limitation of this technique is that it can only measure a few micrometres on the surface of the sample, which is limited when a water gradient may occur in a thick coating layer. The deconvolution of ATR-FTIR spectra can provide theoretical indications of water states within the coating. However, further verification of the results may be necessary using other techniques.

The SAM technique is used to monitor water uptake by measuring coating thickness changes. Operating the machine and obtaining proper images require a lot of experience.

The SAM B-scan mode can be applied to detect swelling of coating systems. However, it is important to note that using thickness change as an indicator to determine the water content of the coating film may result in underestimating the actual water content. This is because the swelling process becomes dominant at a later phase, while the initial water uptake would be excluded by this method.

EIS measurements can be used to assess water uptake in coatings, whether they are applied to free films or coated metallic samples. The EIS setup is relatively practical to operate, but interpreting the EIS data accurately requires a solid understanding of the coating protective system and electrochemistry. The results from this study indicate that the EIS technique tends to overestimate the water uptake level when compared to gravimetry.

Table 4.4.2: Summary of non-destructive methods applied in this study and their benefits and limitations.

Technique	Measured parameter	Sample form	Measurement time	Operational requirement	Limitations
Gravimetry	Mass	Free film	<1 min	low	leaching of ingredients
ATR-FTIR	O-H bending absorbance	Free film/ Coated substrate	1 min	low	Limited to the surface detection 6 μm
SAM	Thickness of coating	Coated substrate	3-5 min	High	Required swelling to apply for water uptake and may underestimate water uptake level
EIS	Capacitance of coating	Free film/ Coated metallic substrate	30 min	Medium	Overestimating water uptake level

4.5 Conclusion

Non-destructive evaluation techniques, including gravimetric analysis, ATR-FTIR, EIS, and SAM, were applied for water uptake measurements of the epoxy coating system immersed in 3.5 wt.% NaCl solution. The following conclusions can be drawn:

1. Water uptake into epoxy coating free film proceeds through rapid absorption, a slower continuous water uptake rate, and is followed by leaching of the coating ingredients.
2. Water uptake into coated steel substrate shows rapid absorption and a slower continuous water uptake rate due to swelling of the applied coating layer.
3. SAM technique is feasible for non-destructively detecting of swelling process during the water uptake.

5 A quantitative real-time evaluation of rust creep propagation in coating systems exposed to field testing and cyclic ageing test

This chapter has been written in a manuscript format and has been submitted to the peer-reviewed journal *Progress in Organic Coatings*.

The rust creep propagation mechanism of zinc-rich epoxy primed and epoxy primed two-layer coating systems is investigated in the field and cyclic ageing test, respectively.

Highlights

1. *Two-layer coating systems exposed in the field and the cyclic ageing test.*
2. *Scanning acoustic microscopy is effective in revealing rust creep propagation.*
3. *Rust creep propagates via a linear kinetic function over exposure time.*

Abstract

This study investigated the rust creep propagation of two different coating systems, an epoxy primed (EP/PUR) and a zinc-rich epoxy (ZnEP/PUR) primed coating system exposed to the field and the accelerated cyclic ageing test. Non-destructive scanning acoustic microscopy (SAM) was used to assess the coating samples and detect rust creep propagation. The results showed a linear increase in rust creep propagation over time in all coating systems exposed to the field and the cyclic ageing test. The EP/PUR coating system exhibited a rust creep propagation rate of 0.228 mm/week under field exposure and 0.380 mm/week in the cyclic ageing test, while the ZnEP/PUR coating system showed rates of 0.024 mm/week under field exposure and 0.292 mm/week in the cyclic ageing test. Notably, the rust creep propagated through filiform corrosion mechanism under field exposure for both coating systems and that was not observed in the cyclic ageing test. The reliability of evaluating the anti-corrosive performance and rust creep growth around a scribe of different anti-corrosive coating systems exposed to the accelerated cyclic ageing test, as defined in ISO 12944-9, is questionable. The study highlights the benefits of applying non-destructive scanning acoustic microscopy for rust creep propagation investigation capturing information that may be missed by the traditional standardised method.

Keywords: *Filiform corrosion, Rust creep, Field testing, Cyclic ageing test, Scanning Acoustic Microscopy*

5.1 Introduction

Organic coating systems are widely applied for the protection of metallic structures in offshore and marine environments [20]. Full commercial anticorrosive coating systems can protect steel substrates for 15-20 years [8], making the real field data collection and coating performance evaluation a time-, manpower- and resource-consuming process. As a result, accelerated laboratory tests were adopted to reduce the time required for coating performance evaluation. The International Standards Organization (ISO) and the American Society of Testing and Materials (ASTM) formulated the commonly accepted accelerated laboratory tests for coatings. Accelerated testing offers the advantage of generating data rapidly under predefined and continuously controlled exposure conditions throughout the test. The ideal goal of accelerated laboratory tests is to simulate natural exposure conditions while maintaining the same coating degradation mechanisms within a shorter time frame. Further, it allows for faster product development, optimisation and quality control. However, field exposure test is still needed to verify the accelerated testing results which can show the coating performance under real application conditions.

According to ISO 12944-9 [90], the rust creep assessment is widely applied for coating performance evaluation, where the rust creep is assessed by removing the detached coating around the scribe and measurement of an averaged rust creep distance from the scribe. The drawback of using rust creep evaluation according to the current standard is that the approach is destructive which restricts further examination. This is because the removal of the detached coating renders the sample to be unsuitable for further exposure.

Non-destructive methods can be used to evaluate rust creep propagation of a coated panel over time, allowing for a better understanding of the coating behaviour and the working mechanism behind. This facilitates the monitoring of the rust creep growth kinetics and the development of prediction models of coating deterioration. Additionally, the use of non-destructive methods can save time and resources for the assessment of coating performance which will better facilitate the screening and prequalification of new coating formulations.

Considering the destructive nature of the rust creep evaluation according to ISO 12944-9 [90], non-destructive evaluation methods are drawing wide attention. Weinell and Rasmussen [8] proposed the application of infrared thermography for rust creep assessment and their results showed a strong correlation in rust creep assessment between infrared thermography images and the destructive standardised approach. However, this technique is based on the detection of the difference in heat conductance between materials (i.e., coating and corrosion products), and the heat exposure may lead to further coating deterioration. 3D profilometry is another non-destructive evaluation technique to characterise coating failures through monitoring the topographical profile of coatings [91]. Scanning Acoustic Microscopy (SAM) can also be utilised to assess coating failures such as blistering [28], delamination [51, 92, 55, 53] and rust creep [91]. These techniques have the ability to monitor coating failures without causing damage. However, the comparison of rust creep propagation between field exposure and accelerated cyclic ageing test by using these non-destructive evaluation techniques is still limited.

The objective of this study is to quantitatively evaluate the rust creep propagation of the coating systems exposed to different environments, including the field exposure and the accelerated cyclic ageing test condition. Scanning acoustic microscopy will be applied

which enables continuous monitoring of the coating degradation and following the rust creep kinetics in a non-destructive way, thereby leading to a better understanding of the coating failure mechanisms.

5.2 Experimental

5.2.1 Sample preparation

All samples were prepared from S235JR steel panels with dimensions 150 m x 75 mm x 3 mm. They were sandblasted to a cleanliness of Sa 2½ (ISO 8501-1 [93]) before the coatings were applied by airless spray. Two different coating systems were tested as described in Table 5.2.1. All coating systems were composed of two layers of commercial paint products which are zinc-rich (ZnEP/PUR) primed and epoxy primed (EP/PUR) with a polyurethane topcoat. The zinc-rich epoxy primer (ZnEP, ≥80 wt.% Zn dust) and epoxy primer (EP) are both two-component aromatic amine adducts cured with bisphenol A. The backside and edges of the panels were sealed with a two-component epoxy coating with a draw-down coating applicator. The panels were left for curing in the fumehood for 7 days and then kept in a sealed plastic until exposure. An artificial scribe with a dimension of 50 mm x 2 mm was made down to the steel according to ISO 12944-9 [90].

Table 5.2.1: Coating systems with nominal dry film thickness (NDFT) and actual measured dry film thickness (DFT) are presented, with each coating system having two replication designations denoted by a subscript $_R$. The DFT of the coating is intentionally lower than the recommended thickness of a full coating system to accelerate the coating degradation rate [94].

No.	Coating systems	1^{st} coat NDFT= 40 µm	2^{st} coat NDFT= 40 µm	DFT_{total} µm	Exposure condition
S64	ZnEP/PUR	Zinc-rich epoxy	Polyurethane	100±3	Field
S65	ZnEP/PUR_{R1}	Zinc-rich epoxy	Polyurethane	99±3	Field
S66	ZnEP/PUR_{R2}	Zinc-rich epoxy	Polyurethane	101±7	Field
S77	EP/PUR	Epoxy	Polyurethane	115±6	Field
S75	EP/PUR_{R1}	Epoxy	Polyurethane	112±4	Field
S76	EP/PUR_{R2}	Epoxy	Polyurethane	113±5	Field
S67	ZnEP/PUR_{CAT}	Zinc-rich epoxy	Polyurethane	101±4	Cyclic ageing test
S68	ZnEP/$PUR_{CAT,R1}$	Zinc-rich epoxy	Polyurethane	121±4	Cyclic ageing test
S69	ZnEP/$PUR_{CAT,R2}$	Zinc-rich epoxy	Polyurethane	103±6	Cyclic ageing test
S72	EP/PUR_{CAT}	Epoxy	Polyurethane	117±9	Cyclic ageing test
S73	EP/$PUR_{CAT,R1}$	Epoxy	Polyurethane	114±3	Cyclic ageing test
S74	EP/$PUR_{CAT,R2}$	Epoxy	Polyurethane	115±5	Cyclic ageing test

5.2.2 Exposure testing

5.2.2.1 Marine atmospheric exposure in the field

The samples were exposed on a floating raft (Figure 5.2.1a) at CoaST Maritime Test Centre (CMTC) located in Hundested, Denmark [59]. The field exposure was initiated in April 2021 and with a duration of 15 months. The duration of exposure is calculated based on the actual time that the panels were placed in CMTC except for the time when panels were brought to the laboratory for assessment. For evaluation in the laboratory, the panels were removed from the field conditions and kept under room conditions for roughly one week before returning the panels to the field. Despite this temporary removal, it is assumed that the coatings' degradation characteristics are not affected by the overall exposure duration.

All panels were fixed to the first row of the rack with the artificial scribe facing upwards as shown in Figure 5.2.1d. Panels in the first row were constantly above the waterline (Figure 5.2.1c) where the growth of fouling at the coating surface was limited.

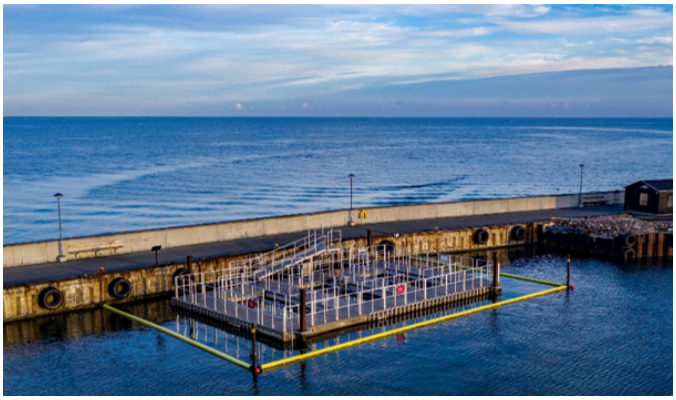

(a) CMTC Floating raft

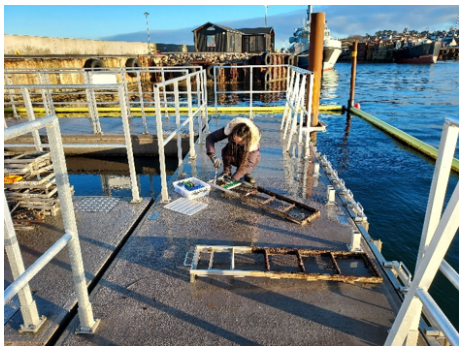

(b) Mounting samples on Row 1 of the rack

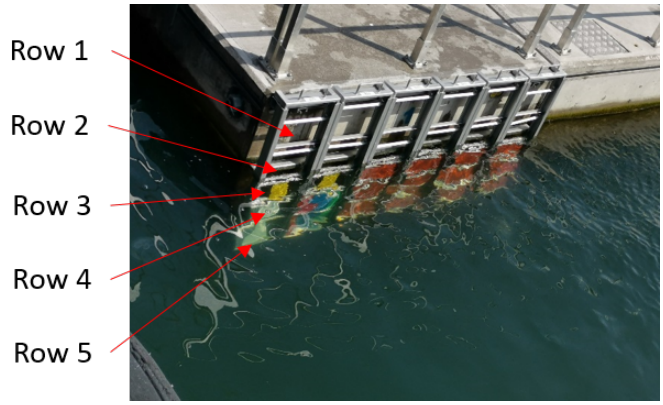

(c) Example of the water level regarding to the rows on the racks

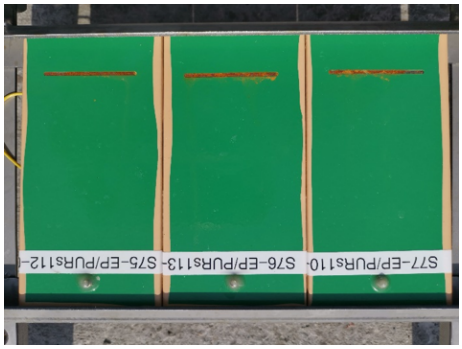

(d) Illustration of sample positioned in the rack

Figure 5.2.1: (a) CoaST Maritime Test Centre (CMCT) floating raft; (b) Sample mounting on Row 1 of the rack; (c) An illustration of the water level when the rack is submerged and (d) positioning of the samples in the first row (Row 1) of the rack.

5.2.2.2 Cyclic Ageing Test (CAT)

The full test consists of 25 exposure cycles with each cycle comprised of 72 hours of exposure to the neutral salt spray, 72 hours of exposure to UV and condensation and 24 hours of exposure to low temperature at -20±2 °C as specified in ISO 12944-9 [90].

5.2.3 Rust creep evaluation

5.2.3.1 Scanning Acoustic Microscopy (SAM) Technique

A scanning acoustic microscope from PVA TePla, SAM 301 HD^2 with a transducer of 125 MHz was applied to assess the rust creep propagation around the scribe after exposure of the coated sample to the field and accelerated laboratory test. Deionised water was used as the coupling medium between the transducer and the coated sample to ensure efficient delivery of acoustic ultrasound waves [95]. A scan resolution of 50 µm/pixel is set to reduce the scanning time and minimise the exposure time of the coated sample in deionised water while scanning. Images were recorded with the reflected signal gated at the coating/steel interface.

5.2.3.2 Non-destructive rust creep evaluation

In the present study, the rust creep propagation is measured non-destructively by analysing the recorded SAM image of the coating/steel interface as illustrated in Figure 5.2.2. The rust creep is quantified in ImageJ software using Equation (5.2.1) which is specified in ISO 12944-9 [90]:

$$M = \frac{C - 2}{2} \tag{5.2.1}$$

Where M (mm) is the crust creep distance, C (mm) is calculated by averaging the nine lines consisting of the central line 5 and four lines with a separation of 5 mm on either side, as depicted in Figure 5.2.2. In Equation (5.2.1), the value 2 in the numerator is the subtraction of the initial scribe width in millimetres and 2 in the denominator is the two sides from the scribe which rust creep growths.

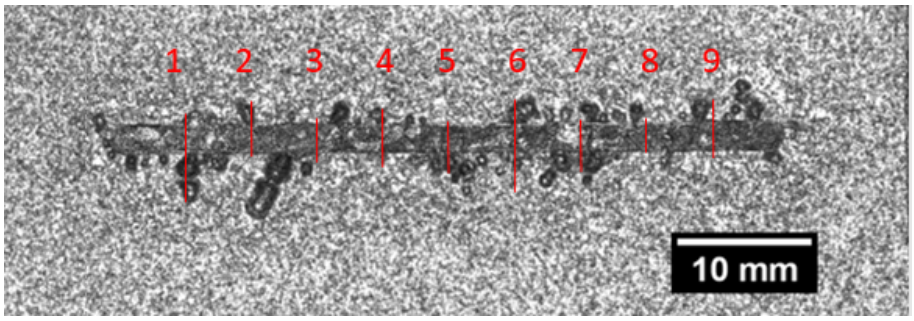

Figure 5.2.2: Illustration of rust creep measurement based on SAM image of coating/steel interface.

5.3 Results and discussion

5.3.1 Rust creep propagation under field exposure

5.3.1.1 EP/PUR coating systems

The rust creep propagation of EP/PUR coating system exposed in the field is illustrated in Figure 5.3.1, which includes optical images taken of the sample surface and SAM images at the coating/steel interface.

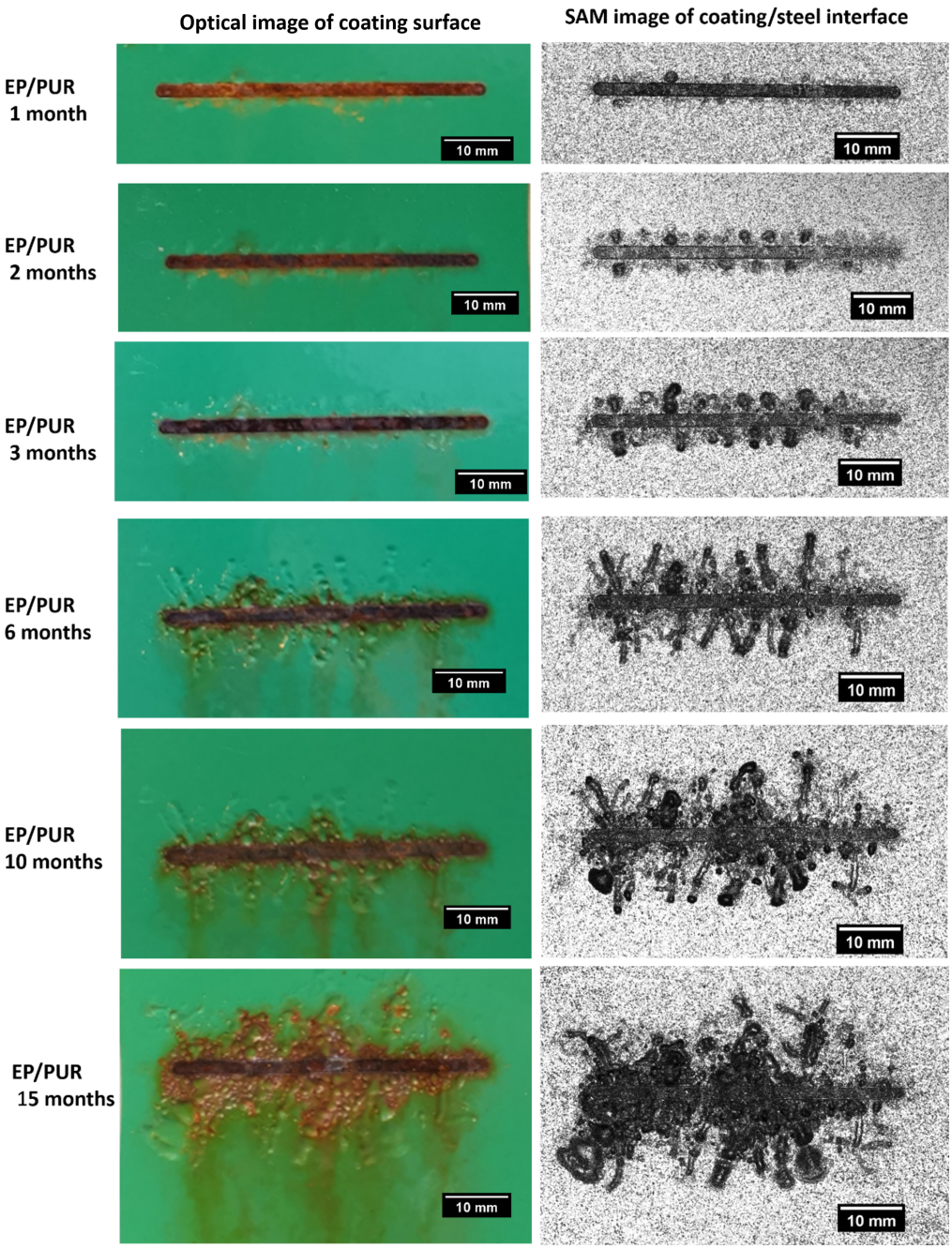

Figure 5.3.1: The EP/PUR coating system (S77) exposed in the field evaluated after 1, 2, 3, 6, 10, and 15 months of exposure time are presented. The replicated samples of EP/PUR (S76 and S75) system are presented in Appendix C.1.

Visual degradation around the scribe was observed in the optical images, as evidenced by coating morphology changes. Additionally, SAM images of the coating/steel interface revealed an unexpected rust creep propagation on the steel substrate, which progresses through (i) blister formation around the scribe through the first two months of exposure time, (ii) filiform-like propagation from the filament head up to 10 months of exposure, and (iii) merged filaments to a connected rusted area around the scribe. As shown by the SAM images of the coating/steel interface, filiform corrosion initiates at the local predefined scribe. During the exposure, coating around the scribe area gradually loses its adhesion to the steel substrate. This allows aggressive species from the environment to gain access and initiate blister formation which in this case is also filament head formation. The filament growth starts from the previous filament head as shown in Figure 5.3.1, where anodic oxidation of iron is expected to occur inside the head, while cathodic reduction of oxygen takes place behind the head [14]. The filiform corrosion mechanism is commonly observed in aluminium alloys [96, 13, 97], and in this study, filiform-like corrosion has also been detected on coated steel substrates exposed in the field, as shown in Figure 5.3.1 with replications presented in Appendix C.1.

5.3.1.2 ZnEP/PUR coating systems

The rust creep propagation of ZnEP/PUR coating systems exposed in the field is shown in Figure 5.3.2. Once again, there is a clear contrast between optical images and SAM images of the coating-steel interface, where rust propagation is easily observed in SAM images.

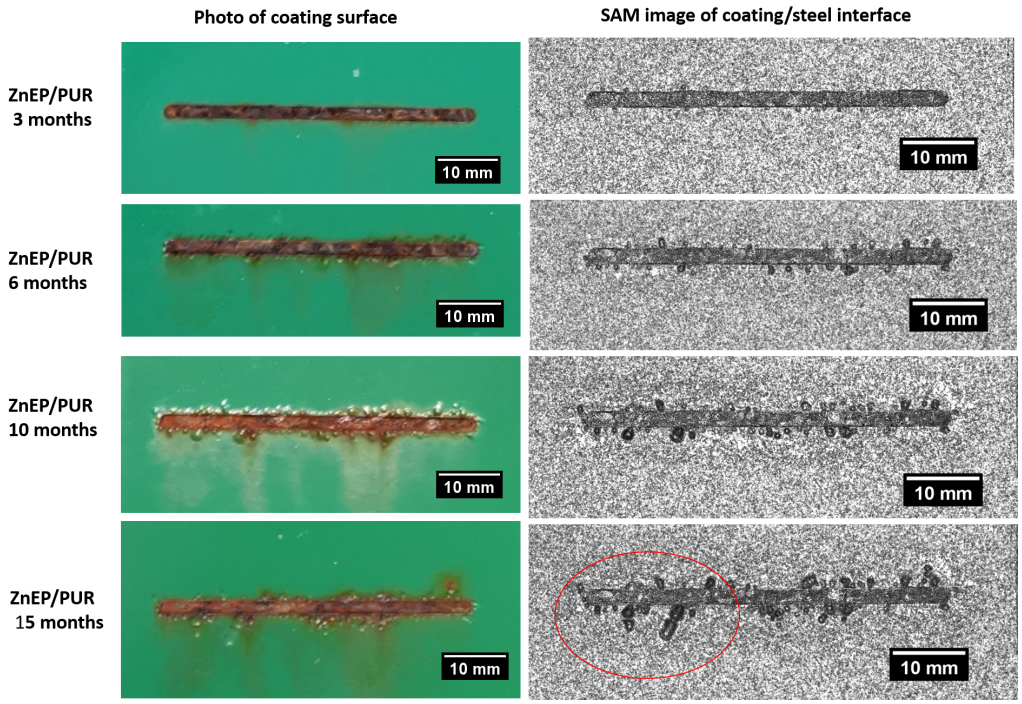

Figure 5.3.2: The ZnEP/PUR coating system (S64) exposed in the field evaluated after 3, 6, 10, and 15 months of exposure time are presented. The replicated samples of ZnEP/PUR (S65 and S66) system are presented in Appendix C.2.

The SAM images of coating/steel interface of ZnEP/PUR coating system exhibit a similar filiform corrosion pattern as observed in EP/PUR coating system with the initiation

of small filament heads and subsequent growth of filaments from these formed heads. The filiform corrosion propagation becomes evident for ZnEP/PUR coating system after 15 months of exposure in the field, as highlighted by the red circle in the SAM image corresponding to the 15 months of exposure time in Figure 5.3.2.

Notably, after 15 months of exposure of the ZnEP/PUR coating system in the field, only filiform corrosion initiation was observed, while for the EP/PUR coating the merging of filaments into a large connected rusting area around the scribe was detected. These results demonstrate the significant efficiency of sacrificial protection from zinc particles in the ZnEP/PUR system against corrosion compared to the EP/PUR systems. Similar findings regarding better corrosion protection provided from zinc-rich primer compared to epoxy primer exposed to the field were also reported by Knudsen et al. [98]. The zinc-rich primed coating system provides better rust creep protection due to the galvanic protection from zinc pigments. The corrosion of zinc pigments forms an inert and dense zinc oxide, which enhances the barrier property of the coating and thereby limits rust creep propagation. In contrast, the epoxy primed coating system provides only pure barrier protection, and once detachment of the coating occurs through rust creep growth, limited protection remains.

As presented in Sections 5.3.1.1 and 5.3.1.2, filiform corrosion propagation around a pre-defined scribe was observed for both EP/PUR and ZnEP/PUR coating systems exposed in the field. However, ZnEP/PUR coating system offers much better protection than the EP/PUR system due to the galvanic protection mechanism. The rust creep propagation kinetics of these two coating systems exposed to the field are presented in Section 5.3.4.

5.3.2 Rust creep propagation under cyclic ageing test

Cyclic ageing test (ISO 12944-9 [90]) consisting of 25 cycles was conducted for EP/PUR and ZnEP/PUR coating systems with visual rust creep propagation presented below.

5.3.2.1 EP/PUR coating systems

The rust creep propagation of EP/PUR coating system exposed to cyclic ageing test is presented in Figure 5.3.3, which includes the optical images of the sample surface and SAM scanning images of the coating/steel interface.

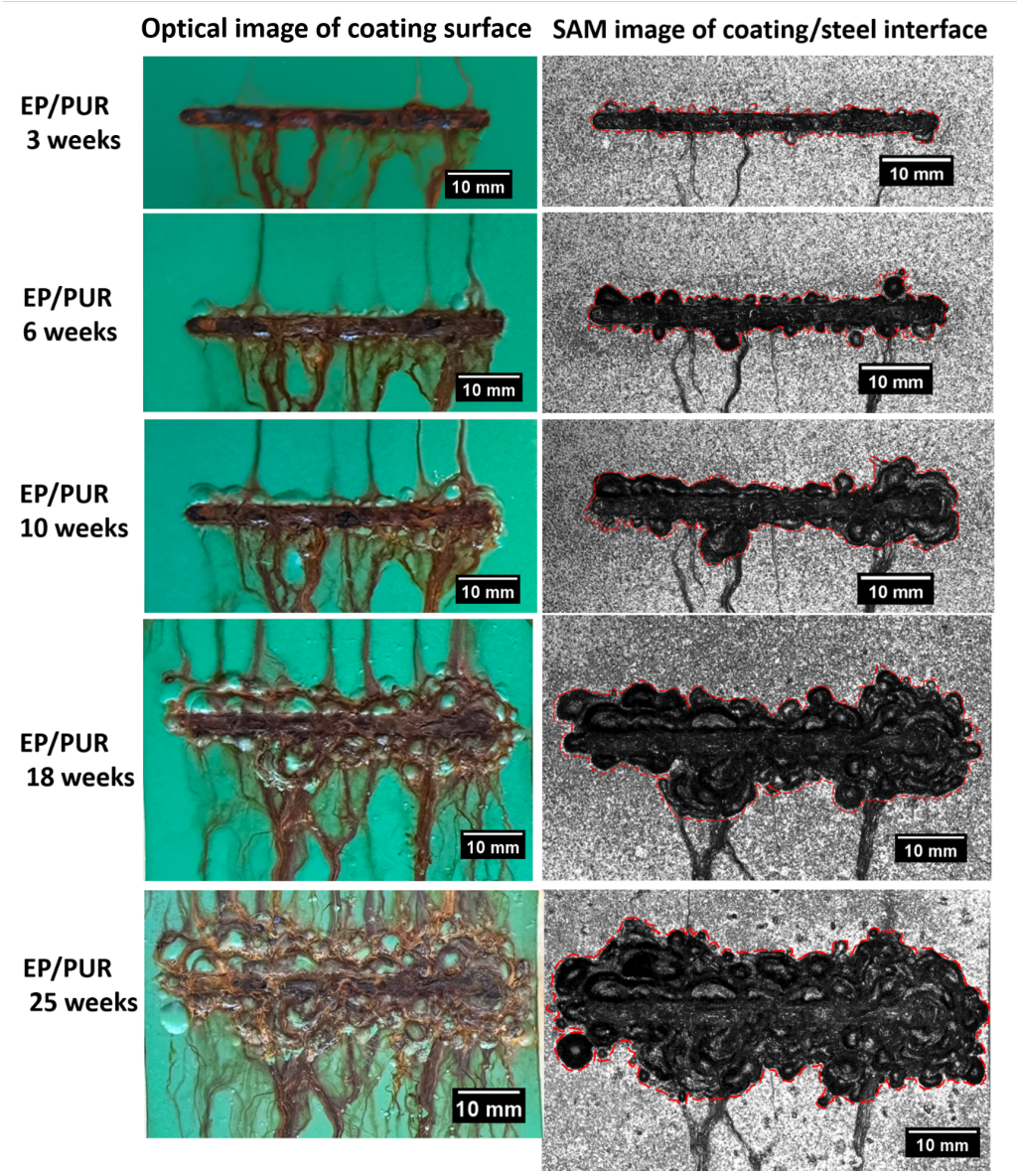

Figure 5.3.3: The EP/PUR coating system (S72) exposed in the cyclic ageing test evaluated after 3, 6, 10, 18 and 25 weeks of exposure time are presented. The replicated samples (S73 and S74) of EP/PUR system are presented in Appendix C.3.

It should be noted that in the optical images of Figure 5.3.3, there are corrosion product lines running from the scribe and adhering to the coating surface. Some of these corrosion product lines are visible in the SAM scanning image of the coating/steel interface due

to their thickness, which creates a strong acoustic impedance reflection that cannot be avoided by the transducer. It is important to emphasise that these signals originate on the coating surface and not from defects at the coating/steel interface. Thus, the true rust creep area is circled by the red dashed line on the SAM scanning images of the coating/steel interface for clarification.

The results demonstrate that the rust creep propagates from small blister formations around the scribe. These blisters gradually expand and merge with nearby blisters, contributing to the overall growth of the rust creep area. However, the EP/PUR coating system exposed in the cyclic ageing test did not exhibit a filiform-like corrosion mechanism, which is observed in the field exposure. This suggests that the degradation mechanism experienced by the EP/PUR coating systems in the field may be more complex than what can be captured by the accelerated ageing test.

5.3.2.2 ZnEP/PUR coating systems

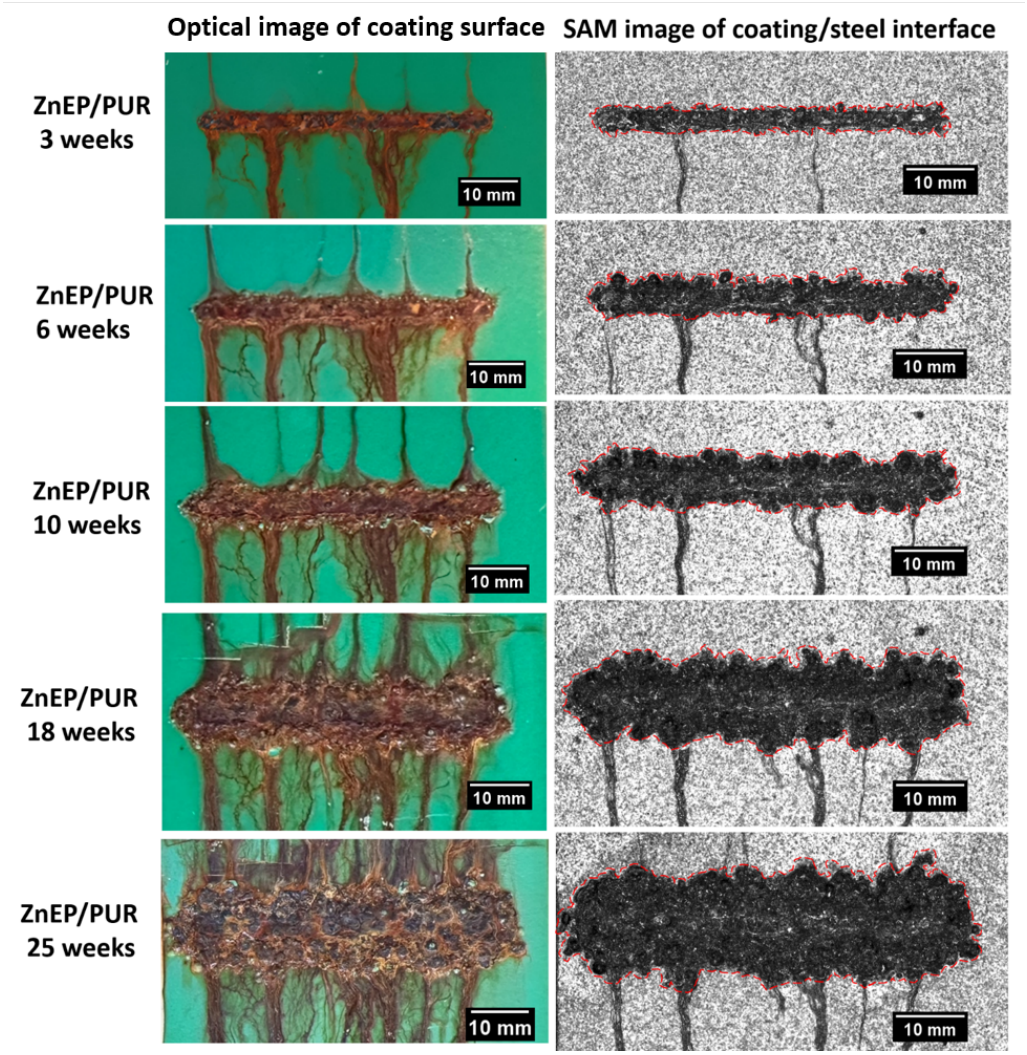

Figure 5.3.4: The ZnEP/PUR coating system (S67) exposed in the cyclic ageing test evaluated after 3, 6, 10, 18 and 25 weeks of exposure time are presented. The replicated samples (S68 and S69) of EP/PUR system are presented in Appendix C.4.

Figure 5.3.4 illustrates the rust creep corrosion propagation of ZnEP/PUR coating systems exposed to the cyclic ageing test. On the SAM images, the true rust creep area at the coating/steel interface is highlighted with red dashed lines. The results reveal that the rust creep initiates with small blister formations and then propagates uniformly from the scribe, exhibiting a different pattern compared to the rust creep growth in EP/PUR coating system exposed to the cyclic ageing test. In contrast to the field results, the rust creep propagation of ZnEP/PUR coating system exposed to the cyclic ageing test does not grow through filiform corrosion pattern; instead, a more uniform expansion from the scribe is observed. These findings further highlight the potential limitations of the cyclic ageing test in fully replicating the degradation mechanism observed in the field for the ZnEP/PUR coating system.

5.3.3 Field test versus cyclic ageing test

The final rusted area of EP/PUR and ZnEP/PUR coating systems exposed to the field and the cyclic ageing test are compared in Figure 5.3.5. The results show that the ZnEP/PUR coating provided significantly better protection compared to the EP/PUR coating in the field, as illustrated in Figure 5.3.5a and Figure 5.3.5b. However, in the cyclic ageing test, only a minor improvement in anti-corrosive protection was observed by ZnEP/PUR relative to EP/PUR, as shown in Figure 5.3.5c and Figure 5.3.5d. These findings indicate that a different degradation rate was observed for ZnEP/PUR and EP/PUR coating systems exposed to the field and the cyclic ageing test. Therefore, the reliability of grading different anticorrosive coating systems exposed to the cyclic ageing test, as defined in ISO 12944-9 [90], is questionable in terms of representing the real field performances.

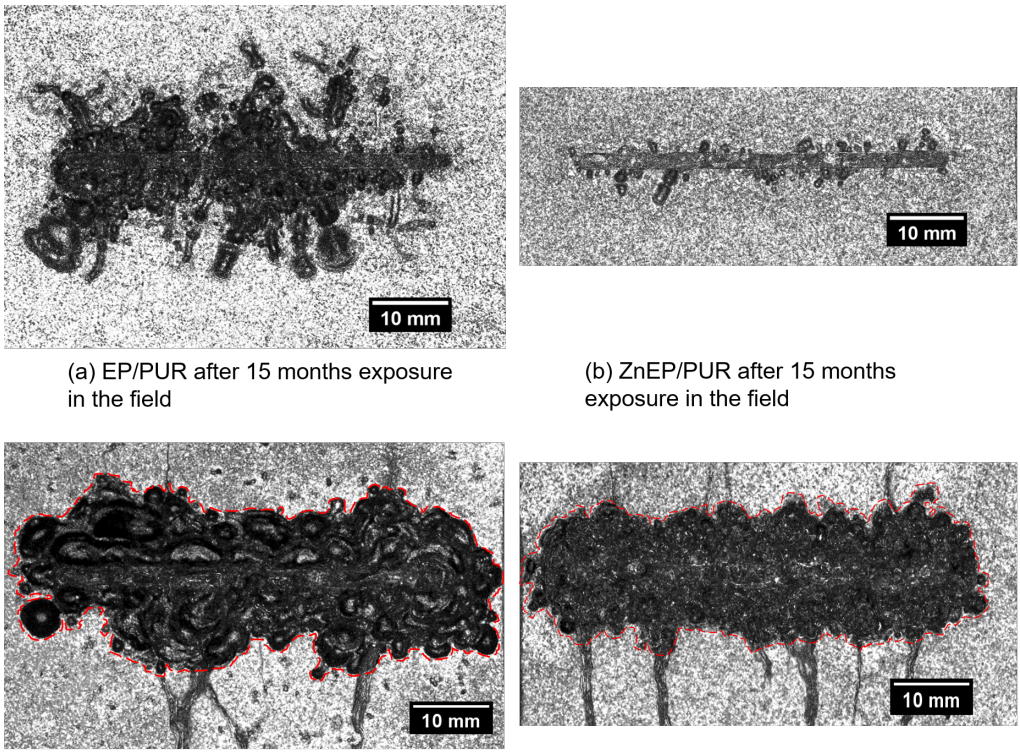

(a) EP/PUR after 15 months exposure in the field

(b) ZnEP/PUR after 15 months exposure in the field

(c) EP/PUR after 25 weeks exposure in the cyclic ageing test

(d) ZnEP/PUR after 25 weeks exposure in the cyclic ageing test

Figure 5.3.5: Comparison of the final rust creep evaluation of EP/PUR and ZnEP/PUR coating systems exposed to the field and the cyclic ageing test, respectively

The rust creep propagation mechanism for EP/PUR and ZnEP/PUR coating systems grew through filiform-like corrosion from the scratching under field exposure, in contrast to the relatively regular rust creep growth that spread slowly from the rust creep boundaries for the same coating systems exposed in the cyclic ageing test. The observed filiform-like corrosion pattern around the scribe on samples exposed to the field is not a unique case. Honda et [16, 99] reported a similar filiform-like corrosion pattern around the scribe on coated steel substrate, which they initiated by spraying 5 wt.% NaCl solution and subjecting the panel to a chamber with a constant temperature of 40 °C and relative humidity of 80 %. Moreover, it has been reported that filiform corrosion is most active at 20-40 °C and relative humidity between 65-95 % for steel [100] with typical a coating thickness on the order of 80-100 μm [13, 14]. In the field exposure, at least two of the activation factors have been fulfilled where the monitored average humidity ranges from 65-87 % and a coating thickness of approximately 100 μm in this study. Even though, the average temperature in the field was monitored to be between 5-20 °C during the exposure period, the filiform-like corrosion still occurred on the steel substrate, indicating that the proposed most active temperature range of 20-40 °C may not be the decisive factor for the activation of filiform corrosion. This is further confirmed in the cyclic ageing test, where the temperature was mostly between 35-60 °C (except for 24 hours at -20 °C), and filiform corrosion activation did not occur. In the cyclic ageing test, the relative humidity remained above 50 % within 62 % of the exposure time, which may indicate a constant humidity of the environment is more essential factor to activate the filiform corrosion.

The results of this study highlight the potential of using SAM technique to study rust creep propagation mechanisms in real-time. This method can provide early detection of rust creep and can serve as a cost-effective alternative to traditional destructive inspection methods, which require replicating samples to collect data points. With traditional methods, the number of replications needed should match the frequency of evaluations, as each sample can only be evaluated once. Additionally, an assumption of all replicated samples would follow the same degree of degradation is needed. However, this assumption can be challenging to fulfil in reality. Real-time evaluation of coated samples not only achieves a kinetic study of the degradation pattern, as shown in Section 5.3.4, but also allows for the prediction of coating lifespan, thereby reducing assessment time. This methodology could also be applied to optimise existing accelerated testing protocols in the laboratory. The immediate evaluation of rust creep propagation after each exposure condition can guide the refinement of the accelerated testing protocols, aiming to achieve a propagation mechanism that closely resembles what is observed in the field, within the shortest possible time frame.

In summary, the ability to monitor rust creep propagation in real-time non-destructively is a valuable tool for both coating performance evaluation and optimisation of accelerated testing protocols.

5.3.4 Kinetics of rust creep propagation

In order to predict the kinetics of the rust creep propagation, the evolution of rust creep propagation of EP/PUR and ZnEP/PUR exposed in the field and the accelerated cyclic ageing test were quantified from SAM coating/steel interface images as a function of exposure time as presented in Figure 5.3.6. The results were fitted with linear regression with an interception at (0.0), which represents the expected zero formation of rust before exposure. All the fittings had a $R^2 \geq 0.97$, indicating that propagation of rust creep is well-described by a linear function for both the field and accelerated cyclic ageing exposures. To quantify rust creep on samples exposed in the cyclic ageing test, the delaminated area around the scribe was determined, as highlighted inside the dashed red lines in Figures 5.3.3 and 5.3.4. This was done to avoid overestimation by including the false rust lines appearing on the SAM coating/steel interface images.

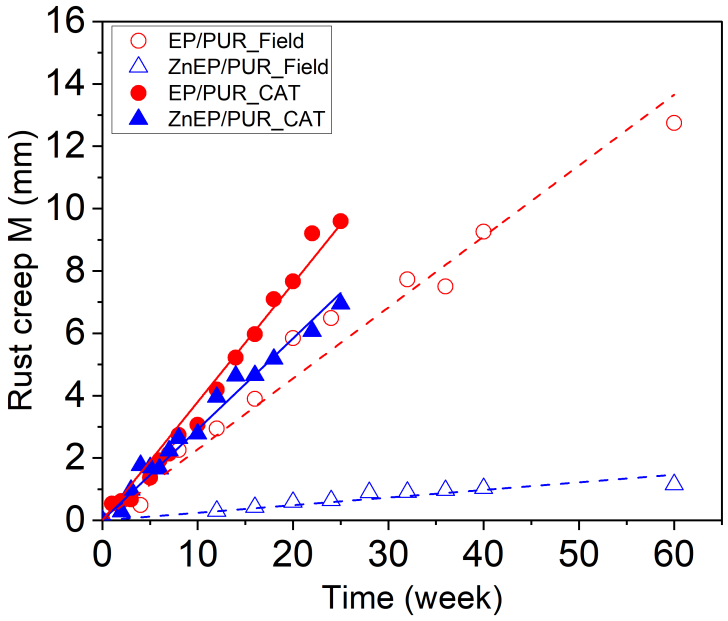

Figure 5.3.6: Linear fitting based on rust creep evolution on EP/PUR and ZnEP/PUR coating systems exposed to the field and cyclic ageing test, respectively.

The rates of rust creep propagation, which were determined by linear fitting of the data, are summarised in Table 5.3.1. The results show that during the field test, the ZnEP/PUR coating system provided 9.5 times better anticorrosive protection around the scribe compared to EP/PUR coating systems based on the determined growth rates of rust creep. This finding is consistent with Knudsen et al [98], who reported that full three-layer coating systems with zinc-rich primer improved corrosion creep resistance by a factor of about 10, as determined based on the final rust creep evaluation of the samples, compared to the epoxy primed coating systems. This suggests that two-layer coating systems with a DFT around 100 µm are capable of capturing the same degree/rate of rust creep growth between zinc-rich primed and epoxy primed systems, as seen in full coating systems.

In contrast, ZnEP/PUR coating system exposed in the cyclic ageing test provided only 1.3 times better rust creep resistance compared to EP/PUR coating system. This raises

concerns about the suitability of using the cyclic ageing test to evaluate the performance of different anti-corrosive coating systems, as the results may not accurately reflect the corrosion resistance benefits provided by the zinc-rich primer in the field test.

Table 5.3.1: Rust creep propagation rates of EP/PUR and ZnEP/PUR coating systems exposed to the field and CAT test, respectively.

No.	Coating system	Exposure	Rust creep rate, v (mm/week)	Efficiency $\frac{v_{EP/PUR}}{v_{ZnEP/PUR}}$	Accelerated factor: $\frac{v_{CAT}}{v_{Field}}$
S77	EP/PUR	Field test	0.228		
S64	ZnEP/PUR	Field test	0.024	9.5	
S72	EP/PUR	CAT test	0.380		1.7
S67	ZnEP/PUR	CAT test	0.292	1.3	12.2

The accelerated factor for EP/PUR and ZnEP/PUR coating systems was determined by dividing the rust creep growth rate in the CAT test by the rust creep growth rate in the field test, resulting in values of 12.2 and 1.7, respectively (Table 5.3.1). The cyclic ageing test was more effective in accelerating the degradation of zinc-rich primed systems and less efficient for epoxy primed systems. However, even with this difference in the accelerated factors, the cyclic ageing test was unable to capture the filiform-like corrosion mechanisms as observed during rust creep expansion under field exposure. These findings further support the fact that the cyclic ageing test generates an overly aggressive environment [98, 101], potentially overlooking the true degradation mechanism. Therefore, field results are still necessary to verify the actual coating performance and the suitability of applied accelerated tests.

Although, the cyclic ageing test may be capable of distinguishing the best coating system performance concerning rust creep corrosion, as evidenced by the results in this study, where ZnEP/PUR coating system outperformed the EP/PUR coating system. However, it is unsuitable for distinguishing the degree of better protection between different anti-corrosive coating technologies, as confirmed by the findings of this study.

5.4 Conclusion

By using non-destructive scanning acoustic microscopy, significantly different degradation mechanisms were observed for EP/PUR and ZnEP/PUR coating systems exposed to the field and the cyclic ageing test, respectively. The following conclusions can be drawn:

1. Non-destructive scanning acoustic microscopy is beneficial for studying coating rust creep propagation because it reveals rust creep propagation mechanism that may be missed by the traditional standardised destructive evaluation method.
2. Rust creep propagates through a filiform-like corrosion mechanism, as observed in the field exposure of both EP/PUR and ZnEP/PUR coating systems.
3. Rust creep propagation of EP/PUR coating system exposed to the cyclic ageing test grows through an asymmetrical pattern from the scribe, while for ZnEP/PUR coating system, the rust creep grows more uniformly from the scribe.
4. The accelerated factor of the ZnEP/PUR coating system in the cyclic ageing test based on the rust creep is 12.2 times compared to the field exposure, while the accelerated factor of the EP/PUR system is 1.7 times. Thus, ranking different anti-corrosive coating systems using the cyclic ageing test may not be reliable.

6 Conclusion

This project aimed to investigate the degradation processes of different commercial coating systems using non-destructive evaluation techniques. The study focused on zinc-rich epoxy primer, epoxy barrier, EP/PUR, and ZnEP/PUR coating systems. Non-destructive methods, such as electrochemical impedance measurements and scanning acoustic microscopy, were primarily employed. The study investigated the degradation of coating barriers and sacrificial protection using electrochemical methods in exposure to neutral salt spray and field conditions. Additionally, the project examined the water uptake mechanisms of epoxy primers during immersion. Non-destructive monitoring of rust creep propagation around the scribe in a two-layer coating system was also conducted, both in cyclic ageing tests and field exposure, and the rust creep propagation rate was proposed.

Electrochemical impedance measurements provided valuable insights into the degradation process of commercial coatings exposed to various environments. For zinc-rich epoxy primers, the evolution profile of the open circuit potential (OCP) was indicative of sacrificial protection duration, while the impedance modulus (|Z|) reflected the barrier properties and overall performance of the coatings. However, it is important to note that the primary protective mechanism of zinc-rich primers is sacrificial protection, and the impedance modulus threshold of $10^6 \Omega \cdot cm^2$ should not be solely relied upon to evaluate their corrosion protection effectiveness.

In contrast, epoxy barrier coatings primarily rely on their barrier properties to prevent the penetration of aggressive species to the coating/substrate interface. The impedance modulus is a suitable parameter to assess the coating performance, with corrosion expected to occur when |Z| falls below $10^6\ \Omega \cdot \text{cm}^2$ for further exposures.

Water uptake measurements, conducted in a 3.5 wt.% NaCl solution, revealed the water uptake behaviour of the epoxy coating systems. Water diffusion into the free film of the epoxy coating followed rapid absorption, a slower continuous uptake rate, and leaching of coating ingredients. In the case of coated steel substrates, water uptake exhibited rapid absorption and a slower continuous uptake rate due to swelling of the applied coating layer. The non-destructive scanning acoustic microscopy technique was successfully applied to detect swelling during water uptake, offering a feasible method for monitoring changes in the coating system without causing damage.

Scanning acoustic microscopy has further proved to be a valuable tool for studying the degradation mechanisms of EP/PUR and ZnEP/PUR coating systems exposed to the field and cyclic ageing test, respectively. It revealed distinct rust creep propagation mechanisms that may be missed by traditional standardised destructive evaluation methods. During field exposure, both coating systems exhibited rust creep through a filiform-like corrosion mechanism, indicating similar degradation processes. However, there were differences in the growth rate of rust creep due to the specific protective mechanisms provided by each coating system.

Furthermore, the cyclic ageing test significantly accelerated the rust creep, with the ZnEP/PUR system experiencing a higher acceleration factor of approximately 12 compared to field

exposure, while the EP/PUR system exhibited an acceleration factor of around 2. The EP/PUR system showed asymmetric rust creep growth originating from the scribe, whereas the ZnEP/PUR system exhibited more uniform growth. Notably, neither of the coating systems demonstrated the filiform corrosion mechanism observed in the field. This highlights the limitations of using the cyclic ageing test alone to rank the performance of different anti-corrosive coating systems, as it may differ significantly from their real-field performance.

In conclusion, non-destructive evaluation techniques (NDTs) have provided valuable insights into the degradation processes of commercial coatings. These techniques have enabled the monitoring of sacrificial protection duration, assessment of barrier properties, detection of water uptake and swelling, and observation of rust creep propagation. The utilisation of non-destructive techniques offers several advantages, including the ability to study coatings in situ and over extended periods, thereby reducing the need for destructive sampling. However, it is essential to consider the limitations and challenges associated with each technique.

Overall, this project contributes to the understanding of coating degradation and provides valuable information for optimizing coating formulations, improving protective performance, and ensuring long-term durability. Furthermore, NDTs can be further applied to optimise existing accelerated tests, aiming to improve their correlation with field exposure. By enhancing the reliability and accuracy of accelerated tests, it becomes possible to better predict the performance of coatings in real-world conditions, leading to more effective coating evaluations and reduced material consumption.

7 Future work

Based on the findings of this project using non-destructive evaluation techniques (NDTs), several future research perspectives and directions can be suggested:

- *Coating Degradation Mechanisms*: The study identified degradation mechanisms such as sacrificial protection, barrier properties, water uptake, and rust creep propagation. Future work can focus on a more detailed analysis of these mechanisms to better understand their underlying processes and factors influencing them. The following improvements can be made based on the results of this study:

    1. To investigate the relationship between the galvanic protection duration of a zinc-rich primer and its dry film thickness, a minimum of three different thicknesses should be examined before drawing a conclusion. The recommended thicknesses for investigation are 50, 100, 150 and 200 µm, respectively. The zinc-rich primer can be exposed to neutral salt spray since it exhibits the same degradation as observed during field exposure when OCP is used as the evaluation factor.

    2. For gravimetry measurements of water uptake in free films, it is recommended to collect and analyse the bulk solution for possible leaching of ingredients from the coating layer. Additionally, monitoring the decrease in ions' concentration in the bulk solution may also be of interest if possible. This allows for the isolation of the total mass gained inside the coating free film due to water molecules.

    3. ATR-FTIR can also be applied to simplified coating systems with known compositions. By combining the ATR-FTIR spectra with gravimetry measurements during immersion, the ATR-FTIR spectra can be used for the quantification of water uptake in thin coating layers. This can be achieved by correlating the mass gain with the intensity of the absorbance. Such an approach expands the application of ATR-FTIR beyond qualitative analysis.

    4. In the SAM technique, when utilizing a higher transducer frequency (»125 MHz), it may be possible to conduct a detailed investigation of defects in the coating layer or to track the water penetration profile along the coating cross-section non-destructively. However, the current equipment's maximum image resolution of 10 µm/pixel makes it impossible to detect water diffusion into the coating layer through cross-sectional assessment.

    5. For field exposure, the evaluation of rust creep frequency in a two-layer coating system with an EP/PUR system (DFT $\approx$ 100 µm) can be conducted every month. However, for ZnEP/PUR, a frequency of every 6 months is deemed sufficient. The same coating systems are recommended for cyclic ageing test exposure, with an evaluation frequency of every 3 weeks for both EP/PUR and ZnEP/PUR coating systems.

- *Development or improvement of coating formulation*: Future work can focus on applying NDTs to continuously evaluate the performance of new coating materials and development of formulations that exhibit enhanced sacrificial protection, barrier properties, and resistance to water uptake and rust creep propagation.
- *Optimisation of accelerated testing*: Future research can focus on establishing a correlation between the results obtained from these techniques in accelerated tests and the long-term field exposure of the coatings. This will help validate the findings of non-destructive evaluation and assess the predictive capability of these techniques. Additionally, efforts can be made to optimise the accelerated testing protocols in order to achieve a higher correlation with field performance.
- *Integration of multiple NDTs*: Combining different non-destructive evaluation techniques can provide a more comprehensive assessment of coating degradation. Future work can explore the integration of techniques such as electrochemical impedance spectroscopy, infrared spectroscopy, and gravimetric analysis to obtain a holistic understanding of coating performance and degradation mechanisms. This can provide a more reliable and accurate evaluation of coating systems.
- *Application of Artificial Intelligence and Machine Learning*: The vast amount of data generated from non-destructive evaluation techniques can be effectively analyzed and interpreted using artificial intelligence and machine learning algorithms. Future research can explore the application of these techniques to develop predictive models for coating performance and degradation prediction. This can facilitate proactive maintenance strategies and enhance the overall durability and performance of coated systems.

Bibliography

[1] Artur Goldschmidt and Hans-Joachim Streitberger. *BASF Handbook on Basic of Coating Technology*. BASF and VINCENTZ, 2017.

[2] Gerharbus et al. Koch. International Measures of Prevention , Application , and Economics of Corrosion Technologies Study. Technical report, 2016.

[3] M. Iannuzzi and G. S. Frankel. The carbon footprint of steel corrosion. *npj Materials Degradation*, 6(1):1–4, 2022.

[4] European Commission. Paris Agreement in 2015. https://climate.ec.europa.eu/eu-action/international-action-climate-change/climate-negotiations/paris-agreement_en. (accessed on 26-04-2023).

[5] Aziz Rezig, Tinh Nguyen, David Martin, Lipiin Sung, Xiaohong Gu, Joan Jasmin, and Jonathan W. Martin. Relationship between chemical degradation and thickness loss of an amine-cured epoxy coating exposed to different UV environments. *Journal of Coatings Technology and Research*, 3(3):173–184, 2006.

[6] Hong Qi Yang, Qi Zhang, San Shan Tu, You Wang, Yi Min Li, and Yi Huang. A study on effects of elastic stress on protective properties of marine coatings on mild steel in artificial seawater. *Progress in Organic Coatings*, 99:61–71, 2016.

[7] Branko N. Popov. Organic coatings. In *Organic coatings*, chapter 13, pages 558–579. Elsevier B.V., 2015.

[8] Claus E Weinell and Soeren Nyborg Rasmussen. Non-destructive determination of rust creep. *NACE - International Corrosion Conference Series*, (08004):1–10, 2008.

[9] Chao Wei, George Wang, Marcus Cridland, David L. Olson, and Stephen Liu. Corrosion protection of ships. In *Handbook of Environmental Degradation Of Materials: Third Edition*, pages 533–557. Elsevier Inc., third edition, 2018.

[10] P. A. Sørensen, S. Kiil, K. Dam-Johansen, and C. E. Weinell. Anticorrosive coatings: A review. *Journal of Coatings Technology and Research*, 6(2):135–176, 2009.

[11] Jyoti Bhandari, Faisal Khan, Rouzbeh Abbassi, Vikram Garaniya, and Roberto Ojeda. Modelling of pitting corrosion in marine and offshore steel structures - A technical review. *Journal of Loss Prevention in the Process Industries*, 37:39–62, 2015.

[12] Corrosionpedia Staff. Galvanic Corrosion. https://www.corrosionpedia.com/an-introduction-to-the-galvanic-series-galvanic-compatibility-and-corrosion/2/1403 (accessed on 29-03-2023), 2020.

[13] Christian Vargel. Filiform corrosion. In *Corrosion of Aluminium*, chapter Filiform c, pages 247–265. Elsevier Ltd, 2020.

[14] Branko N. Popov. Pitting and Crevice Corrosion. In *Corrosion Engineering*, chapter 7, pages 289–325. Elsevier B.V., 2015.

[15] Andrej Nazarov and Dominique Thierry. Application of Scanning Kelvin Probe in the Study of Protective Paints. 6(August):1–17, 2019.

[16] Kazuhiko Honda, Akira Usami, and Hiromasa Nomura. Potential distribution measurement of under-film corrosion by scanning Kelvin probe. *Zairyo to Kankyo/ Corrosion Engineering*, 47(6):403–405, 1998.

[17] Qixin Zhou and Yechun Wang. Comparisons of clear coating degradation in NaCl solution and pure water. *Progress in Organic Coatings*, 76(11):1674–1682, 2013.

[18] Kenichiro Imafuku. Steel construction today & tomorrow. *The Japan Iron and Steel Federation & Japansese Society of Steel Construction*, page 5, 2016.

[19] Ainara López-Ortega, Raquel Bayón, and José Luís Arana. Evaluation of protective coatings for high-corrosivity category atmospheres in offshore applications. *Materials*, 12(8), 2019.

[20] P. A. Sørensen, S. Kiil, K. Dam-Johansen, and C. E. Weinell. Anticorrosive coatings: A review. *Journal of Coatings Technology and Research*, 6(2):135–176, 2009.

[21] P. A. Sørensen, K. Dam-Johansen, C. E. Weinell, and S. Kiil. Cathodic delamination of seawater-immersed anticorrosive coatings: Mapping of parameters affecting the rate. *Progress in Organic Coatings*, 68(4):283–292, 2010.

[22] Rudolph G. Buchheit. *Corrosion resistant coatings and paints*. Elsevier Inc., third edit edition, 2018.

[23] Zoi Lamprakou, Huichao Bi, Claus Erik Weinell, Silvia Tortajada, and Kim Dam-Johansen. Smart epoxy coating with mesoporous silica nanoparticles loaded with calcium phosphate for corrosion protection. *Progress in Organic Coatings*, 165(January):106740, 2022.

[24] Tatyana Nesterova, Kim Dam-Johansen, and Søren Kiil. Synthesis of durable microcapsules for self-healing anticorrosive coatings: A comparison of selected methods. *Progress in Organic Coatings*, 70(4):342–352, 2011.

[25] Amin Vedadi, Xinnan Wang, M. Subbir Parvej, Quan Yuan, Fardad Azarmi, Dante Battocchi, Zhibin Lin, and Yechun Wang. Degradation of epoxy coatings exposed to impingement flow. *Journal of Coatings Technology and Research*, 18(4):1153–1164, 2021.

[26] Fandi Meng, Li Liu, Yu Cui, and Fuhui Wang. Evaluation of coating resistivity for pigmented/unpigmented epoxy coatings under marine alternating hydrostatic pressure. *Journal of Materials Science and Technology*, 64:165–175, 2021.

[27] J. Edward Singley. Principles of Corrosion. *Proceedings - AWWA Water Quality Technology Conference*, pages 319–329, 1982.

[28] H. Oehler, I. Alig, D. Lellinger, and M. Bargmann. Failure modes in organic

coatings studied by scanning acoustic microscopy. *Progress in Organic Coatings*, 74(4):719–725, 2012.

[29] Jean Baptiste Jorcin, Emmanuel Aragon, Céline Merlatti, and Nadine Pébère. Delaminated areas beneath organic coating: A local electrochemical impedance approach. *Corrosion Science*, 48(7):1779–1790, 2006.

[30] Changfeng Fan, Jianmin Shi, and Klaus Dilger. Water uptake and interfacial delamination of an epoxy-coated galvanized steel: An electrochemical impedance spectroscopic study. *Progress in Organic Coatings*, 137(September):105333, 2019.

[31] R. C.L. Tai and Z. Szklarska-Smialowska. Effect of fillers on the degradation of automotive epoxy adhesives in aqueous solutions - Part II The microhardness change and delamination of automotive epoxy adhesives in distilled water and NaCl solutions. *Journal of Materials Science*, 28(22):6205–6210, 1993.

[32] Mark E. Nichols. Paint weathering tests. In *Handbook of Environmental Degradation Of Materials: Third Edition*, pages 51–67. Elsevier Inc., third edit edition, 2018.

[33] B. Fitzsimons and T. Parry. Paint and coating failures and defects. *Shreir's Corrosion*, pages 2728–2745, 2010.

[34] P. A. Sørensen, K. Dam-Johansen, C. E. Weinell, and S. Kiil. Cathodic delamination: Quantification of ionic transport rates along coating-steel interfaces. *Progress in Organic Coatings*, 68(1-2):70–78, 2010.

[35] M. H. Nazir, Z. A. Khan, and K. Stokes. A holistic mathematical modelling and simulation for cathodic delamination mechanism - A novel and an efficient approach. *Journal of Adhesion Science and Technology*, 29(22):2475–2513, 2015.

[36] M. H. Nazir, Z. A. Khan, A. Saeed, and K. Stokes. A model for cathodic blister growth in coating degradation using mesomechanics approach. *Materials and Corrosion*, 67(5):495–503, 2016.

[37] Ole Knudsen, Unni Steinsmo, Marit Bjordal, and Sarbjyot Nijjer. Accelerated Testing : and Five Years of Offshore Field Testing. *Jpcl*, (May):52–56, 2001.

[38] F. X. Perrin, C. Merlatti, E. Aragon, and A. Margaillan. Degradation study of polymer coating: Improvement in coating weatherability testing and coating failure prediction. *Progress in Organic Coatings*, 64(4):466–473, 2009.

[39] Assured Testing. ASTM G85 Annex 5: Prohesion Testing. https://www.assuredtesting.com/astm-g85-annex-5-prohesion (accessed on 26-04-2023).

[40] Accelerated Test. Evaluation of the Long-Term Performance of Marine and Offshore Coatings System Exposed on a Traditional Stationary Site and an Operating Ship and Its Correlation to Accelerated Test. *Coatings*, 12:1758, 2022.

[41] F. Deflorian, S. Rossi, and M. Fedel. Organic coatings degradation: Comparison between natural and artificial weathering. *Corrosion Science*, 50(8):2360–2366, 2008.

[42] Franky E. Bedoya, Ángela Bermúdez, Juan G. Castaño, Félix Echeverría, and Jorge A. Calderón. Electrochemical impedance study for modeling the anticorrosive performance of coatings based on accelerated tests and outdoor exposures. *Journal of Coatings Technology and Research*, 13(5):895–904, 2016.

[43] Xiaohong Gu, Debbie Stanley, Walter E. Byrd, Brian Dickens, Iliana Vaca-Trigo, William Q. Meeker, Tinh Nguyen, Joannie W. Chin, and Jonathan W. Martin. Linking accelerated laboratory test with outdoor performance results for a model epoxy coating system. *Service Life Prediction of Polymeric Materials: Global Perspectives*, pages 3–28, 2009.

[44] M. Estefanía Angeles, Francisco Rodríguez, and Carlos Magaña. Effect of heating on the performance of anticorrosive coatings. *Pigment and Resin Technology*, 41(1):42–48, 2012.

[45] A. S.L. Castela, A. M. Simões, and M. G.S. Ferreira. E.I.S. evaluation of attached and free polymer films. *Progress in Organic Coatings*, 38(1):1–7, 2000.

[46] Antao Xu, Fan Zhang, Bing Luo, F. Jin, and Tianru Zhang. Investigation the deterioration process of organic coating using changing rate of phase angle at high frequency united to neural network. *International Journal of Electrochemical Science*, 8(1):773–779, 2013.

[47] Fuller Thomas and Harb John. Electroanalytical Techniques and Analysis of Electrochemical Systems. *Electrochemical Engineering*, pages 113–150, 2018.

[48] Hernández J.M. Hernández Héctor Herrera, Reynoso Adriana M. Ruiz, González Juan C. Trinidad, Morán Carlos O. González, Hernández José G. Miranda, Ruiz Araceli Mandujano, Hernández Jorge Morales, Ruiz A.M. and Cruz Ricardo Orozco. Electrochemical Impedance Spectroscopy (EIS): A Review Study of Basic Aspects of the Corrosion Mechanism Applied to Steels. *Intech*, 32(tourism):137–144, 2020.

[49] Jean Baptiste Jorcin, Mark E. Orazem, Nadine Pébère, and Bernard Tribollet. CPE analysis by local electrochemical impedance spectroscopy. *Electrochimica Acta*, 51(8-9):1473–1479, 2006.

[50] David Loveday, Pete Peterspm, and Bob Rodgers. Evalution of organic coatings with electrochemical impedance spectroscopy part 2: Application of EIS to coatings. *CoatingsTech*, 1(10):88–93, 2004.

[51] I. Alig, M. Bargmann, H. Oehler, D. Lellinger, M. Wanner, and D. Koch. Investigation of delamination mechanisms in polymer coatings by scanning acoustic microscopy. *Journal of Physics D: Applied Physics*, 44(3), 2011.

[52] V. Guillaumin and D. Landolt. Effect of dispersion agent on the degradation of a water borne paint on steel studied by scanning acoustic microscopy and impedance. *Corrosion Science*, 44(1):179–189, 2002.

[53] Huichao Bi and John Sykes. Cathodic delamination of unpigmented and pigmented epoxy coatings from mild steel. *Progress in Organic Coatings*, 90:114–125, 2016.

[54] Yao Qiu. Encapsulated Microcircuits Using Scanning Acoustic Microscope. 2017.

[55] B. Reddy and J. M. Sykes. Degradation of organic coatings in a corrosive environment: A study by scanning Kelvin probe and scanning acoustic microscope. *Progress in Organic Coatings*, 52(4):280–287, 2005.

[56] Hyunung Yu. Scanning acoustic microscopy for material evaluation. *Applied Microscopy*, 50(1), 2020.

[57] Andrei S. Dukhin and Philip J. Goetz. Fundamentals of acoustics in homogeneous liquids: Longitudinal rheology. In *Studies in Interface Science*, volume 24, pages 91–125. 2010.

[58] Andressa Trentin, Amirhossein Pakseresht, Alicia Duran, Yolanda Castro, and Dušan Galusek. Electrochemical Characterization of Polymeric Coatings for Corrosion Protection: A Review of Advances and Perspectives. *Polymers*, 14(12):1–28, 2022.

[59] Morten L. Pedersen, Burak Ulusoy, Claus E. Weinell, Frederikke B. Zilstorff, Songgeng Li, and Kim Dam-Johansen. CoaST Maritime Test Centre: an investigation of biofouling propensity. *Journal of Coatings Technology and Research*, 2023.

[60] Elsadig O. Eltai, J. D. Scantlebury, and E. V. Koroleva. Protective properties of intact unpigmented epoxy coated mild steel under cathodic protection. *Progress in Organic Coatings*, 73(1):8–13, 2012.

[61] Farhad Tohidi Shirehjini, Iman Danaee, Hadi Eskandari, and Davood Zarei. Effect of Nano Clay on Corrosion Protection of Zinc-rich Epoxy Coatings on Steel 37. *Journal of Materials Science and Technology*, 32(11):1152–1160, 2016.

[62] J. H.W. de Wit, D. H. van der Weijde, and G. Ferrari. Organic coatings. *Corrosion Mechanisms in Theory and Practice: Third Edition*, pages 863–906, 2011.

[63] Hong Qi Yang, Qi Zhang, Yi Min Li, Gang Liu, and Yi Huang. Effects of Immersion Temperature on the Performance of a Marine Epoxy-Based Organic Coating for Ballast Tanks. *Journal of Materials Engineering and Performance*, 30(6):4458–4465, 2021.

[64] Chengfei Zhu, Rui Xie, Jinhua Xue, and Linlin Song. Studies of the impedance models and water transport behaviors of cathodically polarized coating. *Electrochimica Acta*, 56(16):5828–5835, 2011.

[65] P. A.J. Donkers, H. P. Huinink, S. J.F. Erich, N. J.W. Reuvers, and O. C.G. Adan. Water permeability of pigmented waterborne coatings. *Progress in Organic Coatings*, 76(1):60–69, 2013.

[66] H. Oehler, I. Alig, D. Lellinger, and M. Bargmann. Failure modes in organic coatings studied by scanning acoustic microscopy. *Progress in Organic Coatings*, 74(4):719–725, 2012.

[67] A. Miszczyk and K. Darowicki. Water uptake in protective organic coatings and its reflection in measured coating impedance. *Progress in Organic Coatings*, 124(August 2017):296–302, 2018.

[68] C. Vosgien Lacombre, G. Bouvet, D. Trinh, S. Mallarino, and S. Touzain. Water uptake in free films and coatings using the Brasher and Kingsbury equation: a possible explanation of the different values obtained by electrochemical Impedance spectroscopy and gravimetry. *Electrochimica Acta*, 231:162–170, 2017.

[69] C. Vosgien Lacombre, G. Bouvet, D. Trinh, S. Mallarino, and S. Touzain. Effect of pigment and temperature onto swelling and water uptake during organic coating ageing. *Progress in Organic Coatings*, 124(November 2017):249–255, 2018.

[70] X. Yuan, Z. F. Yue, X. Chen, S. F. Wen, L. Li, and T. Feng. EIS study of effective capacitance and water uptake behaviors of silicone-epoxy hybrid coatings on mild steel. *Progress in Organic Coatings*, 86:41–48, 2015.

[71] Franky Esteban Bedoya-Lora, Félix Echeverría, and Jorge Andrés Calderón. Effectiveness of non-Fickian diffusion model on the water uptake determination of different organic coatings. *Progress in Organic Coatings*, 136(June):105206, 2019.

[72] S. Duval, M. Keddam, M. Sfaira, A. Srhiri, and H. Takenouti. Electrochemical Impedance Spectroscopy of Epoxy-Vinyl Coating in Aqueous Medium Analyzed by Dipolar Relaxation of Polymer. *Journal of The Electrochemical Society*, 149(11):B520, 2002.

[73] A. S. Castela and A. M. Simões. Water sorption in freestanding PVC films by capacitance measurements. *Progress in Organic Coatings*, 46(2):130–134, 2003.

[74] Weilong Zhang and Mark R. Jaworowski. In situ capacitance measurements for in-plane water vapor transport in paint films. *Progress in Organic Coatings*, 74(3):534–539, 2012.

[75] C. Vosgien Lacombre, G. Bouvet, D. Trinh, S. Mallarino, and S. Touzain. Effect of pigment and temperature onto swelling and water uptake during organic coating ageing. *Progress in Organic Coatings*, 124(September):249–255, 2018.

[76] G.L. Yu, T.R. and Ji. *Electrochemical Methods in Soil and Water Research*. Pergamon Press, 1993.

[77] G. J. Brug, A. L.G. van den Eeden, M. Sluyters-Rehbach, and J. H. Sluyters. The analysis of electrode impedances complicated by the presence of a constant phase element. *Journal of Electroanalytical Chemistry*, 176(1-2):275–295, 1984.

[78] D.M; Kingsbury and A.H. Brasher. Electrical Measurements in the study of immersed paint coating on metal. I. Comparison between capacitance and gravimetric methods of estimating water-uptake. *J.appl.Chem*, 4:62–72, 1954.

[79] Mohammad Naser Kakaei, Jaber Neshati, and Ali Reza Rezaierod. On the Extraction of the Effective Capacitance from Constant Phase Element Parameters. *Protection of Metals and Physical Chemistry of Surfaces*, 54(3):548–556, 2018.

[80] C. H. Hsu and F. Mansfeld. Concernng the conversion of the constant phase element parameter Y0 into a capacitance. *Corrosion*, 57(9):747–748, 2001.

[81] Bryan Hirschorn, Mark E Orazem, Bernard Tribollet, Vincent Vivier, Isabelle Frateur, and Marco Musiani. Electrochimica Acta Determination of effective

capacitance and film thickness from constant-phase-element parameters. *Electrochimica Acta*, 55(21):6218–6227, 2010.

[82] Pierre Bonin, Aurélien Roggero, Nicolas Caussé, Nadine Pébère, Dominique Thierry, and Nathalie Le Bozec. Impedance analysis of the barrier effect of coil-coated materials: Water uptake and glass transition variations. *Progress in Organic Coatings*, 153(September 2020):1–9, 2021.

[83] Aurélien Roggero, Laura Villareal, Nicolas Caussé, Audrey Santos, and Nadine Pébère. Correlation between the physical structure of a commercially formulated epoxy paint and its electrochemical impedance response. *Progress in Organic Coatings*, 146(January):105729, 2020.

[84] A. S. Castela and A. M. Simoes. An impedance model for the estimation of water absorption in organic coatings. Part I: A linear dielectric mixture equation. *Corrosion Science*, 45(8):1631–1646, 2003.

[85] Peeter Laurson, Piret Raudsepp, Hedi Kaldmäe, Ave Kikas, and Uno Mäeorg. The deconvolution of FTIR-ATR spectra to five Gaussians for detection of small changes in plant-water clusters. *AIP Advances*, 10(8), 2020.

[86] P. Musto, G. Ragosta, and L. Mascia. Vibrational spectroscopy evidence for the dual nature of water sorbed into epoxy resins. *Chemistry of Materials*, 12(5):1331–1341, 2000.

[87] María González González, Juan Carlos Cabanelas, and Juan Baselga. Applications of FTIR on Epoxy Resins - Identification, Monitoring the Curing Process, Phase Separation and Water Uptake. *Infrared Spectroscopy - Materials Science, Engineering and Technology*, 2, 2012.

[88] Negin Madelat, Benny Wouters, Ehsan Jalilian, Guy Van Assche, Annick Hubin, Herman Terryn, and Tom Hauffman. Differentiating between the diffusion of water and ions from aqueous electrolytes in organic coatings using an integrated spectro-electrochemical technique. *Corrosion Science*, 212(September 2022):110919, 2023.

[89] N. Fredj, S. Cohendoz, S. Mallarino, X. Feaugas, and S. Touzain. Evidencing antagonist effects of water uptake and leaching processes in marine organic coatings by gravimetry and EIS. *Progress in Organic Coatings*, 67(3):287–295, 2010.

[90] ISO12944-9. Structures, Paints and varnishes- Corrosion protection of steel structures by protective paintsystem- Part 9: Protective paint systems and laboratory performance test methods for offshore and related. Technical report, 2018.

[91] Huichao Bi, Claus Erik Weinell, Raquel Agudo de Pablo, Benjamín Santos Varela, Sergio González Carro, Álvaro Rodríguez Ruiz, and Kim Dam-Johansen. Rust creep assessment—A comparison between a destructive method according to ISO 12944 and selected non-destructive methods. *Progress in Organic Coatings*, 157(April), 2021.

[92] Ingo Alig, Sascha Tadjbach, Peter Krüger, Harald Oehler, and Dirk Lellinger. Characterization of coating systems by scanning acoustic microscopy: Debonding, blistering and surface topology. *Progress in Organic Coatings*, 64(2-3):112–119, 2009.

[93] ISO8501-1. Preparation of steel substrates before application of paints and related products ? Visual assessment of surface cleanliness ? Part 1: Rust grades and preparation grades of uncoated steel substrates and of steel substrates after overall removal of previou. Technical report, 2017.

[94] Tomislav Šolić, Dejan Marić, Ivan Peko, and Ivan Samardžić. Influence of Anticorrosive Pigment, Dry-Film Thickness and Conditioning Time on Protective Properties of Two-Component Epoxy Primer. *Materials*, 15(9), 2022.

[95] Francesco Bertocci, Andrea Grandoni, and Tatjana Djuric-Rissner. Scanning acoustic microscopy (SAM): A robust method for defect detection during the manufacturing process of ultrasound probes for medical imaging. *Sensors (Switzerland)*, 19(22):1–19, 2019.

[96] Håkon Leth-Olsen, Andreas Afseth, and Kemal Nisancioglu. Filiform corrosion of aluminium sheet. II. Electrochemical and corrosion behaviour of bare substrates. *Corrosion Science*, 40(7):1195–1214, 1998.

[97] F. Vacandio, Y. Massiani, P. Gravier, S. Rossi, P. L. Bonora, and L. Fedrizzi. New knowledge on localized corrosion obtained from local measuring techniques. *Electrochimica Acta*, 46(24-25):3641–3650, 2001.

[98] O. Knudsen, A. W.B. Skilbred, A. Løken, B. Daneshian, and D. Höche. Correlations between standard accelerated tests for protective organic coatings and field performance. *Materials Today Communications*, 31(May), 2022.

[99] Branko N. Popov. Evaluation of Corrosion. In *Corrosion Engineering*, pages 1–28. 2015.

[100] Fabian Brau, Stephanie Thouvenel-Romans, Oliver Steinbock, Silvana S.S. Cardoso, and Julyan H.E. Cartwright. Filiform corrosion as a pressure-driven delamination process. *Soft Matter*, 15(4):803–812, 2019.

[101] Tongzhai Gao, Zhouying He, Lloyd H. Hihara, Hamideh Shokouhi Mehr, and Mark D. Soucek. Outdoor exposure and accelerated weathering of polyurethane/polysiloxane hybrid coatings. *Progress in Organic Coatings*, 130(January):44–57, 2019.

A Appendix A

A.1 EIS evaluation of zinc rich primer

A.1.1 Replications of zinc rich primer exposed to neutral salt spray

A.1.1.1 Replications of OCP data

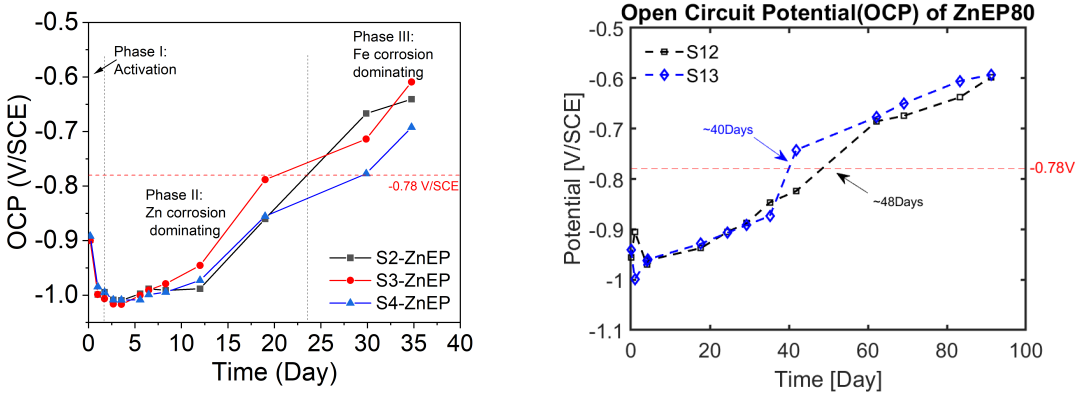

(a) ZnEP 50µm (b) ZnEP 80µm

Figure A.1.1: OCP profiles of zinc rich primer replications exposed to the neutral salt spray.

A.1.2 Replications of zinc rich primer exposed to field

A.1.2.1 Replications of OCP data

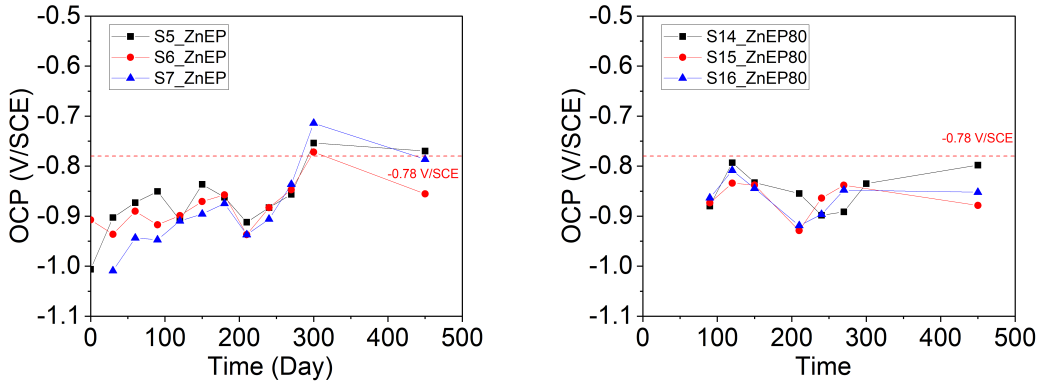

(a) ZnEP with NDTF=50µm (b) ZnEP with NDTF=80µm

Figure A.1.2: Sample replication for OCP profiles of ZnEP coating system with DFTs of (a) $50\mu m$, and (b) $80\mu m$ exposed to the field.

A.2 Replication of epoxy primer exposed to neutral salt spray

A.2.1 Epoxy primer with 50µm

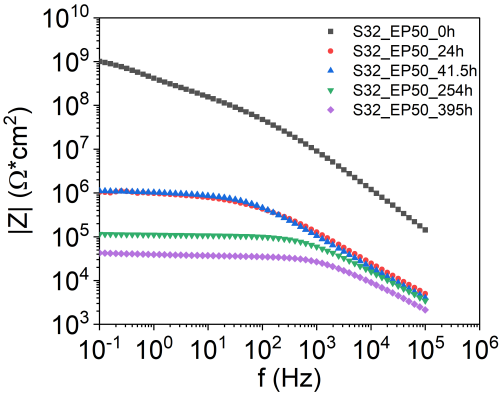

(a) Bode plot of EP50 µm S32

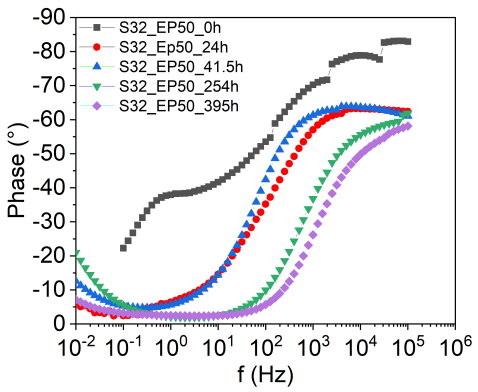

(b) Phase shift of EP50 S32µm

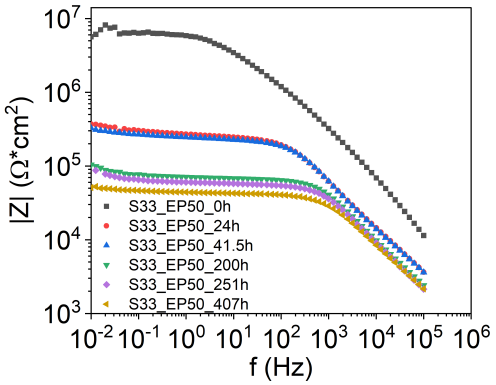

(c) Bode plot of EP50 µm S33

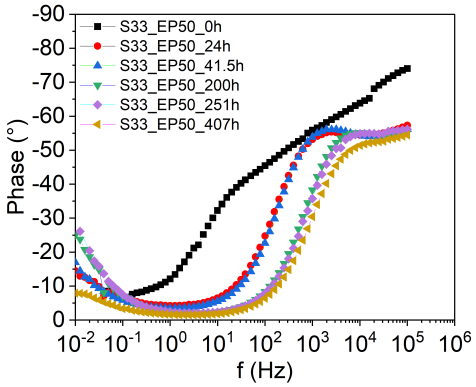

(d) Phase shift of EP50 µm S33

Figure A.2.1: EIS data of epoxy primer exposed to neutral salt spray (a) S32 Bode plot of EP50 µm, (b) S32 Phase shift of EP50 µm, (c) S33 Bode plot of EP50 µm, and (d) S33 Phase shift of EP50 µm. The discontinuities and jumps of the phase shift plot at 0 hour of exposure time is caused by the wire connected to the steel sample (insufficient sample design).

A.2.2 Epoxy primer with 80 µm

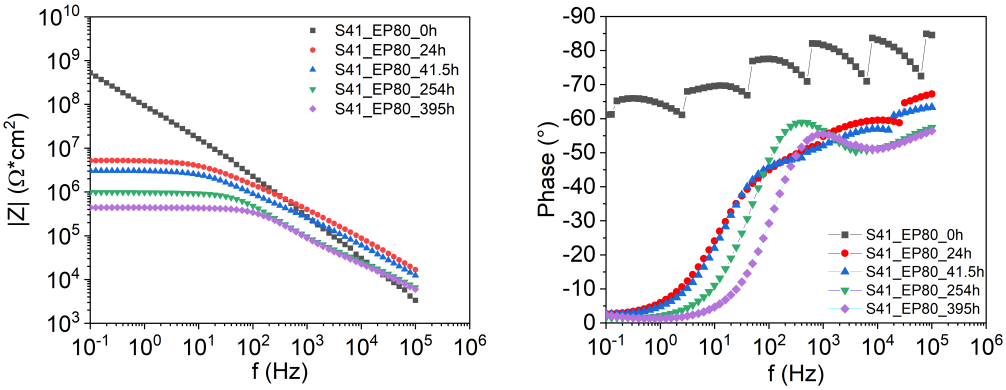

(a) Bode plot of EP80 µm S41

(b) Phase shift of EP80 µm S41

Figure A.2.2: EIS data of epoxy primer exposed to neutral salt spray (a) S41 Bode plot of EP80 µm, (b) S41 Phase shift of EP80 µm. The discontinuities and jumps of the phase shift plot at 0 hour of exposure time is caused by the wire connected to the steel sample (insufficient sample design).

A.3 Replication of epoxy primer exposed to the field

A.3.1 Epoxy primer with 50 µm

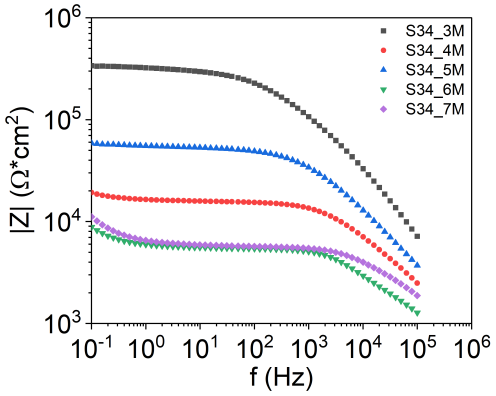

(a) Bode plot of EP50 µm S34

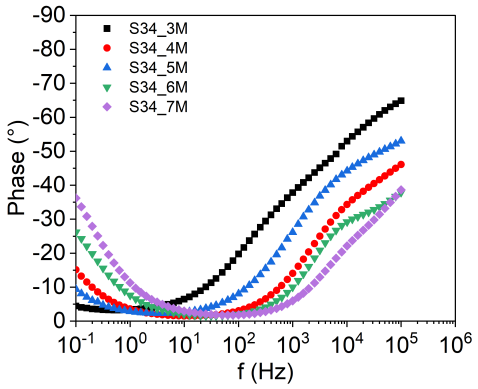

(b) Phase shift of EP50 S34µm

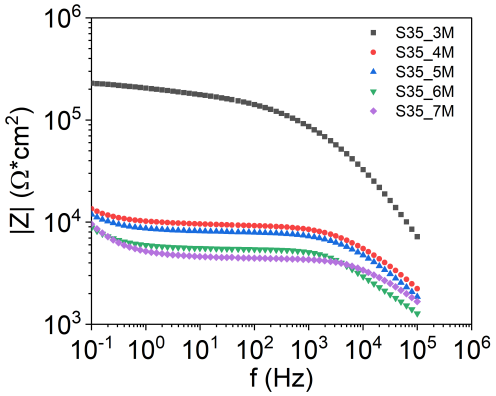

(c) Bode plot of EP50 µm S35

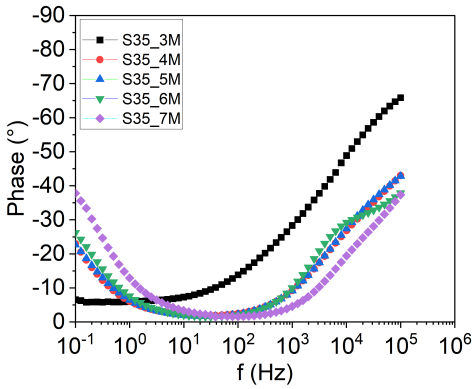

(d) Phase shift of EP50 µm S35

Figure A.3.1: EIS data of epoxy primer exposed to the field (a) S34 Bode plot of EP50 µm, (b) S34 Phase shift of EP50 µm, (c) S35 Bode plot of EP50 µm, and (d) S35 Phase shift of EP50 µm.

A.3.2 Epoxy primer with 80 µm

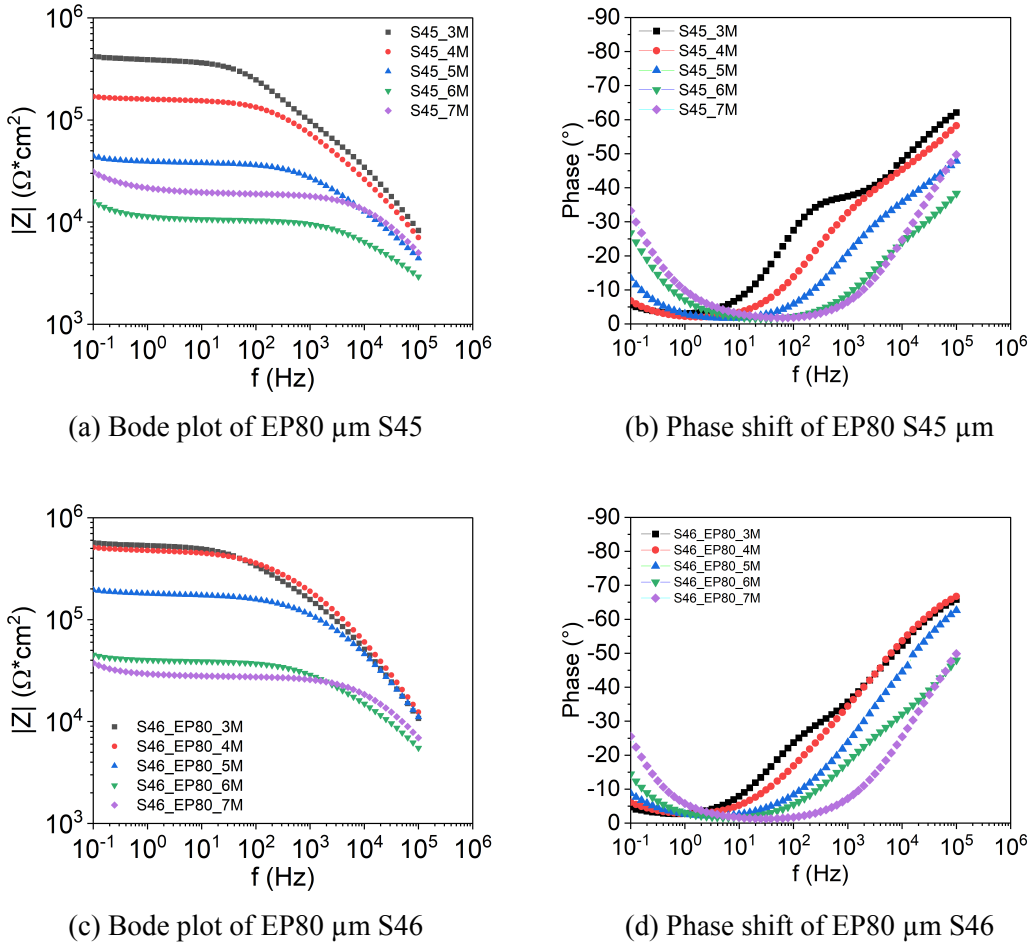

(a) Bode plot of EP80 µm S45

(b) Phase shift of EP80 S45 µm

(c) Bode plot of EP80 µm S46

(d) Phase shift of EP80 µm S46

Figure A.3.2: EIS data of epoxy primer exposed to the field (a) S45 Bode plot of EP80 µm, (b) S45 Phase shift of EP80 µm, (c) S46 Bode plot of EP80 µm, and (d) S46 Phase shift of EP80 µm.

A.3.3 Optical images of epoxy primer exposed to the field

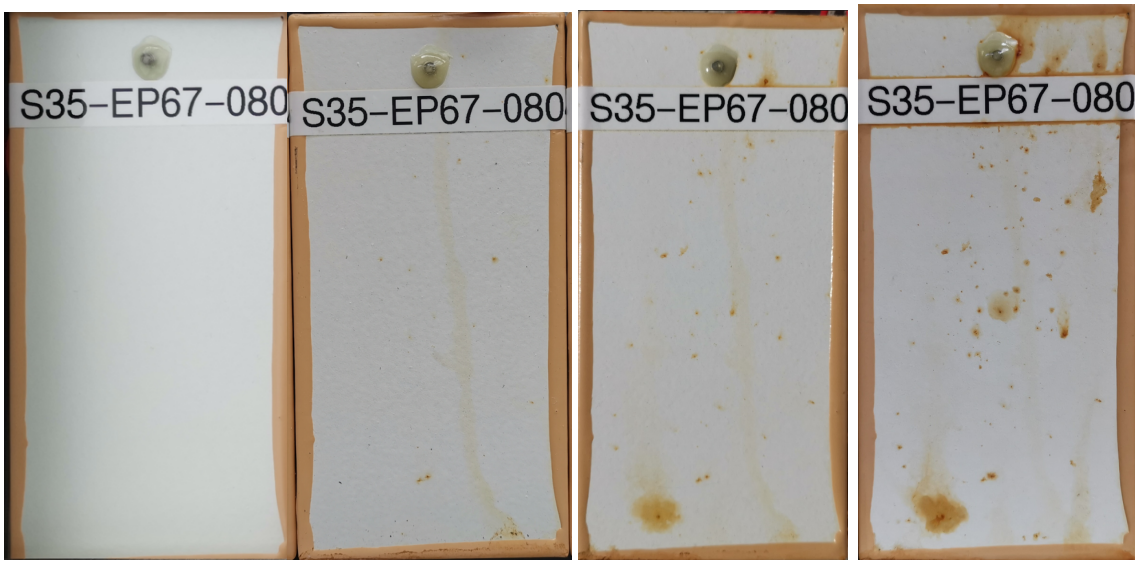

(a) S35 0h (b) S35 1 month (c) S35 2 months (d) S35 3 months

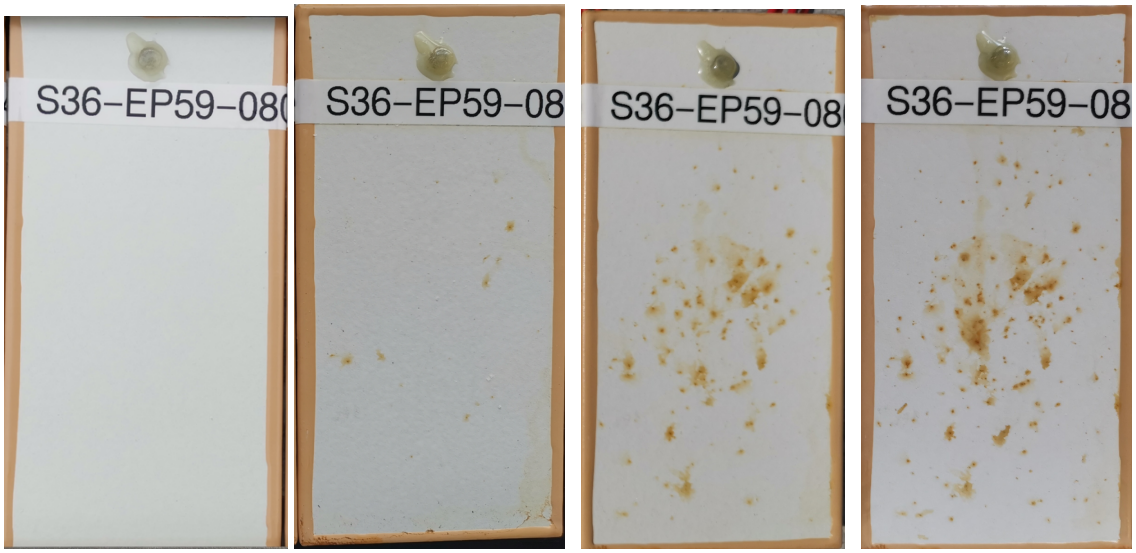

(e) S36 0h (f) S36 1 month (g) S36 2 months (h) S36 3 months

Figure A.3.3: Optical images of S35 (50 µm) and S36 (50 µm) after 0, 1, 2, 3 months exposure in the field.

(a) S45 0h (b) S45 1 month (c) S45 2 months (d) S45 3 months

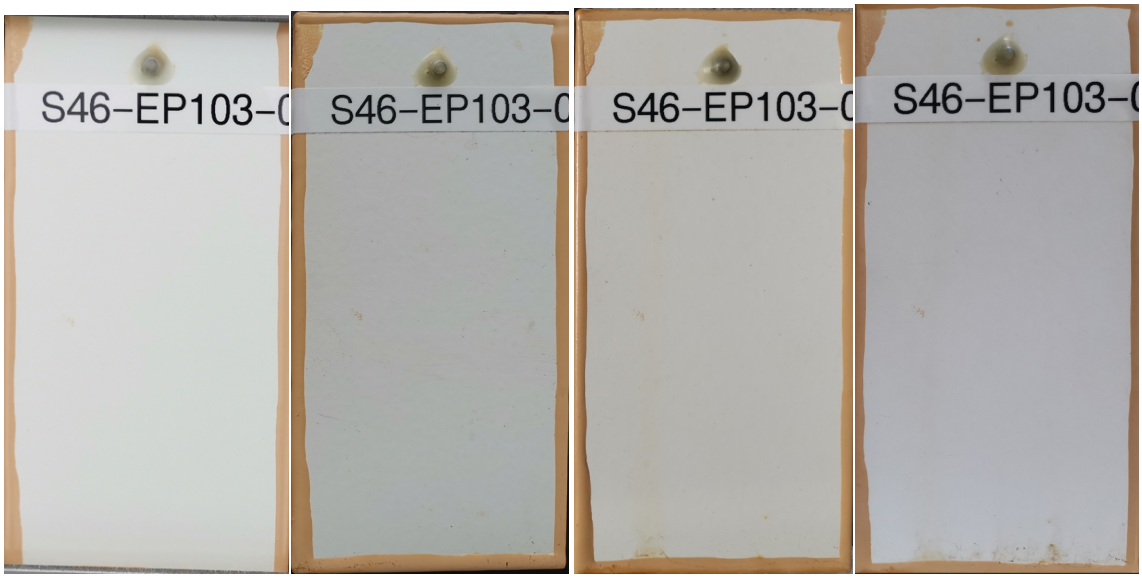

(e) S46 0h (f) S46 1 month (g) S46 2 months (h) S46 3 months

Figure A.3.4: Optical images of S45 (80 µm) and S46 (80 µm) after 0, 1, 2, 3 months exposure in the field.

B Appendix B

B.1 Four electrodes cell for EIS of free film

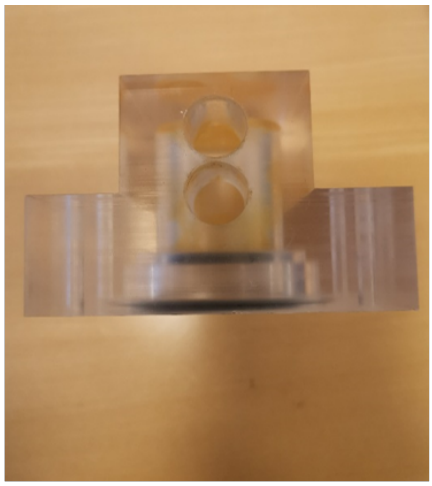

(a) A half cell top-view

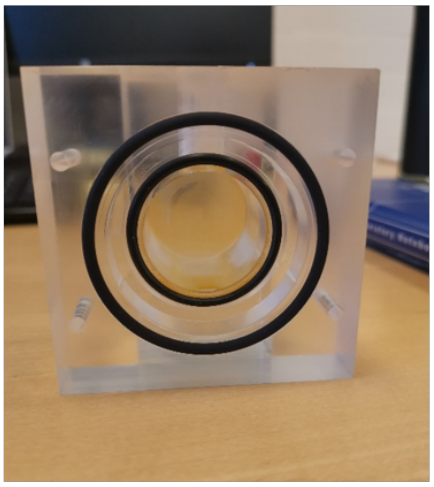

(b) A half cell side-view

(c) A full (two merged half cells) cell top-view

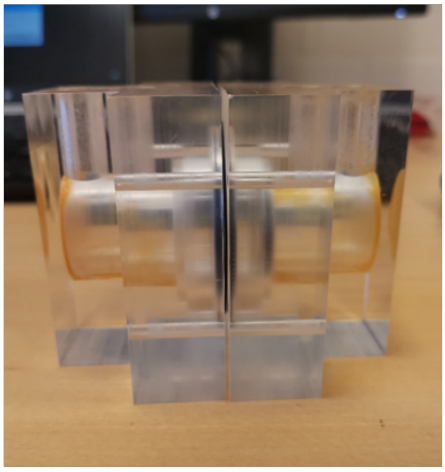

(d) A full cell side-view

Figure B.1.1: Pictures of the cell applied for four-electrode configuration for EIS measurement of free films.

B.2 Commercial coating EP-01 density determination

Three EP-01 free films are produced with dimensions 4 cm x 5cm and an averaged thickness of 100 µm. The density of the dry EP-01 coating is determined as:

$$\rho_{coating} = \frac{m}{V}$$

where $\rho_{coating}$ is the density of the coating $\left(\frac{kg}{m^3}\right)$, m is the mass of free film (kg) and V (m^3) is the volume of free film. The following is the density determined from three free films:

$$\rho_{freefilm_1} = \frac{462.1 \cdot 10^{-6}\text{kg}}{(4 \cdot 10^{-2} \cdot 5 \cdot 10^{-2} \cdot 100 \cdot 10^{-6})\,\text{m}^2} = 2310\frac{\text{kg}}{\text{m}^3}$$
$$\rho_{freefilm_2} = \frac{452.2 \cdot 10^{-6}\text{kg}}{(4 \cdot 10^{-2} \cdot 5 \cdot 10^{-2} \cdot 100 \cdot 10^{-6})\,\text{m}^2} = 2261\frac{\text{kg}}{\text{m}^3}$$
$$\rho_{freefilm_3} = \frac{449.2 \cdot 10^{-6}\text{kg}}{(4 \cdot 10^{-2} \cdot 5 \cdot 10^{-2} \cdot 100 \cdot 10^{-6})\,\text{m}^2} = 2246\frac{\text{kg}}{\text{m}^3}$$

The dry EP-01 coating density is given as:

$$\rho_{coating} = \frac{\rho_{freefilm_1} + \rho_{freefilm_2} + \rho_{freefilm_3}}{3} = 2272\frac{\text{kg}}{\text{m}^3}$$

B.3 Mass of water uptake versus $\sqrt{t}$

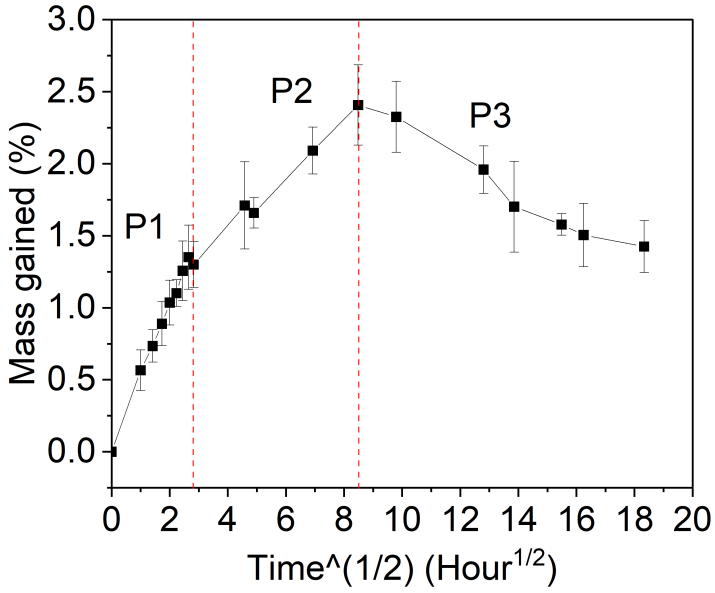

Figure B.3.1: The averaged mass percentage evolution of water uptake as a function of $\sqrt{t}$.

B.4 EIS raw data replications for coated steel sample

B.4.1 EIS raw data for epoxy coated sample S47

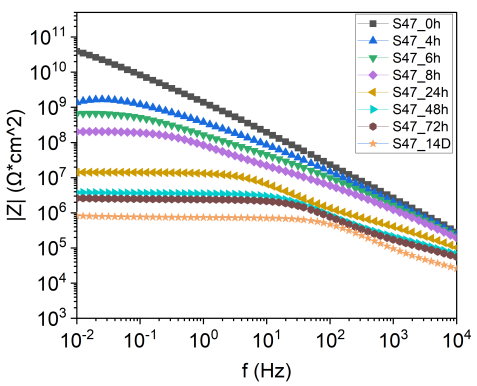

(a) Bode plot

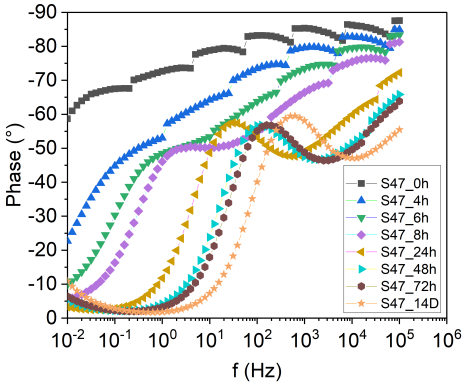

(b) Phase shift

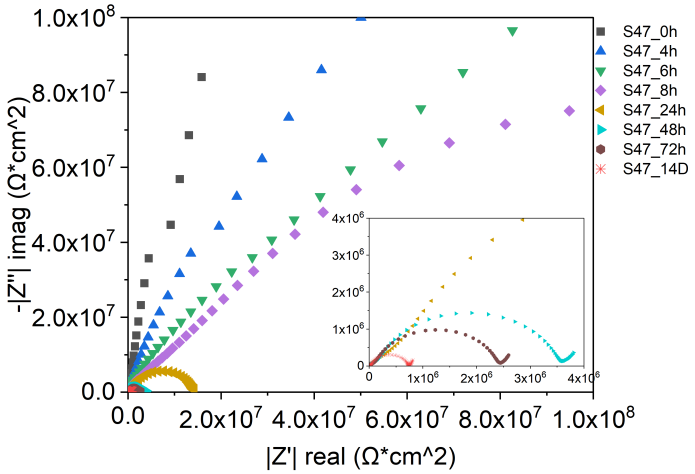

(c) Nyquist plot

Figure B.4.1: Bode plot (a), phase shift plot (b) and Nyquist plot (c) of coated steel sample S47. The discontinuities and jumps of the phase shift plot at 0 – 6 hours are caused by the wire connected to the steel sample (insufficient sample design).

B.4.2 EIS raw data for epoxy coated sample S48

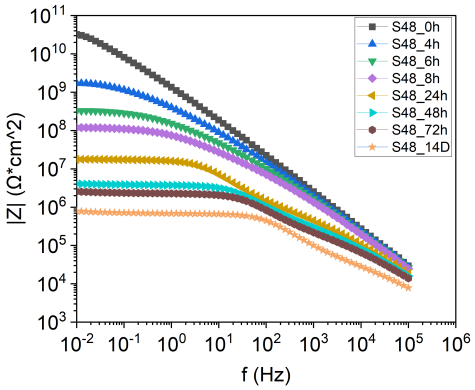

(a) Bode plot

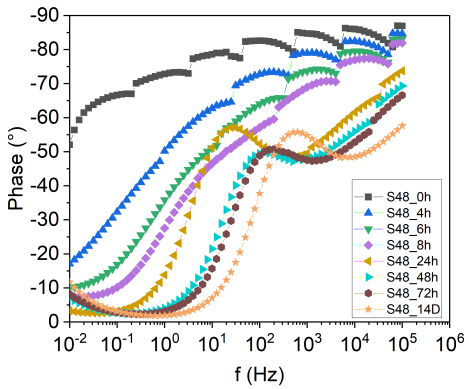

(b) Phase shift

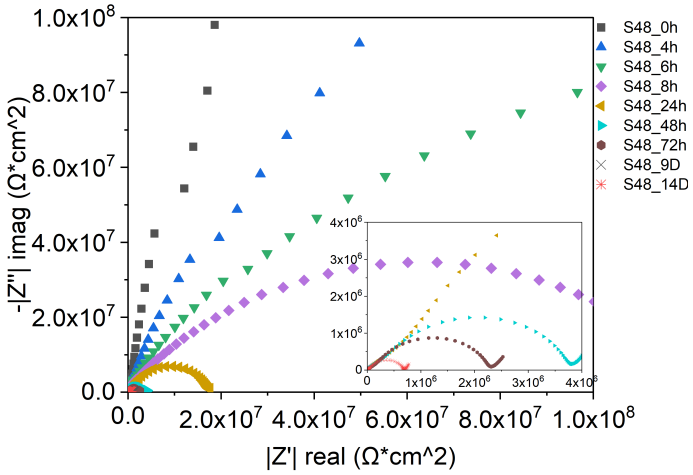

(c) Nyquist plot

Figure B.4.2: Bode plot (a), phase shift plot (b) and Nyquist plot (c) of coated steel sample S48. The discontinuities and jumps of the phase shift plot at 0 – 6 hours are caused by the wire connected to the steel sample (insufficient sample design).

B.4.3 EIS raw data for epoxy coated sample S49

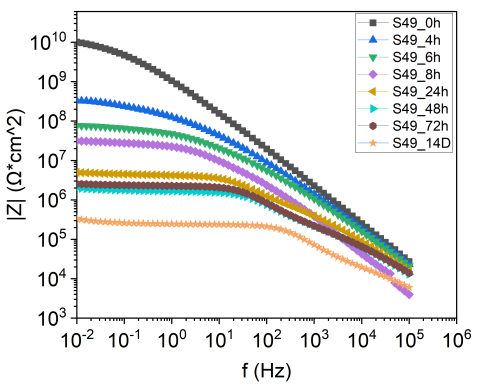

(a) Bode plot

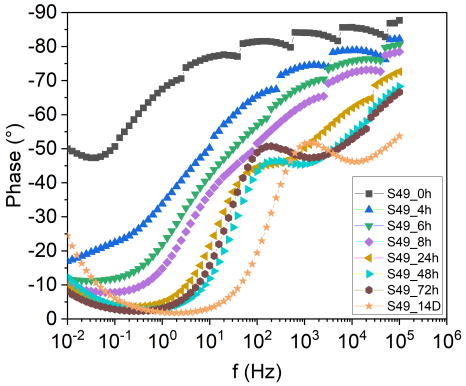

(b) Phase shift

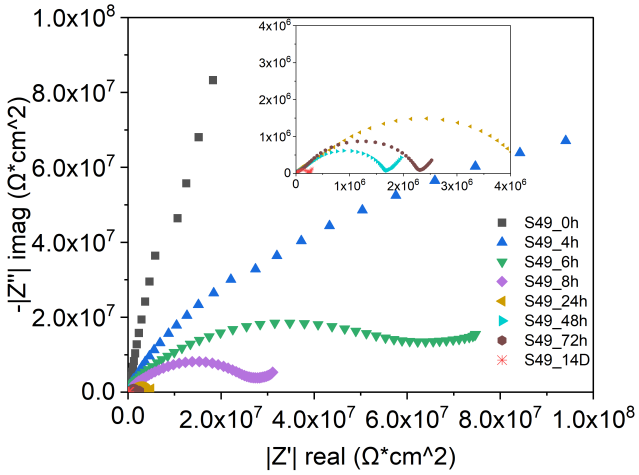

(c) Nyquist plot

Figure B.4.3: Bode plot (a), phase shift plot (b) and Nyquist plot (c) of coated steel sample S49. The discontinuities and jumps of the phase shift plot at 0 – 6 hours are caused by the wire connected to the steel sample (insufficient sample design).

B.4.4 ECM model fittings of S47

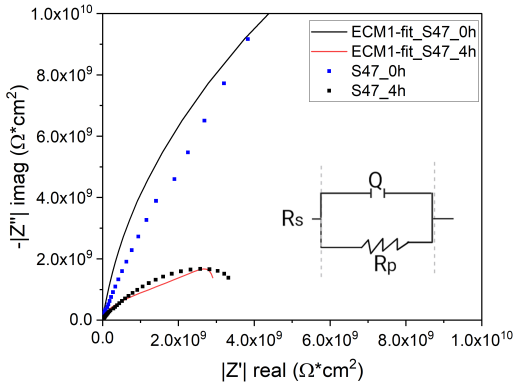

(a) ECM 1

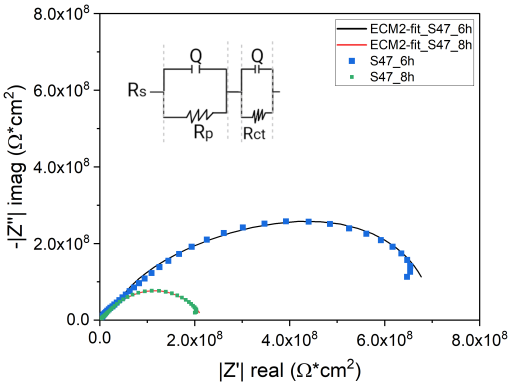

(b) ECM 2

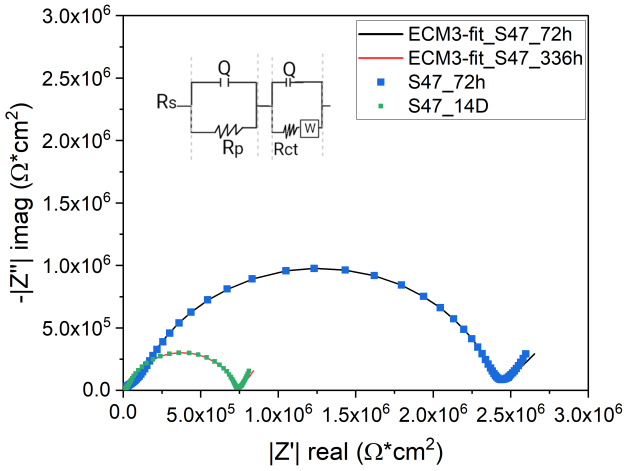

(c) ECM 3

Figure B.4.4: EEC model fittings of the measured EIS data for coated steel sample S47.

B.4.5 ECM model fitting parameters of sample S47

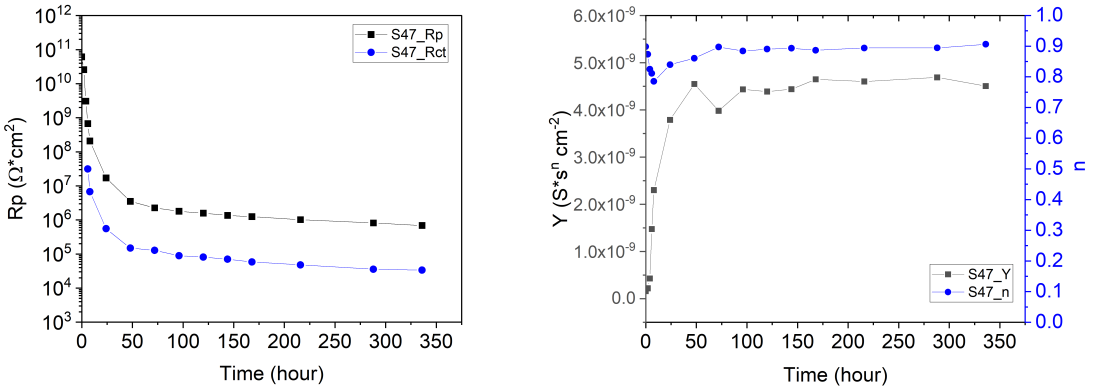

(a) ECM 1 (b) ECM 2

Figure B.4.5: Polarisation reisstance R_p and charge transfer resistance R_{ct} developments as a function of immersion time for coated steel sample S47 in (a); Constant phase element parameters Y and n evolution representing the coating capacitance behaviours (b).

B.4.6 Reproducibility of EIS data on water uptake determination

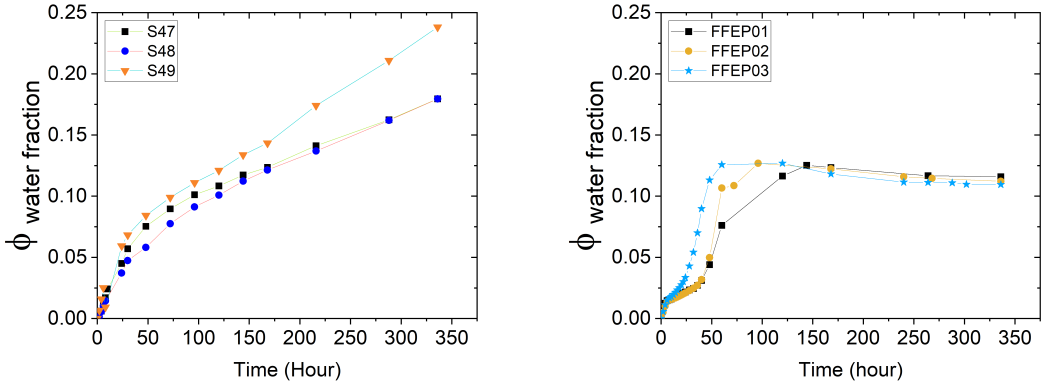

(a) Coated steel samples (b) Epoxy free films

Figure B.4.6: (a) replications of water uptake fraction determined from EIS results on coated steel samples, and (b) replications of water uptake fraction determined from EIS results on epoxy free films.

C Appendix C

C.1 Replication of rust creep propagation in EP/PUR coatings exposed to the field

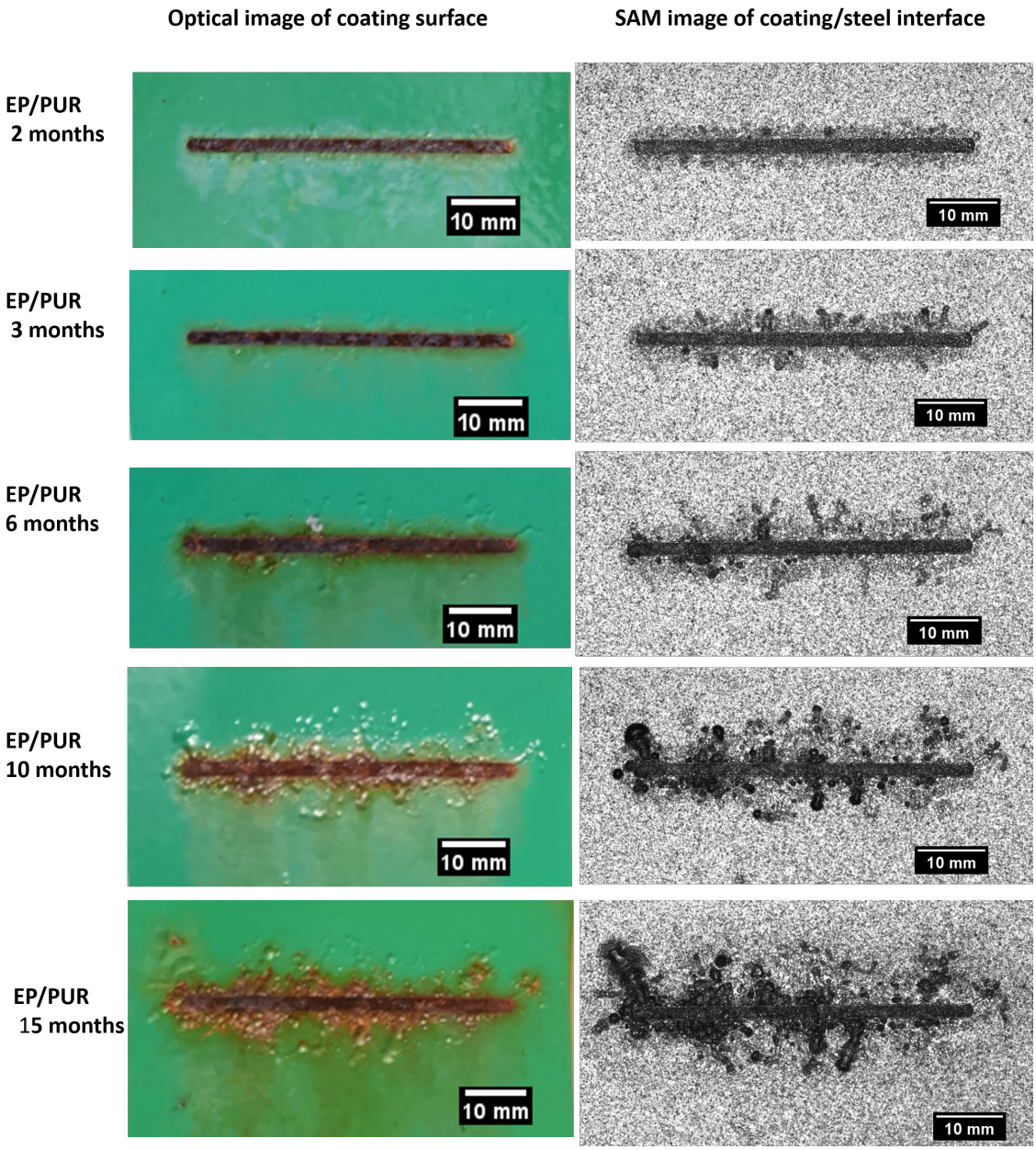

Figure C.1.1: Optical images of EP/PUR$_{R1}$ (S75) at different exposure times: 2 months, 3 months, 6 months, 10 months and 15 months and (b) SAM image of the epoxy-steel interface at the corresponding exposure time. Reproducibility check of EP/PUR coating system exposed to the field.

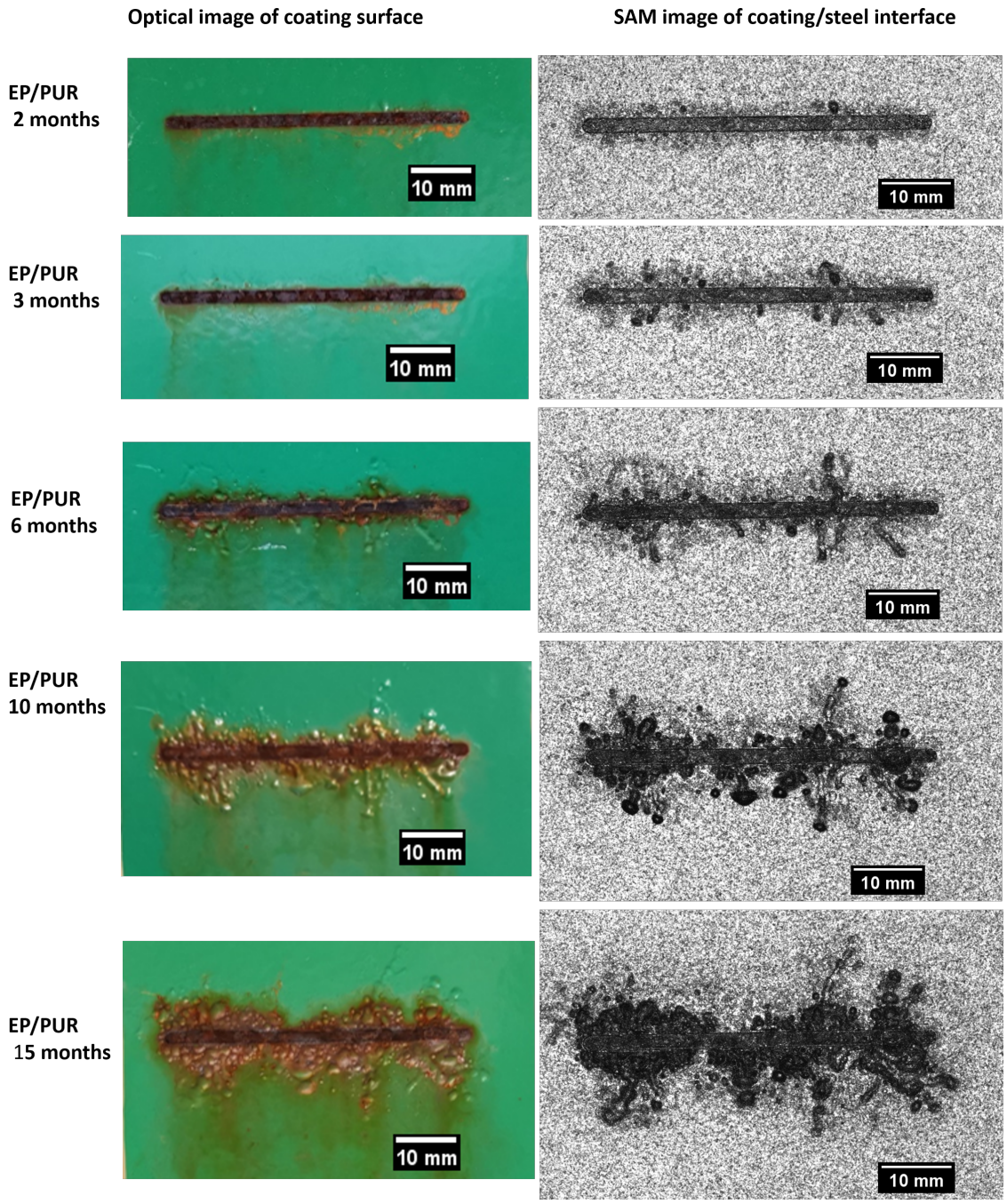

Figure C.1.2: Optical images of EP/PUR$_{R1}$ (S76) at different exposure times: 2 months, 3 months, 6 months, 10 months and 15 months and (b) SAM image of the epoxy-steel interface at the corresponding exposure time. Reproducibility check of EP/PUR coating system exposed to the field.

C.2 Replication of rust creep propagation in ZnEP/PUR coatings exposed to the field

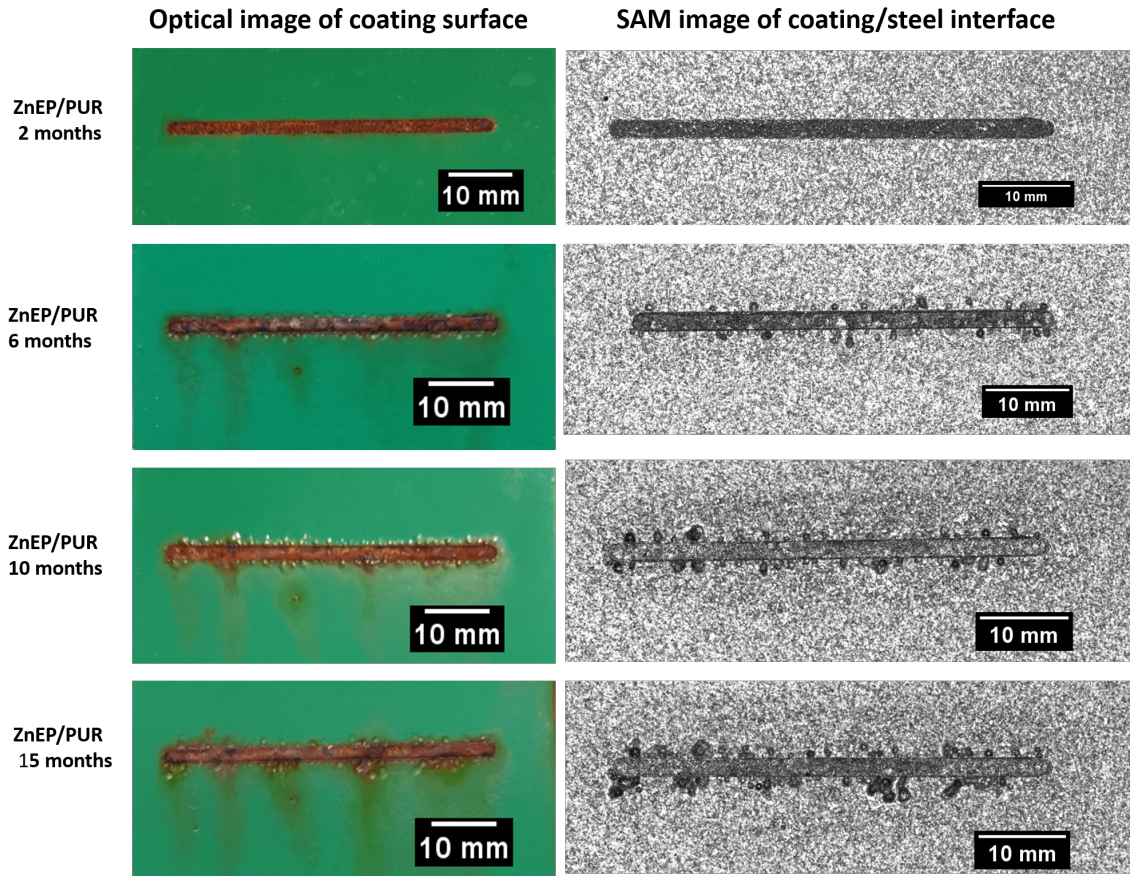

Figure C.2.1: Optical images of ZnEP/PUR$_{R1}$ system (S65) at different exposure times: 2 months, 6 months, 10 months and 15 months and (b) SAM image of the zinc rich epoxy-steel interface. Reproducibility check of ZnEP/PUR coating system exposed to the field.

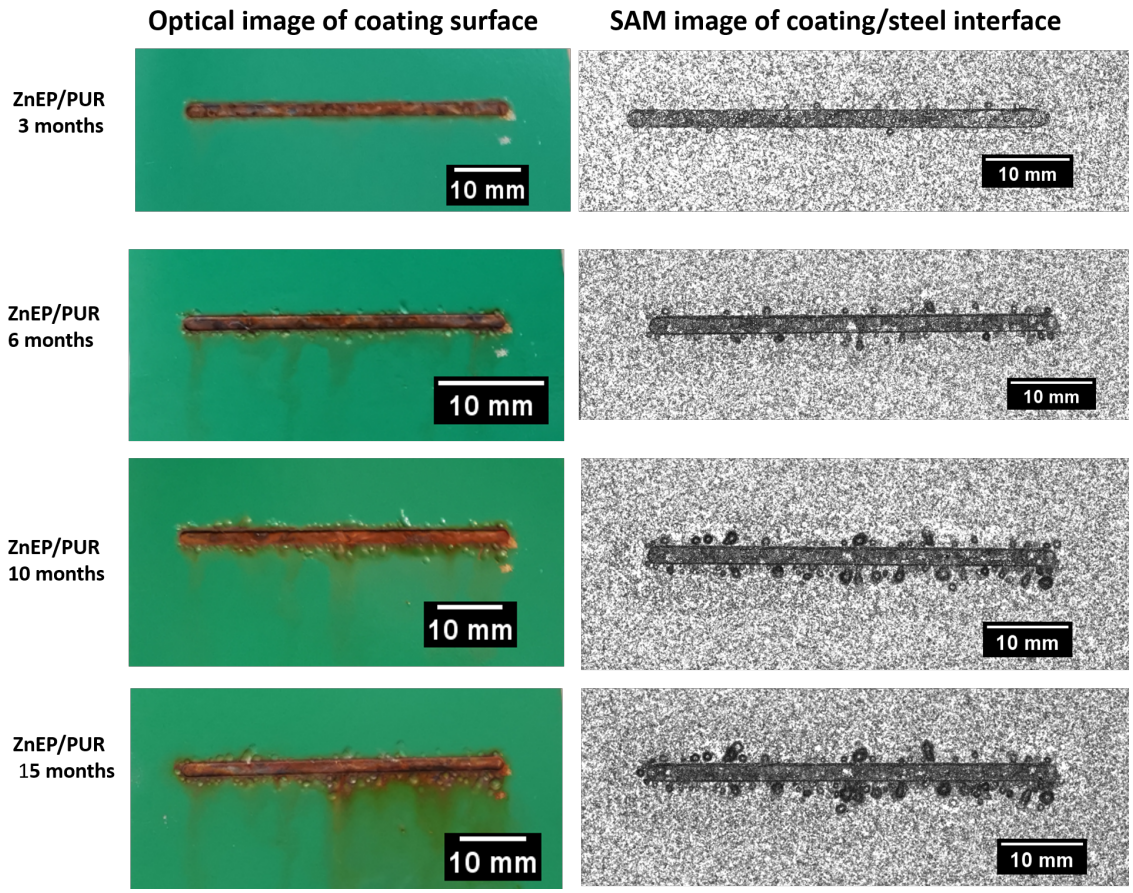

Figure C.2.2: Optical images of ZnEP/PUR$_{R2}$ system (S66) at different exposure times: 2 months, 6 months, 10 months and 15 months and (b) SAM image of the zinc rich epoxy-steel interface. Reproducibility check of ZnEP/PUR coating system exposed to the field.

C.3 Replication of rust creep propagation in EP/PUR coatings exposed to cyclic ageing test

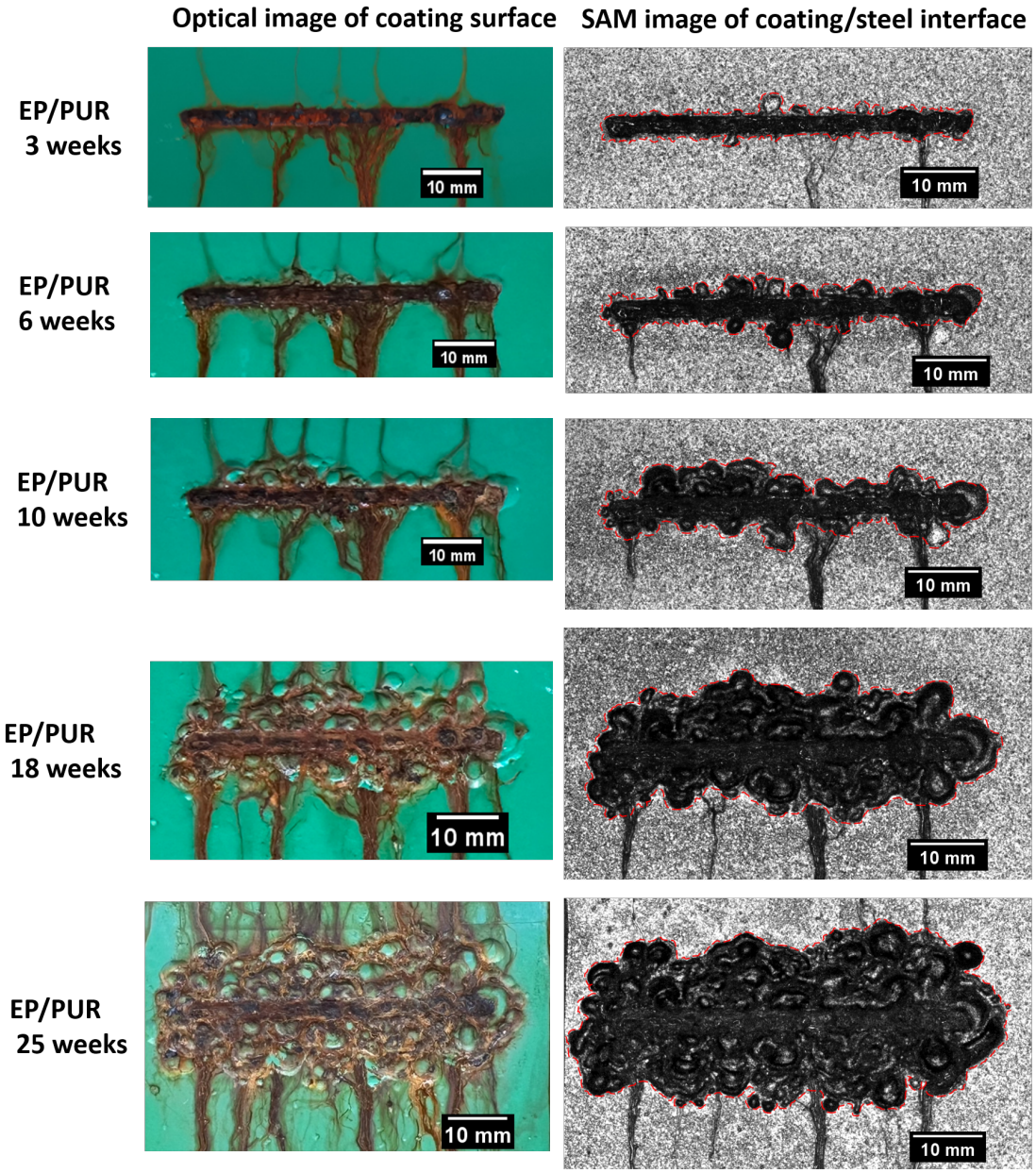

Figure C.3.1: Optical images of EP/PUR$_{R1}$ (S73) exposed to CAT test at different exposure times: 3 weeks/cycles, 6 weeks/cycles, 10 weeks/cycles, 18 weeks/cycles and 25 weeks/cycles and (b) SAM image of the zinc rich epoxy-steel interface. Reproducibility check of EP/PUR coating system exposed to CAT.

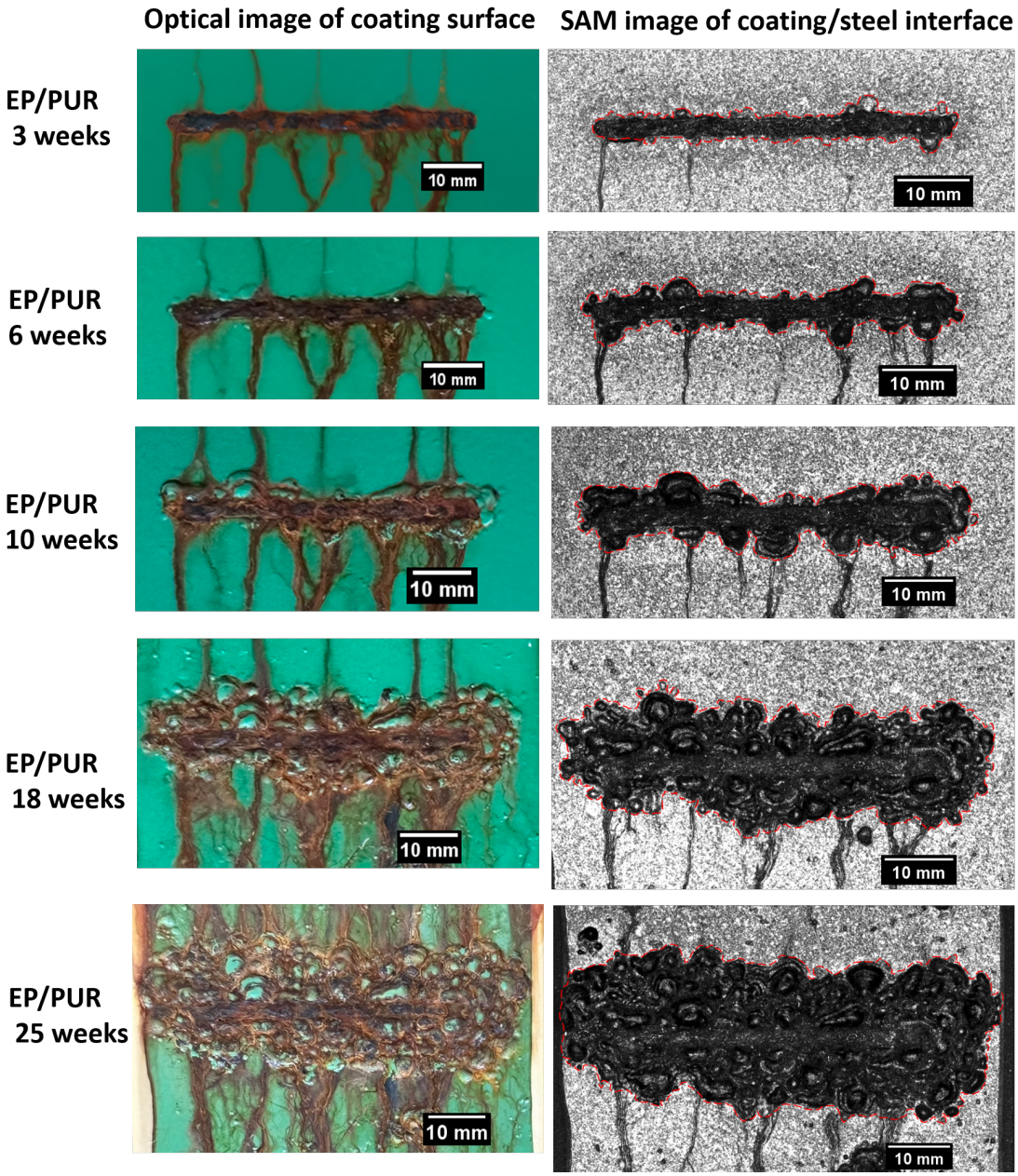

Figure C.3.2: Optical images of EP/PUR$_{R1}$ (S74) exposed to CAT test at different exposure times: 3 weeks/cycles, 6 weeks/cycles, 10 weeks/cycles, 18 weeks/cycles and 25 weeks/cycles and (b) SAM image of the zinc rich epoxy-steel interface. Reproducibility check of EP/PUR coating system exposed to CAT.

C.4 Replication of rust creep propagation in ZnEP/PUR coatings exposed to cyclic ageing test

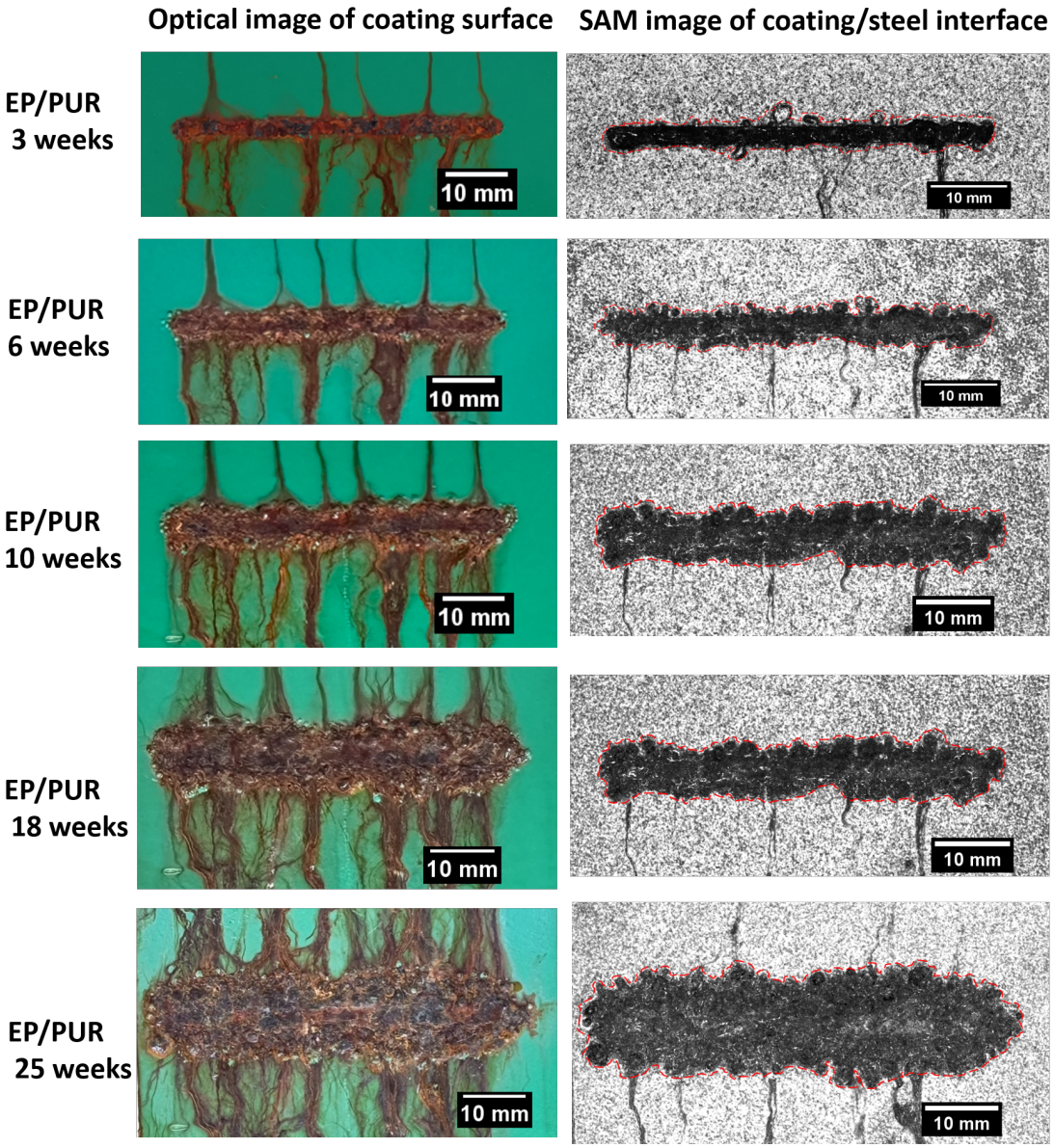

Figure C.4.1: Optical images of ZnEP/PUR$_{R1}$ (S68) exposed to CAT test at different exposure times: 3 weeks/cycles, 6 weeks/cycles, 10 weeks/cycles, 18 weeks/cycles and 25 weeks/cycles and (b) SAM image of the zinc rich epoxy-steel interface. Reproducibility check of ZnEP/PUR coating system exposed to CAT.

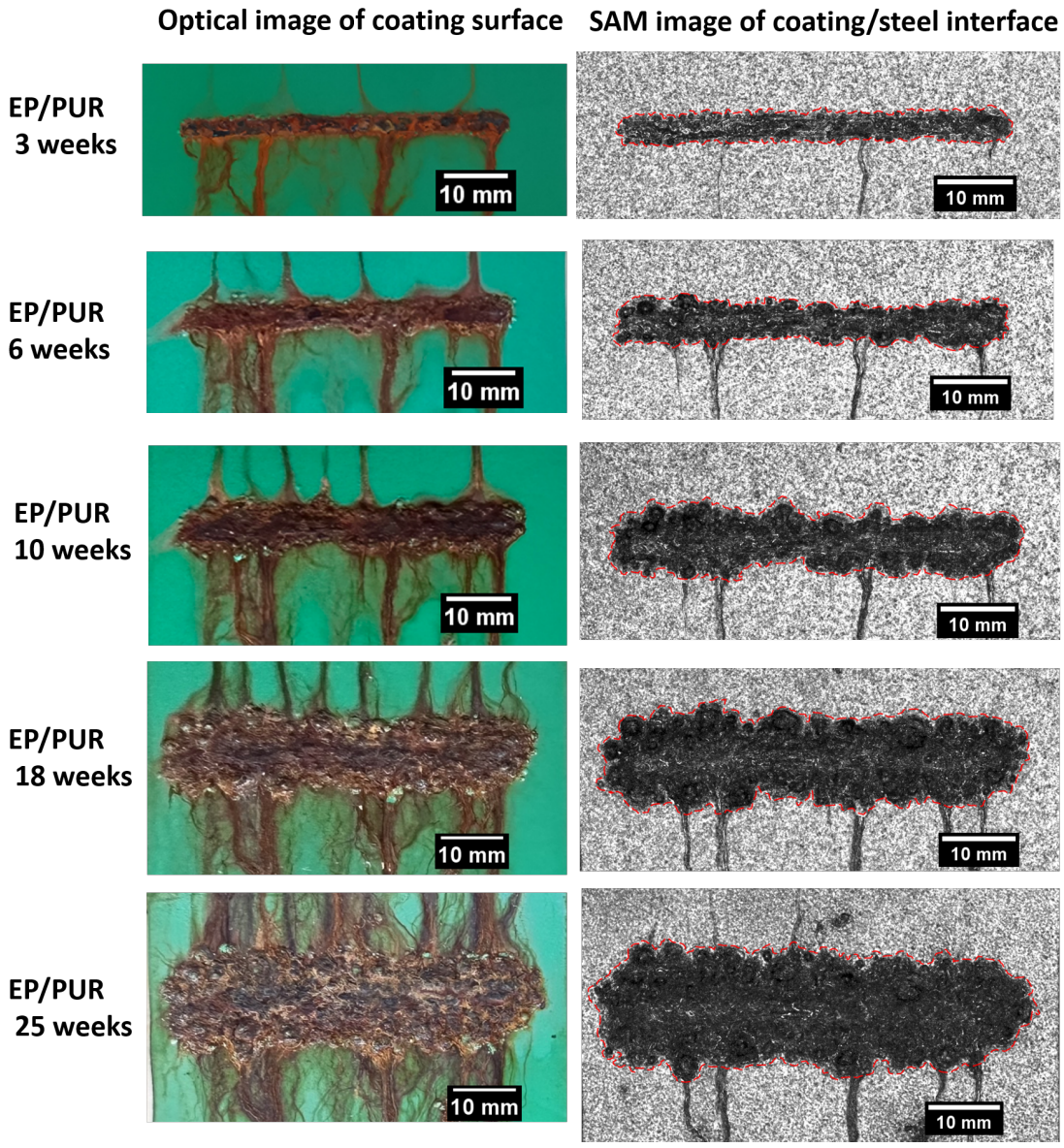

Figure C.4.2: Optical images of ZnEP/PUR$_{R2}$ system (S69) at different exposure times: 2 months, 6 months, 10 months and 15 months and (b) SAM image of the zinc rich epoxy-steel interface. Reproducibility check of ZnEP/PUR coating system exposed to CAT.

Technical
University of
Denmark

Søltofts plads, Building 229
2800 Kgs. Lyngby
Tlf. 4525 2822

www.kt.dtu.dk